Measuring stellar spin orientation by high-resolution spectroscopy

Dissertation

zur Erlangung des Doktorgrades

des Department Physik

der Universität Hamburg

vorgelegt von

Ulfert Wiesendahl

aus Hamburg

Hamburg

2010

Gutachter der Dissertation:	Prof. Dr. Günter Wiedemann Prof. Dr. Stefan Dreizler
Gutachter der Disputation:	Prof. Dr. Jürgen Schmitt Prof. Dr. Peter Hauschildt
Datum der Disputation:	13. August 2010
Vorsitzender des Prüfungsausschusses:	Dr. Robert Baade
Vorsitzender des Promotionsausschusses:	Prof. Dr. Jochen Bartels
Dekan der MIN-Fakultät:	Prof. Dr. Heinrich Graener
Departmentleiterin Physik:	Prof. Dr. Daniela Pfannkuche

Measuring stellar spin orientation by high-resolution spectroscopy

Dissertation
zur Erlangung des Doktorgrades
des Department Physik
der Universität Hamburg

im Rahmen des
Graduiertenkollegs 1351/1

vorgelegt von
Ulfert Wiesendahl
aus Hamburg

Hamburg
2010

Contents

List of Figures

List of Tables

Zusammenfassung

Die vorliegende Doktorarbeit stellt eine neue spektroskopische Methode zur Messung der Orientierung von Rotationsachsen von Sternen vor. Dabei kann nur die relative Ausrichtung am Himmel (Positionswinkel) bestimmt werden. Die Orientierung von Rotationsachsen ist wichtig zum Verständnis von Mehrfachsternsystemen und Sternen mit einer zirkumstellaren Hülle. Außerdem kann das Wissen um den Positionswinkel eines Sternes Einblicke in die Theorie der Planetenbildung ermöglichen, wo der Drehimpuls eine wichtige Rolle spielt.

Bisher war es hauptsächlich bei Transit-Planeten möglich, mit Hilfe des Rossiter-McLaughlin Effektes, die relative Ausrichtung der stellaren Rotationsachse und derjenigen des Bahndrehimpulses des Planeten zu bestimmen. Etwa 2/5 der dabei gemessenen relativen Ausrichtungen weichen signifikant davon ab, parallel zu sein, was der klassischen Theorie der Planetensystembildung einer Protoplanetaren Scheibe widerspricht. Die Kenntnis des Positionswinkels zusammen mit astrometrisch vermessenen Planetenbahnen kann die Bestimmung relativer Rotation-Planetenbahn-Ausrichtungen auch für andere Planetensysteme ermöglichen.

Die hier vorgestellte spektroskopische Methode zur Messung des Positionswinkels beruht auf dem kombinierten Linienverbreiterungseffekt der Rotation und der scheinbaren geometrischen Ausdehnung der Sternscheibe in Kombination mit einem Gitterspektrographen. Die kombinierte Verbreiterung der Linien hängt von der relativen Ausrichtung der Rotationsachse und der Dispersionsachse (bzw. des Spaltes) des Spektrographen ab. Durch Vergleich sonst identischer Messungen bei unterschiedlicher relativer Rotation-Spalt-Ausrichtung (durch 'Drehung' des Spaltes) kann der Positionswinkel des Sternes bestimmt werden.

Die Abhängigkeit der kombinierten Linienverbreiterung von der intrinsischen Voigt- und Rotationsverbreiterung sowie dem instrumentenabhängigen geometrischen Effekt und die Wellenlängenabhängigkeit wurden numerisch untersucht. Daraus wurde zur Abschätzung von Linienbreiten eine Näherungsformel entwickelt. Da die scheinbare Winkelausdehnung von nahen Sternen nur wenige Millibogensekunden und damit der geometrische Effekt wenige m/s (für 8 m Teleskope) beträgt, wurde in dieser Arbeit eine Technik zur Messung von Linienbreitenunterschieden entwickelt, die auf der bekannten Technik der Radialgeschwindigkeitsmessung mit Hilfe von hochaufgelösten Spektren und einer Gasreferenzzelle beruht, um eine vergleichbare Genauigkeit zu erreichen.

Die prinzipielle Eignung dieser Technik wurde mit Hilfe von Simulationen an künstlich verbreiterten Spektren nachgewiesen. Unter Anwendung realistischer Bedingungen durch Hinzufügung von zufällig verteiltem Rauschen zeigte die Technik allerdings eine verringerte Eignung im Vergleich zu den erreichten Genauigkeiten der Radialgeschwindigkeitsmessung.

Die Radialgeschwindigkeitsmessungen der UVES Spektren von α Tau und ϵ Indi erreichten eine Genauigkeit von ca. 6 m/s. Übereinstimmend mit den Simulationen war es mit der beschriebenen Technik nicht möglich, den Rotation-Spalt abhängigen Linienverbreiterungseffekt mit Amplituden von ca. $v_{\mathrm{geo},\alpha\mathrm{Tau}} \approx 70$ m/s und $v_{\mathrm{geo},\epsilon\mathrm{Indi}} \approx 7$ m/s zu messen. Die eingesetzte Technik benutzt diverse numerische Prozesse (Ent-/Faltungen), die wie Verbreiterungen wirken und sich anscheinend deutlich stärker negativ auf die angestrebte Verbreiterungsmessung auswirken, als auf die der Radialgeschwindigkeit.

Abstract

This thesis presents a new spectroscopic method for measuring the orientation of the rotation axis of stars. Here, only the orientation on the sky (position angle) can be measured. The knowledge of the orientation of rotation axes can help to understand multiple star systems and stars with a circumstellar envelope. Furthermore, the position angle of a star can give insights to the theory of planet building where angular momentum is important.

So far, the spin-orbit alignment, i.e., the relative orientation of the stellar rotation axis (spin) and the planetary orbit's axis, has been mostly measured by the Rossiter-McLaughlin effect for transiting planets. About 2/5 of the measured spin-orbit alignments of these planets deviate significantly from being coaligned. But coalignment is expected from the classical theory of planet building by a protoplanetary disc. The knowledge of the position angle together with astrometrical measured planetary orbits can enable the determination of the spin-orbit alignment for other planetary systems, too.

The presented spectroscopic method to measure the position angle is based on the combined line-broadening effect of stellar rotation and of the apparent geometrical extension of the stellar disc in combination with a grating spectrograph. The combined broadening of the lines depends on the relative orientation of the rotation- and dispersion axis (or the slit, respectively) of the spectrograph. The position angle can be determined by comparing identical measurements but of different spin-slit alignments (achieved by 'rotating' the slit).

The dependency of the combined line-broadening of the intrinsic Voigt- and rotation profile strength as well as of the instrumentally dependent geometrical effect and of the wavelength has been numerically studied. In that study, a line width estimation formula has been developed.

Since even nearby stars have apparent angular diameters on the order of a few milliarcseconds and, therefore, geometrical effects of a few m/s (for 8 m class telescopes), a special technique to measure line-broadening differences has been developed. To achieve a comparable accuracy, this technique is based on the known technique of measuring radial velocities with high-resolution spectra and a gas reference cell.

Simulations with artificially broadened spectra verified the principle capability of the used technique. Adding realistical random noise to the spectra, the simulations revealed a decreased ability of the technique of measuring broadening deviations compared to the achieved radial velocity accuracy.

The accuracy of the radial velocity measurements of the UVES spectra of α Tau and ϵ Indi was determined to about 6 m/s. According with the simulations, it was not possible to measure the spin-orbit dependent combined line-broadening effect with an expected amplitude of about $v_{\mathrm{geo},\alpha\mathrm{Tau}} \approx 70$ m/s and $v_{\mathrm{geo},\epsilon\mathrm{Indi}} \approx 7$ m/s. The described technique uses several numerical processes (like de-/convolutions) that act as line-broadening effects. They seem to have a much stronger negative impact on the line-broadening measurement than on that of the radial velocity.

Chapter 1

Introduction

The Research Training Group / Graduiertenkolleg GRK 1351/1 "Extrasolar Planets and Their Host Stars" funded by the Deutsche Forschungsgemeinschaft (DFG), in which context this work is placed, is a joint GRK between the Hamburger Sternwarte of the University of Hamburg, the Institut für Astrophysik of the University of Göttingen and the Max-Planck-Institut für Sonnensystemforschung. It is dedicated to the common exploration of extrasolar planets and their parent stars. The interplay of the two in formation, evolution and characteristics is the main focus of the GRK.

The exploration of extrasolar planets (or exoplanets) is a relatively new topic in astrophysics. Regarding the rich planetary environment of our solar system, astronomers have been looking for planets around other stars (i.e., extrasolar planets) a long time. But it took until 1995 before the first extrasolar planet *51 Peg b* around a normal star has been found (Mayor & Queloz (1995)). Before that, only some planets around pulsars could be detected. Since then, over 400 extrasolar planets have been found. A list of the number of planets sorted by their detection method can be found in table 1.1, for more information see *The Extrasolar Planets Encyclopedia* at http://www.exoplanet.eu.

Detection method	Planetary systems	Total number of planets
Radial velocity or astrometry	361	422
Transit photometry	79	79
Microlensing	9	10
Direct imaging	10	12
Timing	6	9

Table 1.1: Table on the number of extrasolar planets sorted by their detection method for a total of 453 candidates (data from www.exoplanet.eu (as of May 4th, 2010)).

Because the central star is much brighter than the orbiting planet, most planets have been detected with indirect measurements. The majority of planets have been found using the radial velocity (RV) method, which measures the periodic wavelength shift oscillation of the Doppler effect caused by the star's movement with a planet around the center of mass of the system.

The periodic radial velocity shift can be measured at high accuracy with a combination

of a spectrograph and a reference gas cell in front of it with the light of the star passing through it. The gas cell method (or equivalent methods like a stable spectrograph with synchronised ThAr, e.g. HARPS) delivers a reference wavelength scale and the possibility to determine the instrumental profile (or line-spread function, the spectral equivalent to the point-spread-function).

Besides, over 70 planets have been found with the transit light curve measurement. A transit occurs when the orbital axis of a planet is almost perpendicular to the line-of-sight of the observer ('edge-on'). During the so-called primary transit the planet crosses in front of the star (from an observer's point of view)and obscures a tiny amount of the stellar disc resulting in a slightly lower brightness of the star. This brightness decrease can be measured. Space based missions like the CoRoT or the Kepler satellite achieve a much higher magnitude accuracy as ground based telescopes. A general overview of the transit geometry can be found in figure 1.1.

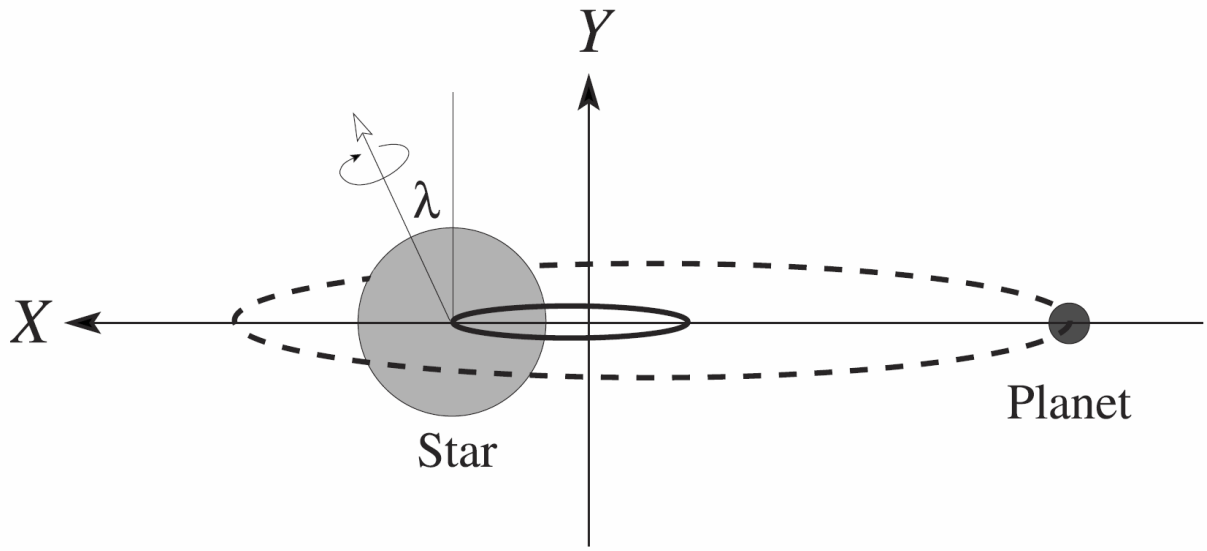

Figure 1.1: Geometrical configuration of a transiting planet as projected on the sky (X-Y-plane; line-of-sight = Z direction) with λ being the spin-orbit alignment angle (taken from Winn et al. 2005).

Further methods to detect planets are looking for microlensing events or direct imaging. Microlensing is an effect of the General Theory of Relativity. Here, the mass of an accidently passing foreground star (or planetary system) can act as a gravitational lens. The lensing system amplifies the light of a background star resulting in a characteristic one-time event brightness enhancement. A planet in a lensing system causes a smaller second peak.

Direct imaging of extrasolar planets is challenging since the central star is much brighter than the orbiting planet. Therefore, planets on a wide orbit are easier to detect. That also means a long period, which translates into observations passing years to discover the movement of the planet.

Planets can also be detected with various timing method, which has been succesfully applied first to pulsars. In the latter case, the variation of the characteristic pulsar frequency

due to planets is measured. Planets around pulsars have been found even earlier than *51 Peg b*.

1.1 Spin-orbit alignment

Apart from light curve photometry, for transits, further information can be gained with spectroscopy. During a transit the planet obscures parts of the rotating stellar disc with different projected rotation velocity $v_{\mathrm{rot}} \cdot \sin i$ (with i being the inclination angle between the rotation axis and the line-of-sight) according to the distance to the rotation axis. The shifted radial velocity distribution is illustrated in figure 2.2 of section 2.1.

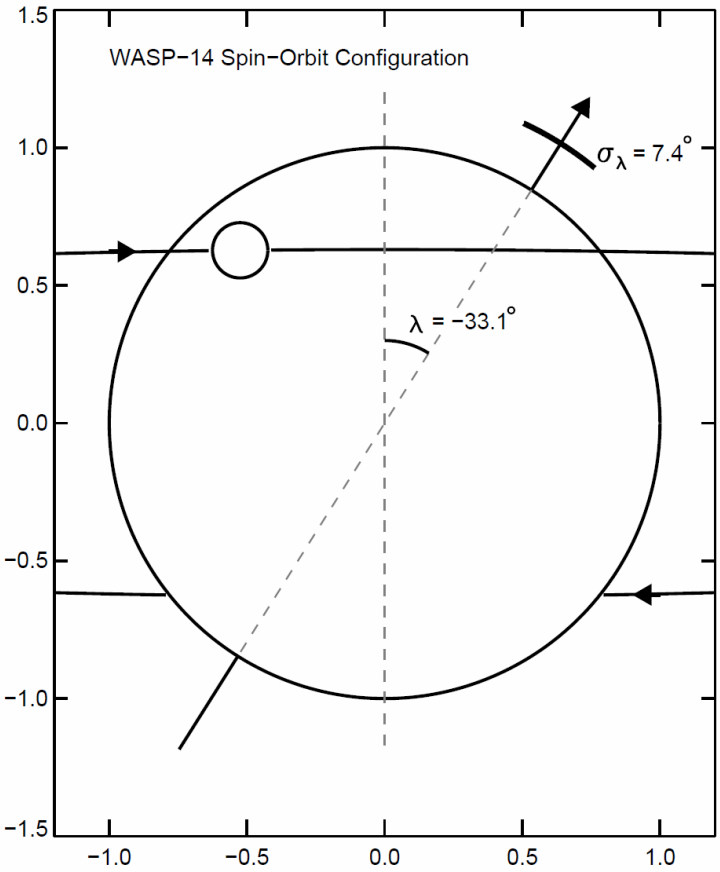

Figure 1.2: Scheme of the transiting planet WASP-14 in front of the stellar disc with a spin(arrow)-orbit misalignment of $\lambda = -33.1 \pm 7.4$ degree (taken from Johnson et al. 2009).

Depending on the traveling direction the planet first blocks the more blue shifted parts, passes the unshifted rotation axis and finally blocks the more red shifted parts of the stellar disc (or vice-versa), which causes a distortion to the stellar spectral line profile. This effect is called the Rossiter-McLaughlin effect.

Planet	Spin-orbit alignment (projected, degree)	reference
CoRoT-2b	7.2 ± 4.5	Bouchy et al. (2008); Fabrycky & Winn (2009)
Formalhaut b*	1 ± 3.3	Le Bouquin et al. (2009)
Hat-P-1b	3.7 ± 2.1	Johnson et al. (2008)
Hat-P-2b	1.2 ± 13.4	Winn et al. (2007)
	$0.2^{+12.2}_{-12.5}$	Loeillet et al. (2008)
Hat-P-13b	-0.9 ± 8.5	Winn et al. (2010)
HD149026b	-12 ± 15	Wolf et al. (2007)
HD17156b	10 ± 5.1	Narita et al. (2009*a*)
HD189733b	-1.4 ± 1.1	Winn et al. (2006)
HD209458b	-4.4 ± 1.4	Winn et al. (2005)
SuperWASP-3b	15^{+10}_{-9}	Simpson et al. (2010); Tripathi et al. (2010)
	$3.3^{+2.5}_{-4.4}$	
SuperWASP-4b	-4^{+43}_{-34}	Triaud et al. (2010)
SuperWASP-5b	$-12.4^{+11.9}_{-8.2}$	Triaud et al. (2010)
SuperWASP-6b	11^{+14}_{-18}	Gillon et al. (2009)
SuperWASP-18b	$-5^{+3.1}_{-2.8}$	Triaud et al. (2010)
TrES-2	-9 ± 12	Winn et al. (2008)
TrES-4	-6.3 ± 4.7	Narita et al. (2010)
CoRoT-1b	77 ± 11	Pont et al. (2009*a*)
CoRot-3b	$37.6^{+10}_{-22.3}$	Triaud et al. (2009)
Hat-P-7b	182.5 ± 9.4	Winn et al. (2009*b*)
	$-132.6^{+10.5}_{-13.6}$	Narita et al. (2009*b*)
HD80606b	≈ 50	Gillon (2009); Pont et al. (2009*b*), Winn et al. (2009*a*)
Kepler-8b	-26.9 ± 4.6	Jenkins et al. (2010)
SuperWASP-2b	153^{+11}_{-15}	Triaud et al. (2010)
SuperWASP-14b	-33.1 ± 7.4	Johnson et al. (2009)
SuperWASP-15b	$139.6^{+5.2}_{-4.3}$	Triaud et al. (2010)
SuperWASP-17b	≈ -150	Anderson et al. (2009)
TrES-1	30 ± 21	Narita et al. (2007)
XO-3b	-37.3 ± 3.7	Winn et al. (2009*c*)

Table 1.2: Table of measured spin-orbit alignments of extrasolar planets with the Rossiter-McLaughlin effect (as of March 2010). Those planets with a significant spin-orbit misalignment ($>\pi/8 = 22.5°$) are separated in the lower part. *The position angle of the star Fomalhaut was measured to be $65 \pm 3°$, while the disk angle was with $156 \pm 0.3°$ observed to be almost perpendicular. So far, no planet of this system shows transits.

The Rossiter-McLaughlin effect depends on the spin-orbit alignment, that is the angle between the orbital axis of the planet and the rotation axis (spin) of the star projected on the sky. Only the relative angle can be measured, the full spatial orientation of the rotation axis or of the orbital axis, respectively, is not accessible with that technique. A scheme of the spin-orbit geometry can be seen on figure 1.2 exemplified by the WASP-14

exoplanet or more generally in figure 1.1.

A detailed description of the Rossiter-McLaughlin effect and a recent summary of the measurements can be found in Fabrycky & Winn (2009). So far, more than two dozen transiting planets' spin-orbit alignment has been measured by the Rossiter-McLaughlin effect.

For most of these planets the spin-orbit alignment is compliant or close to the coalignment state. This is also true for our solar system, in which the ecliptical plane deviates only $\approx 7°$ from being coaligned with the Sun's equator (the other solar planets' planes are even closer to coalignment). But there is also a considerable number of misalignments. An overview of the measured spin-orbit alignments can be found in table 1.2.

Of the planets with measured Rossiter-McLaughlin spin-orbit alignments eleven show a spin-orbit misalignment, the planetary orbit deviates significantly ($>\pi/8 = 22.5°$) from being coaligned with the stellar rotation. Four of them, *HAT-P7b*, *SuperWASP-2b*, *SuperWASP-15b* and *SuperWASP-17b* even have retrograde orbits. All known extrasolar planets with a significant spin-orbit misalignment are listed in the lower part of table 1.2.

For Formalhaut it was possible to determine the position angle to $PA_{\text{Formalhaut}} = 65 \pm 3°$ by precise spectro-astrometric measurements using near-IR long baseline interferometry (Le Bouquin et al. 2009). The position angle of the disc in that planetary system was determined to be $PA_{\text{disc}} = 156 \pm 0.3°$. So the disc is almost perfectly perpendicular to the star's rotation axis.

There has also been one successful approach to measure the position angle of Aldebaran (or α *Tau*) with a differential Speckle interferometry experimental device (Lagarde et al. 1995). The technique is based on the deviations of the Speckle patterns in various spectroscopic channels. They found a position angle (starting from the N-S direction) of $PA = 110 \pm 5\,°$ for Aldebaran, which is one of the apparently larger stars on the sky with about 20 mas in diameter.

The knowledge of the spin-orbit alignment of planetary systems can give insights to the theory of planet formation. Small angles between the planet and its star indicate a classical building scenario from a protoplanetary disc forming all members of the planetary system.

Small inclinations within a multi-planet system (like our solar system) are evidence for a formation scenario of a contracting protostellar cloud forming into a protoplanetary disc while conserving angular momentum. Further theories regarding planet migration or a non axial-symmetrical collapse of the initial molecular cloud can be tested with the actual measured spin-orbit alignment. The observed misalignment can also indicate an early external third body close encounter scenario.

1.2 Motivation

In the preceding paragraph the ability to measure the relative spin-orbit alignment with the Rossiter-McLaughlin effect has been introduced. No information on the absolute orientation of the spin or the orbit can be derived from it. Also, the Rossiter McLaughlin effect is directly connected to transits, which are rare compared to the number of observable stars. So far, there has not yet been any other successful method to measure the spin-orbit

alignment except for resolved interferometric techniques. Therefore, it is important to find alternative methods. This work introduces a spectroscopic method to measure the position angle of a star on the sky.

The position angle of a star is the angle between the projected rotation axis of a star and the north-south reference direction of the celestial coordinate system. The method is based on two effects, the stellar rotation and the extension of the elongated stellar disc. Only the orientation projected on the sky can be measured, the inclination would be needed to constrain the full spatial orientation.

The rotation of stars causes a Doppler wavelength shift of the light coming from different points of the stellar disc depending on the distance from the rotation axis (see also figure 2.2 of section 2.1). Integrated over the whole disc, this leads to stellar line broadening with a well known characteristic circular broadening profile.

The extension of the stellar disc itself has a geometrical effect. Light coming from different points of the disc has a slightly different incident angle on the grating. The angular deviation depending on the projected distance on the dispersion axis of the spectrograph causes a geometrical wavelength shift as illustrated in figure 2.3 of section 2.2.

Taking both rotational Doppler shift and geometrical wavelength shift into account, a summed wavelength shift for each point of the stellar disc results. Integrated over the disc, this leads to a combined line broadening. The summed wavelength shift depends on the alignment of the projected rotation axis of the star and the orientation of the dispersion axis of the spectrograph.

To measure the position angle of a star, the combined wavelength shift as mentioned above will be used. The stellar line broadening caused by the rotation and geometrical effect leads to tilted stellar lines on the 2D spectrographic image of a star. Using the extracted 1D spectrum, this leads to line broadening.

The main idea is to measure the stellar line broadening of the same star with different spin-slit alignments (the slit is perpendicular to the dispersion axis). Since the broadening depends on the spin-slit alignment, the orientation of the spin axis of the star can be derived by measuring the spin-slit dependend line broadening of such observations and the known orientation of the slit (ergo dispersion axis).

The combined broadening is maximal (minimal) for the dispersion axis being perpendicular (or flipped by 180°) with the rotation axis of the star. Then, the rotationally blue-shifted hemisphere is also geometrically blue shifted (red shifted) along the dispersion axis of the spectrograph, which is illustrated in figure 1.3. For a full coverage of spin-slit alignments (that can be achieved by using different derotator position angles) a 360° periodic progression of the measured spectral line broadening with the derotator position angle is expected. The progression has its maximum at the spin axis being parallel to the slit (perpendicular to the dispersion axis) and its minimum for an antiparallel alignment.

The angular diameter of (even nearby) stars are very small (in the order of milliarcseconds), so the small differential broadening effect between spectra of different spin-slit alignment must be measured with high accuracy (better than some tens of m/s). For radial velocities (RV) such an accuracy can be achieved using a radial velocity analysis program with observations based on using a gas cell (or other reference systems) for wavelength reference and an accurate determination of the instrumental profile. Such radial velocity analyses

have been successfully used for finding the radial velocity oscillations of a star caused by a planet (e.g., Marcy et al. 1997; Butler et al. 1997).

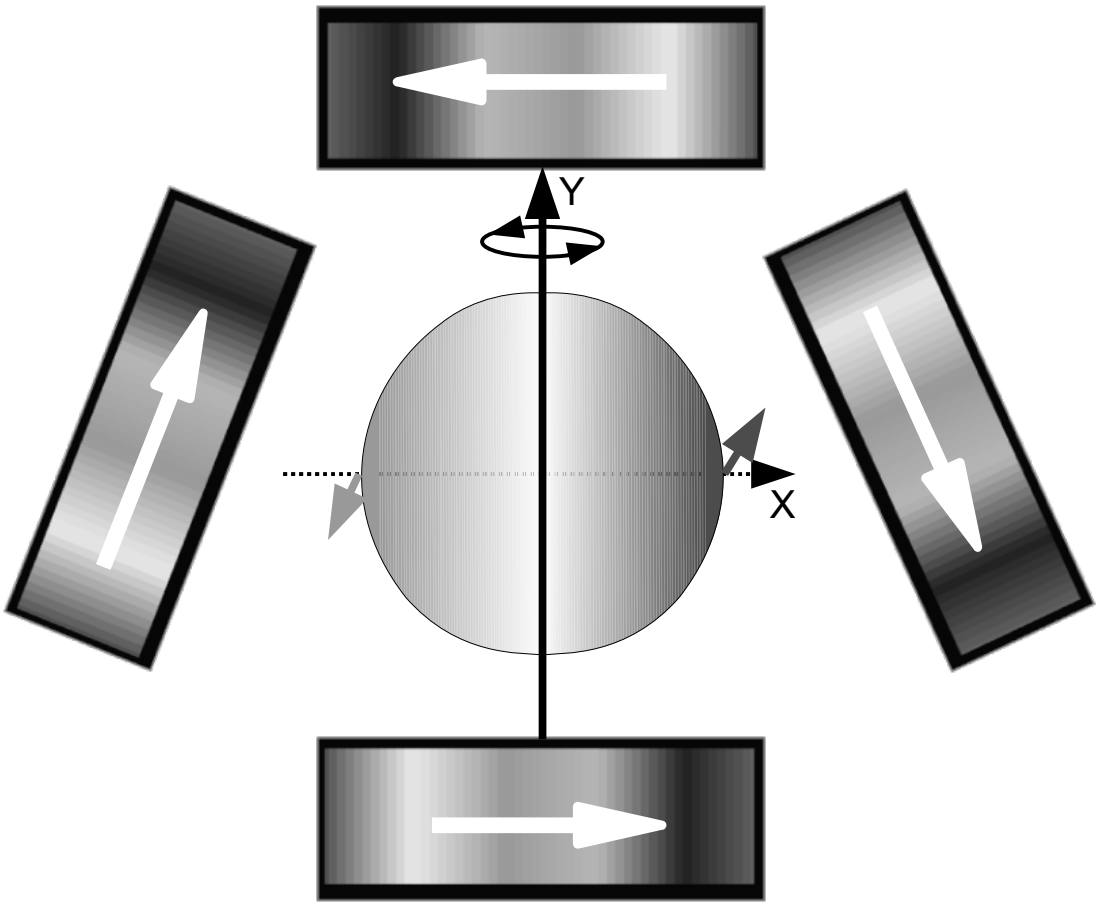

Figure 1.3: Scheme of the stellar disc's rotational Doppler shift distribution (see color gradient and velocity arrows) probed by different spin-slit alignments. The rainbow bars and the white arrows indicate the dispersion axis (being perpendicular to the slit). The maximal (minimal) combined broadening effect is achieved with the bottom (top) spin-slit alignment with (anti-) corresponding wavelength shifts.

For a stellar line profile, the radial velocity shift is measured with the central position of a stellar line and the width of that line corresponds to a two point position measurement (for example one at half height at each side of the line for the full width at half maximum). For an analytical line profile, it can be derived that the line width (here the equivalent to the line broadening) can be measured with a comparable accuracy as the line position. Therefore, the RV method has been expanded to also measure differential line broadening.

For measuring a star's spin orientation, identical spectrographic observations but of different position angle have been performed within a small time frame using an iodine cell. Such spectra for three nearby stars have been analyzed in this work to measure the stellar line broadening deviations of different position angles in order to determine their spin orientation.

1.3 Chapter overview

This work is divided into eight chapters starting with the introduction in chapter one. In chapter two, the theoretical background of line broadening effects used in this work is presented, that is mainly the stellar rotation, the geometrical effect of the elongated stellar disc and the spin-slit alignment dependent combined effect.

Chapter three follows with numerical estimations of the combined line broadening effect using intrinsic Voigt profiles and a spherical rotation profile including limb darkening. The influence of the intrinsic and rotational profile widths on the combined effect is examined there. Furthermore, a line width estimation formula is given and the influence of the wavelength dependence (through the limb darkening) is evaluated.

Chapter four deals with the observed target stars. Basic stellar parameters are given as well as information on the used spectrograph and observational setup. Information on the used data reduction are also to be found there.

Chapter five is about the modeling method and its implementation. Every important processing step of the spectral modeling like the stellar template creation and the instrumental profile modeling is explained. Finally, the extension of the RV method with a differential broadening measurement is presented.

Chapter six continues with simulations of the used analysis method with test spectra that have been constructed from artificially broadened template spectra and then used as target spectra. Ideal as well as more realistic noisy conditions have been applied there.

Chapter seven then presents the results of the method applied to real data from two stars, $\alpha\,Tau$ and $\epsilon\,Indi$ observed with the VLT/UVES spectrograph.

Chapter eight finally summarizes the results of this work. The advantages and disadvantages of the used method are discussed and an outlook on alternative methods and ongoing work is given.

Chapter 2

Theoretical background

Apart from intrinsic stellar line broadening there are two main effects leading to line broadening that are relevant for the method introduced by this work. Since all stars are rotating, the rotational Doppler shift is important. The second effect that contributes to the stellar line broadening is a geometric effect due to the extended stellar disc.

The idea for the spectroscopic method presented here to derive the absolute position angle of stars with the spin-slit alignment dependent line broadening was devised by G. Wiedemann of Hamburger Sternwarte.

2.1 Rotational Doppler effect

As already mentioned before, angular momentum is a conserved quantity in physics. It is believed that stars form from collapsing molecular clouds of a certain angular momentum. Because stars are much more contracted than the initial cloud, large stellar rotation rates are expected from the pure conservation of angular momentum. Due to losses of angular momentum in the star formation process, measured rotation rates have far below values than as expected from the pure conservation of angular momentum. For example, cooler stars like our sun have equatorial rotation velocities of a few kilometers per second.

Spectral lines are massively affected by the relative Doppler shift of the light coming from different parts of the stellar disc. The Doppler line broadening depends on the alignment of the stellar rotation axis $\vec{\Omega}$ and the observer's line of sight. The angle between the orientation of the rotation axis and the line of sight of the observer is named the inclination i, see figure 2.1 for a coordinate scheme. Without expecting a general preferential orientation of stellar axes this inclination angle should be randomly distributed.

In general, the inclination is unknown. There are only a few cases where the inclination can be measured with resolved stellar discs looking for moving star spots or using asteroseismology (Gizon & Solanki 2003). Apart from that, the expected real rotation velocity can be predicted in principle from stellar modeling and the knowledge of the exact stellar type and age, which is hard to determine. But the deceleration of the rotation velocity is not acessible for modeling.

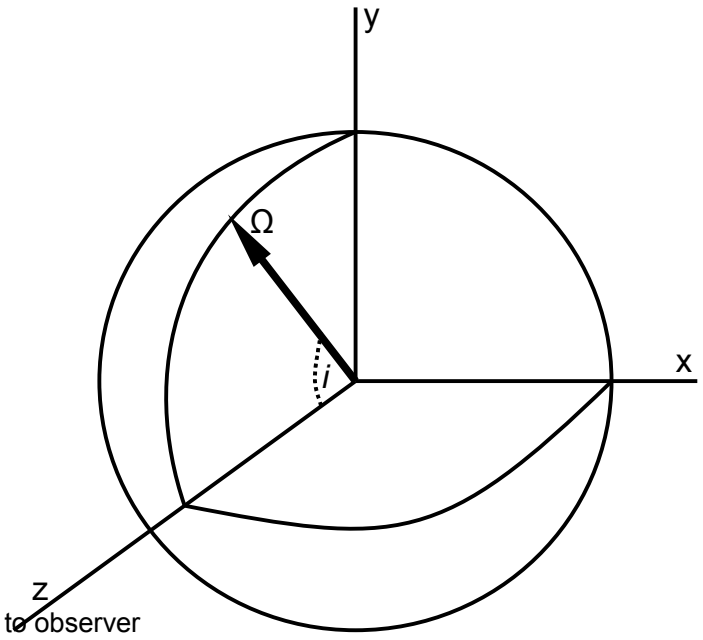

Figure 2.1: This figure illustrates the coordinate system for a rotating star with a rotation axis Ω. The x and y axis represent the plane of the sky being perpendicular to the z axis pointing towards the observer. For simplicity, the rotation axis is set to lie in the yz plane. The velocity for any point on the surface due to rotation is given by $\vec{v} = \vec{\Omega} \times \vec{R}$ with $\vec{R}$ being the stellar radius to the point. The component towards the observer (z) is given by the Doppler shift. The inclination i is the angle between the rotation axis and the z axis.

The calculation of the rotational wavelength shift due to the Doppler shift for a rotating star is shown now. The calculations of the rotation profile performed here are following Gray (1976). We assume a circular star that is handled as a rotating rigid body. The coordinate system is chosen according to figure 2.1. The xy plane is perpendicular to the observer's line of sight along the z axis. The rotation axis lies in the yz plane with the inclination angle i between the line of sight (z axis) and itself. The angular velocity of the star is given by Ω. The radius vector $\vec{R}$ points to any point on the stellar surface.

With this configuration the linear velocity of a single point anywhere on the stellar surface is given by

$$\vec{v} = \vec{\Omega} \times \vec{R}$$

with $\times$ meaning the vector product.

Only the z component (i.e., that component along the observer's line of sight) goes into the Doppler effect

$$v_{\mathrm{z}} = x\Omega \sin i$$

Switching to the wavelength regime this transfers to

$$\Delta\lambda = \frac{v_{\mathrm{z}}}{c}\lambda = \left(\frac{\lambda\Omega \sin i}{c}\right) x$$

This equation reveals that all points on the surface that have the same x coordinate undergo the same wavelength shift regardless of the y component. This is illustrated in figure 2.2 with the stellar disc divided into color gradient coded strips parallel to the x axis. These strips indicate areas of the same wavelength shift. The strips that are most distant to the y axis have the strongest effect (shown by the darkest color) while the inner strips near the projected rotation axis (i.e., y axis) show a weaker effect. Light coming from points on the projected rotation axis is not shifted. In figure 2.2 this behavior is coded by the color gradient on each half of the stellar disc.

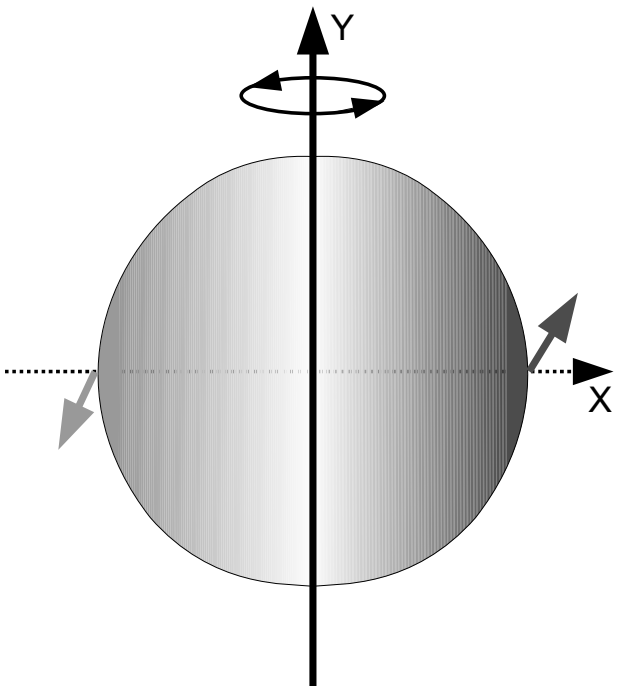

Figure 2.2: Illustration of the rotational Doppler wavelength shift $\Delta\lambda = \lambda\Omega \sin i \; x/c$ distribution being only dependent on the distance x from the projected rotation axis (y axis). One half of the stellar disc is moving towards the observer resulting in a blue shifted half (left side) while the other one moves away from the observer resulting in a red shifted half (right side), which is represented by the color gradient.

The resulting Doppler wavelength shift is maximal at the most distance to the projected rotation axis, that is at the limb where the distance equals the stellar radius $x = R$. With that, the maximal rotational Doppler wavelength shift is

$$\Delta\lambda_{\max} = \left(\frac{\lambda\Omega \sin i}{c}\right) R$$

With $v_{\rm rot} = \Omega R$ at the equator (limb) this finally leads to

$$\Delta\lambda_{\max} = \frac{\lambda}{c} v_{\rm rot} \sin i$$

Now with a formula for the wavelength shift for each point on the stellar disc, the rotational broadening profile results from integrating over the stellar disc. The rotational broadening

profile is a circular function of the maximal wavelength shift and therefore of the projected rotation velocity at the equator. The integration itself is postponed to section 2.3.1 since the geometrical effect described in the next section has to be included as well.

2.2 Geometrical effect

The geometrical effect is based on the extended stellar disc. This is usually neglected since most stars are far away from the observer and the stellar discs (with typical diameters in the order of milliarcsenconds) can usually not be resolved with current 10m class optical telescopes (except for interferometry in some cases). Furthermore, there is the turbulence of the ambient atmosphere for ground based telescopes known as seeing, which results in a smearing effect of the stellar disc.

This analogy is true for a long term exposure with the integration time being longer than the changing of the atmospheric conditions, which is in the order of milliseconds. But still, this is an effect of the integration time and not a real smearing of the stellar disc. Seeing results in a moving stellar disc. So the position of the stellar disc is permanently changed but the shape of the stellar disc remains constant.

So the effect of the geometrical extension of the disc is not directly affected by the seeing. Seeing, especially when using a spectrograph with a small slit, provokes a light loss when the seeing disc of the star is larger than the slit.

Having an extended stellar disc, stellar light comes from different points on the disc with an angular displacement. Considering two monochromatic point sources P and P' at opposite sides of the limb of the stellar disc with a spatial separation of $|\overline{PP'}|$ as illustrated in figure 2.3 the spectroscopically relevant component along the dispersion axis of the angular distance is given by $\phi(\eta) = |\overline{PP'}| \cdot \cos\eta$. η is the angle between the dispersion axis x of the spectrograph and $|\overline{PP'}|$. At the grating, the angular separation is transfered into the entrance angle differential δ_α by the telescope magnification that depends on the properties of the used spectrograph.

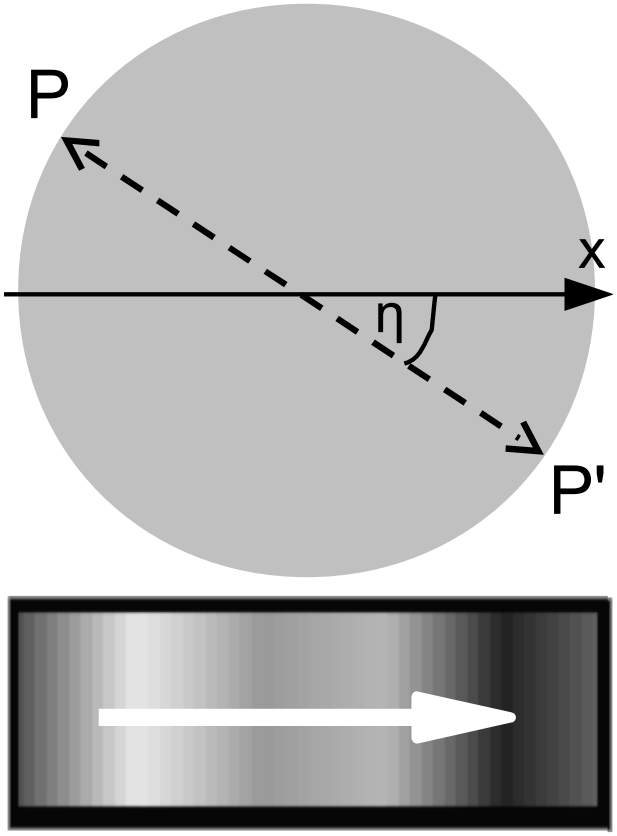

Figure 2.3: Scheme of an extended stellar disc with two points P and P' at the opposite limb that have an angular displacement of $|\overline{PP'}|$. The color bar with the white arrow represents the dispersion axis x of the spectrograph. The spectroscopically relevant component for the angular distance of two points P and P' is $\phi(\eta) = |\overline{PP'}| \cdot \cos\eta$.

Using a combination of a spectrograph and a telescope of a certain diameter D, the energy flux transmission relation between the flux coming from the source on the sky through the telescope to the spectrograph's grating is important, which leads to a quantity called the *étendue* U (see Schroeder (1987) for further details). The étendue is the product of the solid angle S and the area of the used telescope or collimator A. The étendue is conserved

$$U = S \cdot A = const$$

all over the optical path.

This equation is also valid in one dimension where

$$\phi D = const$$

with ϕ being an angular diameter and D the linear diameter of the optical element. Therefore, with a light source of angular diameter ϕ_1 and a telescope mirror diameter of D_1 the product must be conserved at the spectrograph with a collimator beam diameter of D_2 and the angular diameter ϕ_2 at that position according to

$$\phi_1 D_1 = \phi_2 D_2$$

or sorted by the resulting angle

$$\phi_2 = \frac{D_1}{D_2}\phi_1.$$

$M_{\text{telescope}} = D_1/D_2$ is the magnification of the telescope system.

Since the mirror diameter is much greater than the collimator beam diameter, a large magnification factor must be applied to the angular diameter on the sky of an extended source depending on the used telescope/spectrograph combination.

The high-resolution spectrographs used in todays 8 to 10 m class telescopes are typically echelle spectrographs. This type of spectrographs uses a blazed diffraction grating as dispersion element.

In general, neighboring rays of collimated light interfere at the grating with each other and the *grating equation* is given by the formula for positive interference

$$m\lambda = d(\sin\alpha + \sin\beta)$$

with m being the diffraction order, λ the wavelength, d the groove spacing of the grating, α the incident (entrance) angle and β the diffraction (exit) angle. This is illustrated in figure 2.4. For the general case, the out-of-plane angle γ would have to be accounted for with a factor of $\cos\gamma$ to the optical path difference but for such small sources as stellar discs $\cos\gamma = 1$ so it can be neglected.

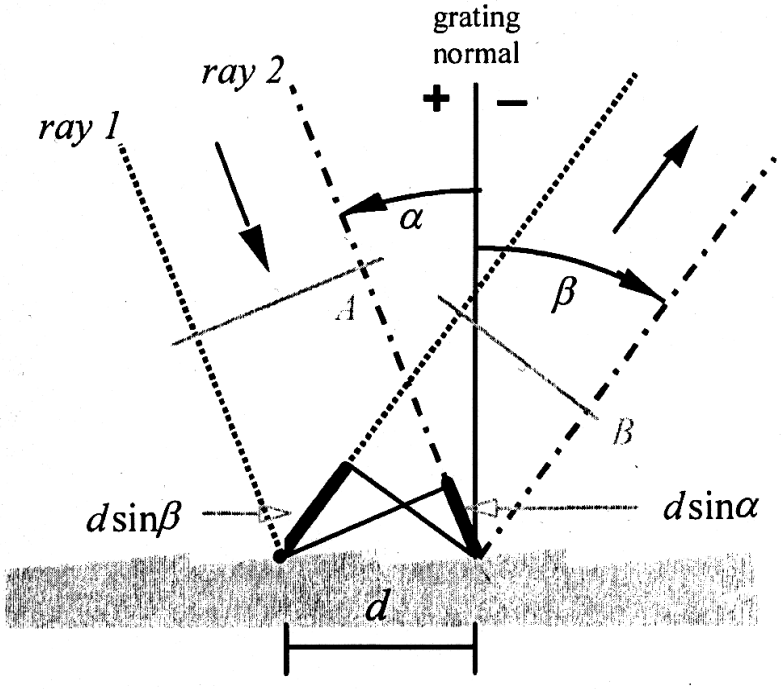

Figure 2.4: Scheme of a diffraction grating with groove spacing d. The incoming parallel rays 1 and 2 separated by one groove spacing d are incident with the angle α. They are in phase with each other at wavefront A. Positive interference is given when these rays are in phase at the diffracted rays of wavefront B (of diffraction angle β) if the path difference $d\sin\alpha + d\sin\beta$ is a multiple of the wavelength, which leads to the grating equation (taken from Palmer 2005).

The differentiated form of the grating equation is

$$m\ \delta\lambda = d(\delta\alpha\cos\alpha + \delta\beta\cos\beta)$$

Light of the same wavelength λ coming from two different points P and P' on the stellar surface has an angular separation. Only the component of the angular distance projected on the dispersion axis of the spectrograph $\Phi = \Phi(\eta) = \left|\overline{PP'}\right|\cos(\eta)$ is spectroscopically relevant for the geometric wavelength shift as illustrated in figure 2.1).

That angular separation Φ on the sky transfers into an incident angle differential $\delta\alpha$ according to the telescope magnification by the conservation of the étendue (as described in the preceding paragraph)

$$D\Phi = W_\alpha\ \delta\alpha$$

here with the telescope's mirror diameter D and the incident beam diameter W_α.

Then the differential $\delta\beta$ of the diffracted (exit) beam due to the spatial angular separation Φ including the telescope magnification D/W_β is

$$\delta\beta = \Phi(\eta)\frac{D}{W_\beta}$$

with the grating length L and the beam diameters $W_\alpha = L\cos\alpha$ and $W_\beta = L\cos\beta$ at the grating.

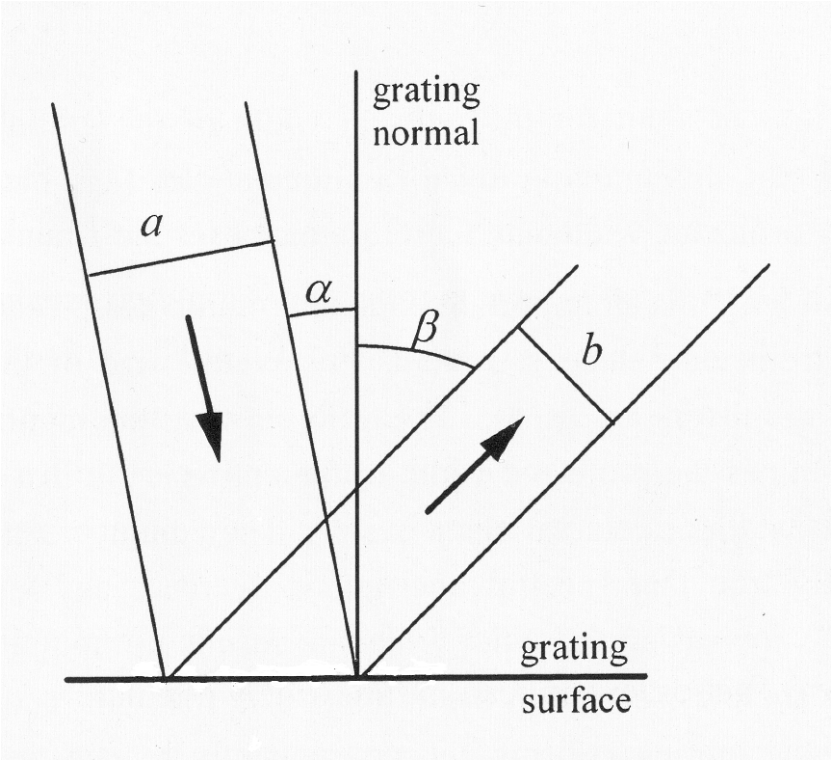

Figure 2.5: Scheme of the anamorphic magnification being the ratio b/a of the diameters of the incident and diffracted beams of light at the grating (taken from Palmer (2005)).

The infalling (a) and outgoing (b) beam diameters at the grating are shown in figure 2.5. The ratio $W_\beta/W_\alpha = b/a$ is called the *anamorphic magnification*, which connects the incident angle α with the diffracted angle β by $|\Delta\beta/\Delta\alpha| = \cos\alpha/\cos\beta = b/a$.

The transfer of the angular dispersion $\delta\beta$ to the wavelength shift $\delta\lambda$ using $0 \approx \delta\alpha << \alpha$ (i.e., $\delta\alpha = 0$) follows by division of the differentiated grating equation by the original grating equation

$$\begin{aligned} m\delta\lambda_{|\delta\alpha=0} &= d(\delta\beta\cos\beta) \\ m\lambda &= d(\sin\alpha + \sin\beta) \end{aligned}$$

division of both results in

$$\frac{\delta\lambda}{\lambda} = \frac{\delta\beta\cos\beta}{(\sin\alpha + \sin\beta)}$$

Sorted by $\delta\beta$ this transfers to

$$\delta\beta = \frac{\delta\lambda}{\lambda}\frac{(\sin\alpha + \sin\beta)}{\cos\beta} = \frac{\delta\lambda}{\lambda}\frac{T}{W_\beta}$$

Inserting of $\delta\beta_\phi$ from above leads to

$$\frac{\delta\lambda_\Phi}{\lambda} = \frac{D\Phi}{L(\sin\alpha + \sin\beta)}$$

then the wavelength shift is

$$\delta\lambda_\Phi = \lambda\frac{D\Phi}{L(\sin\alpha + \sin\beta)} = \lambda\frac{D\Phi}{T}$$

and finally the equivalent velocity

$$\frac{v_\Phi}{c} = \frac{D\Phi}{T}$$

with the *grating depth* $T = L(\sin\alpha + \sin\beta)$ and c the speed of light.

2.3 Combined effect and profile

2.3.1 Combined effect

The combined wavelength shift resulting from the rotational Doppler effect and the geometric effect is simply the sum of both shifts

$$\begin{aligned} \Delta\lambda_{\text{tot}} &= \Delta\lambda_{\text{rot}} + \Delta\lambda_\Phi \\ \Delta\lambda_{\text{tot}} &= \lambda\left(\frac{\Omega\sin i}{c}\right)x + \lambda\frac{D\Phi(\eta)}{T} \end{aligned}$$

or in the velocity regime

$$\begin{aligned} \frac{v_{\text{tot}}}{c} &= \frac{v_{\text{rot}}}{c} + \frac{v_\Phi}{c} \\ \frac{v_{\text{tot}}}{c} &= \left(\frac{\Omega\sin i}{c}\right)x + \frac{D\Phi(\eta)}{T} \end{aligned}$$

with x the distance to the projected rotation axis and the alignment angle η between the dispersion axis and the the rotation axis of the star. So the sum and, therefore, the caused broadening when integrating over the stellar disc depends on the alignment of the dispersion axis and the projected rotation axis of the star. Since the dispersion axis is perpendicular to the slit axis this is also called *spin-slit alignment*.

2.3.2 The combined broadening profile

For the integration over the stellar disc the same coordinate system as introduced in section 2.1 will be used here (see figure 2.1 in section 2.1) with the projected rotation axis of the star being equal to the y axis. Therefore, the rotational Doppler shift depends only on the x coordinate and the corresponding wavelength shift is

$$\Delta\lambda_{\mathrm{rot}} = \lambda\frac{\Omega\sin i}{c}x$$

At the limb of the equator $x = R$ with R the radius of the star. Spherical symmetry is assumed and limb darkening is neglected here but will be implemented later in section 3.1.1.

Also chosen here is the special case where the dispersion axis of the spectrograph is (anti-) parallel aligned to the x axis, $\eta = 0°$, $\cos\eta = 1$ ($\eta = 180°$, $\cos\eta = -1$). Expressing the angular scale with the x coordinate the geometrical wavelength shift is

$$\Delta\lambda_{\Phi} = \pm\lambda\frac{D}{T}\frac{\Phi}{R}x$$

with Φ the angular diameter of the stellar radius R and x the same coordinate as for $\Delta\lambda_{\mathrm{rot}}$.

The summed wavelength shift is

$$\Delta\lambda = \Delta\lambda_{\mathrm{tot}} = \Delta\lambda_{\mathrm{rot}} + \Delta\lambda_{\Phi} = \lambda\left(\frac{\Omega\sin i}{c} \pm \frac{D}{T}\frac{\Phi}{R}\right)x$$

At the limb with $x = R$ the maximal wavelength shift is

$$\Delta\lambda_{\mathrm{max}} = \lambda\left(\frac{v_{\mathrm{rot}}\sin i}{c} \pm \frac{D\Phi}{T}\right)$$

Therefore,

$$\frac{x}{R} = \frac{\Delta\lambda}{\Delta\lambda_{\mathrm{max}}}$$

and

$$x = R\frac{\Delta\lambda}{\Delta\lambda_{\mathrm{max}}}$$

which leads to

$$\frac{dx}{d\Delta\lambda} = \frac{R}{\Delta\lambda_{\mathrm{max}}}$$

and

$$dx = \frac{R}{\Delta\lambda_{\mathrm{max}}}d\Delta\lambda$$

For the spherical stellar disc the circular border is defined by $R^2 = x^2+y^2$, which transforms to

$$y^2 = R^2 - x^2 = R^2\left(1 - \left(\frac{x}{R}\right)^2\right) = R^2\left(1 - \left(\frac{\Delta\lambda}{\Delta\lambda_{\max}}\right)^2\right)$$

The flux is given by $F_\nu = \oint I_\nu \cos\theta dS$ with the specific intensity I_ν (that is shifted), the angle θ to the normal of the incremental surface element dA of the star of radius R and the solid angle dS. With $dS = dA/R^2$ and using the coordinate system defined before in figure 2.1 we get $dx\ dy = dA\cos\theta$ so that $dS = dx\ dy/(R^2\cos\theta)$.

The line profile $H(\lambda) = I_\nu/I_c$ is defined as the ratio of the line spectrum intensity to the continuum intensity I_c. For a rotating star we get

$$\frac{F_\nu}{F_c} = \frac{\oint H(\lambda-\Delta\lambda)I_c\cos\theta dS}{\oint I_c\cos\theta dS}$$

Using the coordinate transfer dx to $d\Delta\lambda$ as defined above and the circular shape of the stellar disc with $y_1 = R\left(1 - \left(\frac{\Delta\lambda}{\Delta\lambda_{\max}}\right)^2\right)^{1/2}$ we can transform

$$\frac{F_\nu}{F_c} = \frac{\int H(\lambda-\Delta\lambda)I_c(dxdy/R)}{\oint I_c\cos\theta dS} = \frac{\int_{-\Delta\lambda_{\max}}^{\Delta\lambda_{\max}} H(\lambda-\Delta\lambda)\int_{-y_1}^{y_1} I_c(dy/R)(d\Delta\lambda/\Delta\lambda_{\max})}{\oint I_c\cos\theta dS}$$

We define

$$G(\Delta\lambda) \equiv \frac{1}{\Delta\lambda_{\max}}\frac{\int_{-y_1}^{y_1} I_c(dy/R)}{\oint I_c\cos\theta dS}$$

for $|\Delta\lambda| \le \Delta\lambda_{\max}$ and $\equiv 0$ for $|\Delta\lambda| > \Delta\lambda_{\max}$.

Then we get

$$\frac{F_\nu}{F_c} = \int_{-\infty}^{\infty} H(\lambda-\Delta\lambda)G(\Delta\lambda)d\Delta\lambda = H(\lambda)\otimes G(\lambda)$$

The resulting spectrum is a convolution ($\otimes$) of the line profile $H(\lambda)$ of an unbroadened star (in the sense of rotation and angular diameter) with the *broadening profile* $G(\lambda)$.

Neglecting the limb darkening, the continuum flux is constant over the stellar disc $I_c = I_c^0 = const$. Then the integration of the broadening profile G can be carried out over the stellar disc resulting in

$$G(\Delta\lambda) = \frac{2}{\pi\Delta\lambda_{\max}}\sqrt{1 - \left(\frac{\Delta\lambda}{\Delta\lambda_{\max}}\right)^2}$$

The resulting broadening profile has the classical shape of the stellar disc also to be found in the pure rotational broadening profile but with the combined wavelength shift from the rotational Doppler shift and the geometrical shift due to the angular extension of the stellar disc.

2.3.3 Spin-slit alignment

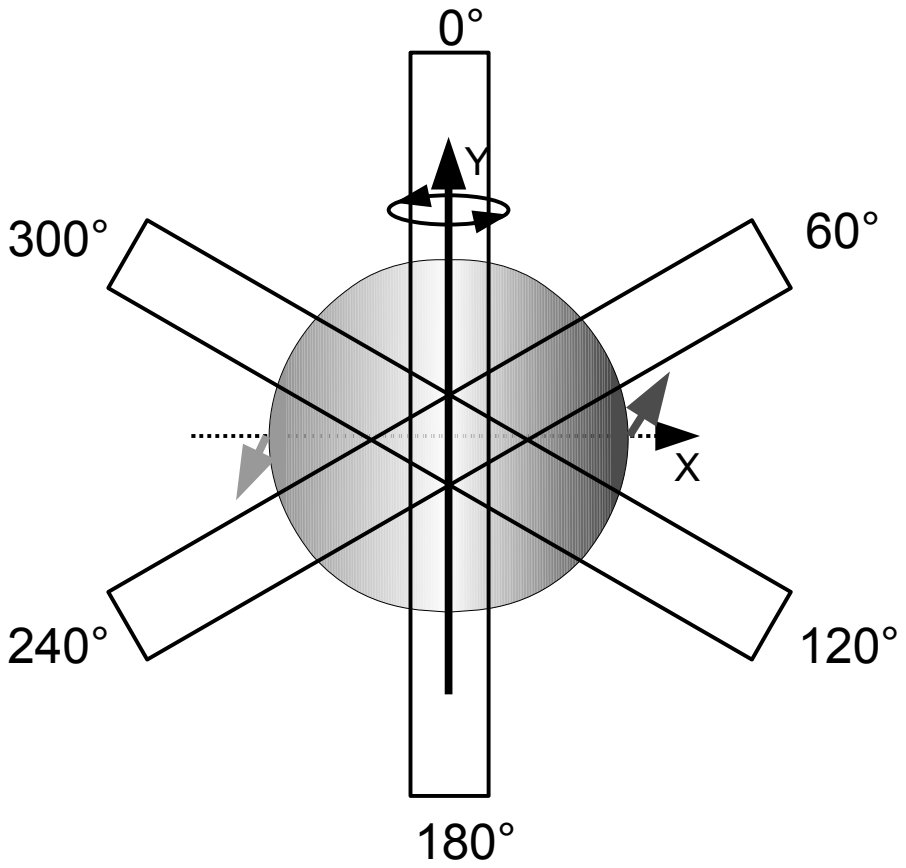

Figure 2.6: Scheme of the stellar disc's rotational Doppler shift distribution probed by different spin-slit alignments. The used slit orientations are indicated by the rectangles with their angular orientation printed at the ends. The scale does not represent the reality where the slit is much broader than the star. For this example, the maximal (minimal) combined broadening effect is achieved with the top (bottom) slit orientation with the slit axis being (anti-) aligned with the spin axis.

The combined wavelength shift found in the resulting broadening profile has been calculated for the two extreme situations of the spin-slit alignment. In the case where the geometrical part of the wavelength shift is positively added to the rotational Doppler part the broadening is maximal. When the geometrical part is subtracted from the rotational part the overall broadening is minimal. In general, a sinusoidal progression of the broadening with the chosen spin-slit alignment is expected.

An illustration of the different spin-slit alignments with the rotating stellar disc can be found in figure 2.6. The slit orientations are varied between zero and 360° in steps of 60°. This is just a scheme, in reality the slit is much larger than the actual star's apparent diameter.

Therefore, analyzing identical observations except for different spin-slit alignments for broadening deviations can in principle reveal the absolute position angle of the projected rotation axis of a rotating star.

Chapter 3

Estimations of the line broadening effect

3.1 Numerical line profiles

To produce a realistic estimation of the combined line broadening effect, which is caused by the spin-slit alignment of stellar rotation and geometrical extension of the stellar disc, realistic line profiles are needed.

A stellar absorption line can be constructed by the convolution of the intrinsic line profile with the rotation profile of the projected stellar rotation velocity $v_{\mathrm{rot}} = v \sin i$, with i the inclination angle and v the full rotation velocity when the system is viewed edge on ($i = 90°$).

Furthermore, the stellar disc has no homogeneous intensity distribution but the intensity declines from center to the limb, which is called limb darkening. This has to be taken into account when integrating over the stellar disc.

Since already the intrinsic profile, usually a Voigt profile, can not be calculated analytically, the estimations presented in this chapter are based on numerically calculated line profiles.

3.1.1 Limb darkening and rotation profile

Limb darkening is caused by the temperature distribution with optical depth and is also slowly varying with the wavelength. For a single spectroscopic line profile, the wavelength dependency can be neglected though. Also, as already mentioned in section 2.3.2, the star is assumed to be a spherical symmetric rigid rotating body neglecting differential rotation.

For the sun, the limb darkening can be easily observed even with very small telescopes. For the description of the limb darkening, the intensity profile $I(\mu)$ across the stellar disc is used with $\mu = \cos\theta = \sqrt{1 - r_R^2}$ and r_R the relative radius and θ as defined in section 2.3.2.

Here, a linear limb darkening law has been adopted as introduced by Gray (1976) using $I_c = I_c^0(1 - \epsilon + \epsilon \cos\theta)$ with I_c the continuum intensity in general and at the center I_c^0 of the disc, ϵ the limb darkening parameter ($0 < \epsilon < 1$) and $\mu = \cos\theta$.

The limb darkening parameter is wavelength dependent. The single parameter ϵ has been chosen so that the used limb darkening model is in good agreement with the common

P5(μ) polynomial fit (power = 5) model used by Neckel & Labs (1994). A comparison of both models for a wavelength of $\lambda \approx 6000$ Å can be seen in figure 3.1 showing only small differences.

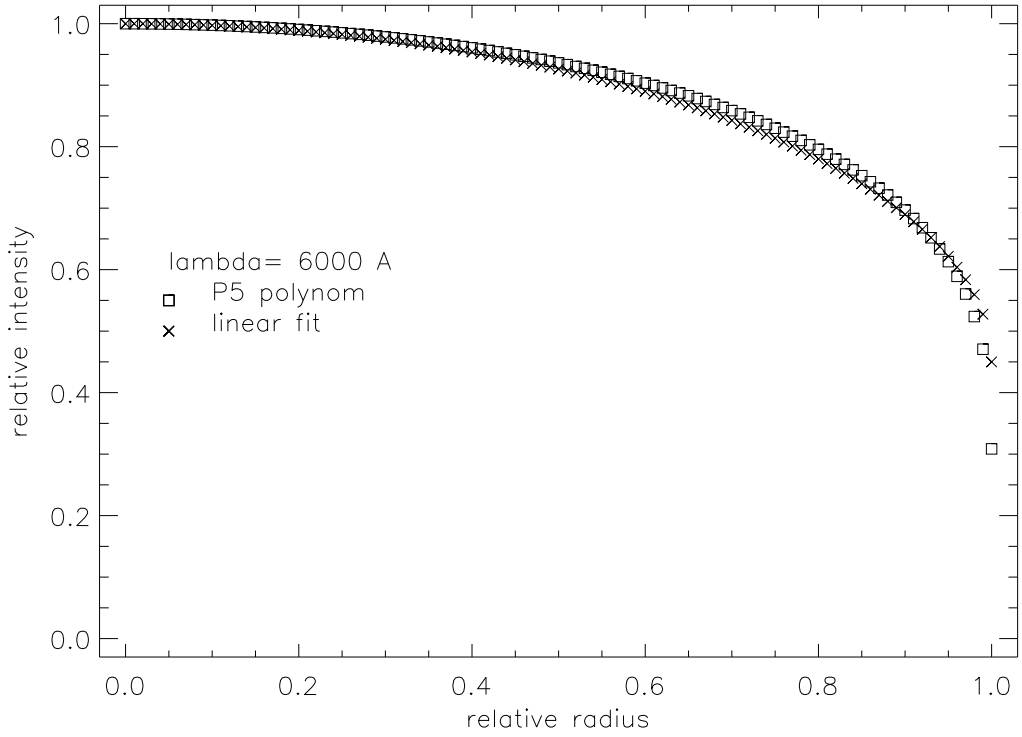

Figure 3.1: Solar limb darkening profile from a 5th order polynomial (P5(μ), squares) of Neckel & Labs (1994) and the linear fit (x) used in this work for a wavelength of $\lambda = 6000$ Å. The deviations between both methods are small.

In general, the linear limb darkening model declines a little faster until it crosses the P5 model near the limb staying usually within a few percent range of the P5 model. The small deviations justify the use of the simpler linear limb darkening model.

Starting from section 2.3.2 the rotational broadening profile is given by

$$G_{\rm rot}(\Delta\lambda) \equiv \frac{1}{\Delta\lambda_{\rm max}} \frac{\int_{-y_1}^{y_1} I_c(dy/R)}{\oint I_c \cos\theta dS}$$

Now we implement the linear limb darkening law using $I_c = I_c^0(1 - \epsilon + \epsilon\cos\theta)$ for the integration over the stellar disc.

The denominator integral $\oint I_c \cos\theta dS$ transfers to

$$I_c^0(1-\epsilon)\int_0^{2\pi} d\Phi \int_0^{\pi/2} \sin\theta\cos\theta\ d\theta \ + \ I_c^0\epsilon\int_0^{2\pi} d\Phi \int_0^{\pi/2} \sin\theta\cos^2\theta\ d\theta$$

Using the integral formula $\int \sin\theta\cos\theta\ d\theta = 1/2\sin^2\theta$ and $\int \sin\theta\cos^2\theta\ d\theta = 1/3\cos^3\theta$ the denominator integral finally is

$$\oint I_c \cos\theta\ dS = \pi I_c^0 \left(1 - \frac{\epsilon}{3}\right)$$

The numerator integral $\int_{-y_1}^{y_1} I_c \, dy/R$ transfers by using $\cos\theta = \sqrt{R^2-(x^2+y^2)}/R$ to

$$\frac{2I_c^0}{R}\int_0^{y_1}(1-\epsilon) \; + \; \frac{\epsilon}{R}\sqrt{R^2-(x^2+y^2)}\, dy$$

With the help of $\int \sqrt{a^2-y^2}dy = 1/2(y\sqrt{a^2-y^2}+a^2 \arcsin y/a)$ and $a^2 = R^2-x^2 = (y_1)^2$ follows

$$\int_{-y_1}^{y_1} I_c \, dy/R = 2I_c^0(1-\epsilon)\left[1-\left(\frac{\Delta\lambda}{\Delta\lambda_{\rm max}}\right)^2\right]^{1/2} \; + \; \frac{\pi\epsilon I_c^0}{2}\left[1-\left(\frac{\Delta\lambda}{\Delta\lambda_{\rm max}}\right)^2\right]$$

Both numerator and denominator form the rotation profile including limb darkening that is given by

$$G_{\rm rot}(\Delta\lambda) = \frac{2(1-\epsilon)}{\Delta\lambda_{\rm max}\pi(1-\epsilon/3)}\left[1-\left(\frac{\Delta\lambda}{\Delta\lambda_{\rm max}}\right)^2\right]^{1/2} + \frac{\epsilon}{2\Delta\lambda_{\rm max}(1-\epsilon/3)}\left[1-\left(\frac{\Delta\lambda}{\Delta\lambda_{\rm max}}\right)^2\right]$$

An illustration of the rotation profile ($v_{\rm rot} = 4$ km/s) with and without limb darkening can be found in figure 3.2.

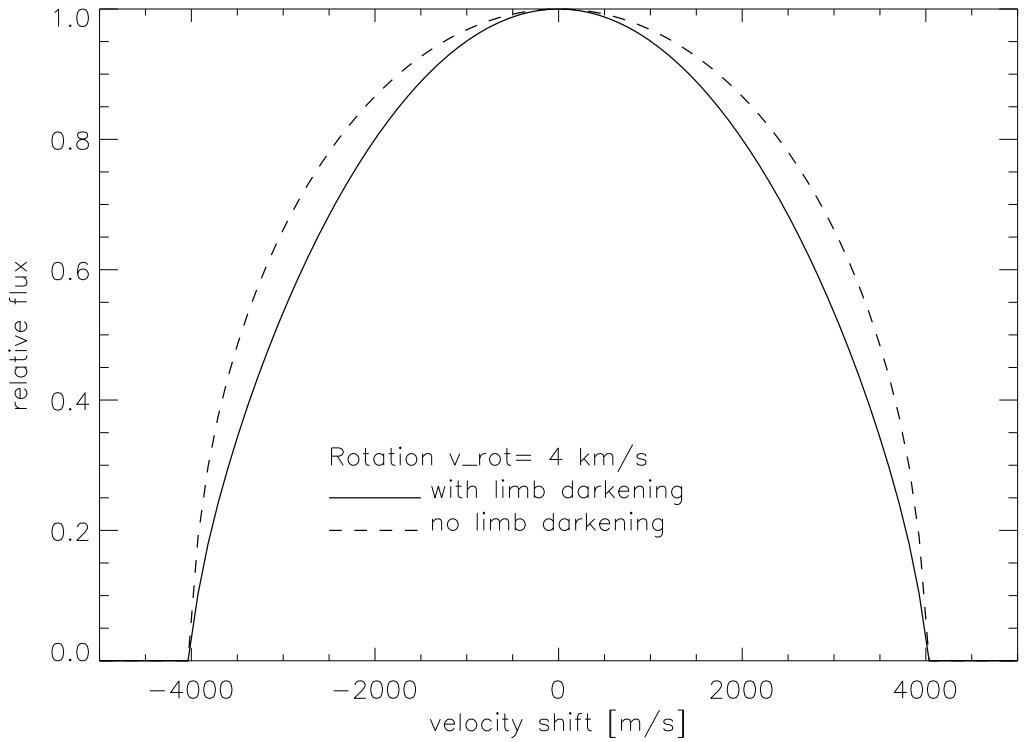

Figure 3.2: Height normalized rotation profile with a rotation velocity of $v_{\rm rot} = 4$ km/s with (solid line) and without (dashed line) limb darkening.

Such a rotation profile with limb darkening (for a mean wavelength of $\lambda \approx 5500$ Å of the UVES middle CCD chip as used for the observations) will always be used in the following.

To account for the geometrical effect, two stellar line profiles will be calculated regarding the maximal ($v_{\rm rot} + v_{\rm geo}$) and minimal ($v_{\rm rot} - v_{\rm geo}$) broadening or parallel/antiparallel spin-slit alignment, respectively.

3.1.2 The Voigt profile

The intrinsic line profile is based on a series of broadening effects, which can be sorted by two types:

- Doppler profile like collisional broadening effects and
- Lorentzian profile like dispersional broadening effects

This is important since the broadening widths of Lorentzian profiles can be added up linearly to $\Gamma = \sum \gamma_i$ while the broadening widths of Gaussian like Doppler profiles can be added up squared $v_{\mathrm{Dop}}^2 = \sum v_j^2$.

This reduces the intrinsic line profile to a convolution of a Lorentzian profile L with a Gaussian profile G, which is called the *Voigt* profile V

$$V(\Gamma, v_{\mathrm{Dop}}) = L(\Gamma) \otimes G(v_{\mathrm{Dop}})$$

The summed width Γ of the Damping or Lorentzian profile (mostly relevant for the line damping wings) consists of the widths of the natural atomic absorption γ_{nat} by the transition probability, the interaction of the atom in an electric field by the Stark effect (linear γ_2 or quadratic γ_4) and by the Van der Waals effect γ_6. The power of the radial dependency of the energy change is given by the indices like $\Delta E \propto 1/r^i$.

The quadratically summed Doppler width v_{Dop} consists mainly of the thermal broadening and the small scale oscillations going into the microturbulence. Stars with significant macroturbulence are not taken into account here. The microturbulence for solar like stars is typically in the range of $v_{\mathrm{micro}} = 1 - 2$ km/s.

The thermal broadening depends on the temperature T and the mass of the atom producing the absorption line. The summed Doppler velocity can be calculated by

$$v_{\mathrm{Dop}} = \sqrt{\frac{2k_B T}{m_a} + v_{\mathrm{micro}}^2}$$

with k_B the Boltzmann constant and m_a the atomic mass.

So the Gaussian width usually dominating the line core depends on the atomic mass of the species of the line of interest. In the visual regime iron shows lots of lines so we adopt $m_a = 56 \cdot m_H$ here together with a mean microturbulence of $v_{\mathrm{micro}} = 1.5$ km/s to calculate a typical Doppler width of $v_{\mathrm{Dop}} \approx 2$ km/s for a solar like star ($T = 5780$ K).

With the dimensionless velocity offset $u = \Delta v / v_{\mathrm{Dop}}$ and the damping parameter $a = \Gamma/(4\pi v_{\mathrm{Dop}})$, the Voigt function or profile can be expressed in the following way for a single line by

$$V(u, a) = \frac{a}{v_{\mathrm{Dop}} \pi^{3/2}} \int_{-\infty}^{\infty} \frac{\exp(-\tilde{u}^2)}{(u - \tilde{u})^2 + a^2} \, d\tilde{u}$$

For most of the following estimations, a typical Doppler width of $v_{\mathrm{Dop}} \approx 2$ km/s and a damping constant of $a = 0.15$ is used to calculate a fixed intrinsic width while varying other parameters. An illustration of such an intrinsic line can be found in figure 3.3 highlighted by the filled area in gray.

3.1.3 Determining halfwidths of convolved profiles

The goal in this chapter is to estimate the line broadening deviations between the two extreme cases where the broadening is maximal/minimal or the spin-slit alignment is parallel/antiparallel, respectively.

So we need a method to determine the width of a realistic line profile constructed from an intrinsic Voigt profile convolved with a rotation profile including limb darkening integrated over the stellar disc.

Since the procedure is done numerically the width can only be determined in the same way. The method uses the Half Width at Half Maximum (HWHM) of the computed line profile.

To determine the HWHM of the line profile it is first normalized by its height and then subtracted by 0.5 (i.e., the half of its normalized height), which is indicated by the dotted horizontal line at $y = 0.5$ in figure 3.3.

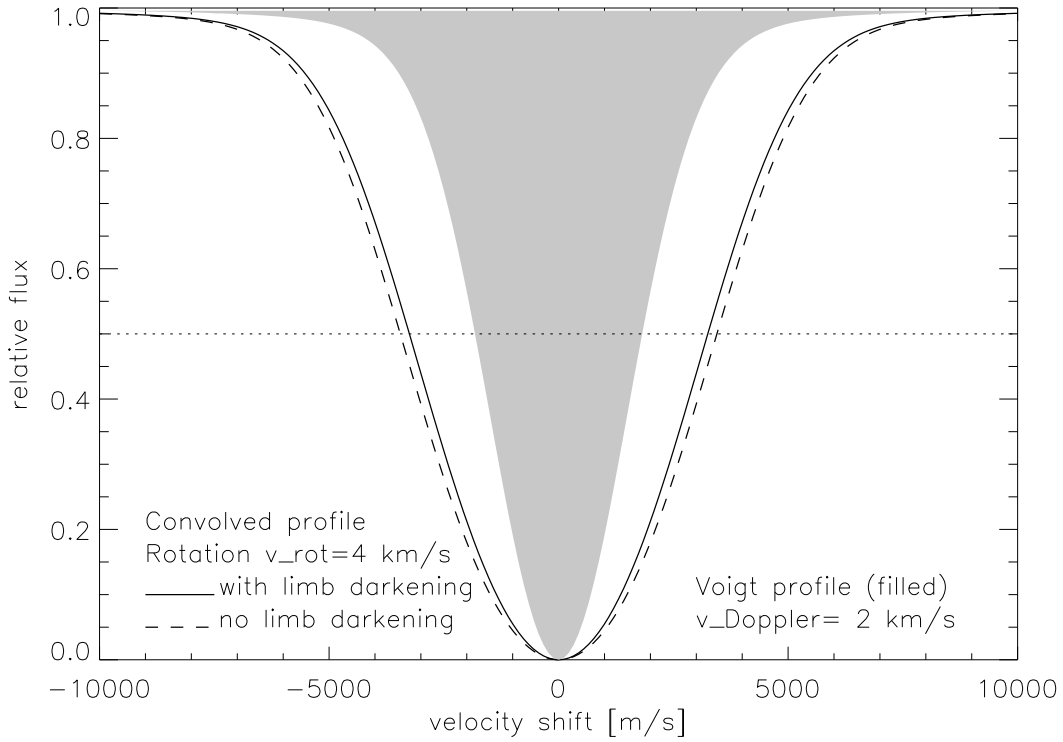

Figure 3.3: Height normalized line profile based on a Voigt profile ($v_{\rm Dop} = 2$ km/s, filled area) convolved with a rotation profile (rotation velocity $v_{\rm rot} = 4$ km/s) with (solid line) and without (dashed line) limb darkening.

With the relevant data points now being around the x-axis (zero line), data points from a small region around the x-axis are selected and fitted by a straight line. Then the root of this fitted line gives the HWHM of the line profile.

This HWHM method is applied always to two convolved line profiles originating from the same intrinsic profile $V_{\rm int}(u, a)$ and the rotation profile $G_{\rm rot}$ from the maximal or minimal broadening case, that is of $(v_{\rm rot} + v_{\rm geo})$ or $(v_{\rm rot} - v_{\rm geo})$, respectively. Usually, a fixed

geometrical width of $v_{\rm geo} = 10$ m/s (roughly corresponding to the radius of a solar like star in about 10 parsec distance as observed with UVES) is applied here.

Finally, the difference $\Delta width$ caused by the geometrical effect $v_{\rm geo}$ between the determined HWHM of the maximal and minimal broadening case is calculated and used to inspect the relation between this broadening difference and other involved parameters.

$$\Delta width = V_{\rm int}(u,a) \otimes G_{\rm rot}(v_{\rm rot} + v_{\rm geo}) \; - \; V_{\rm int}(u,a) \otimes G_{\rm rot}(v_{\rm rot} - v_{\rm geo})$$

Since the accuracy with which a line width or line width difference can be measured is inverse proportional to the the line width itself $\delta\Delta width \propto 1/width$, also the relative width deviation of the geometrical effect $\Delta width/width$ is important for the measurements and should be maximized if possible.

3.1.4 Line width approximation formula

With the ability to calculate the line widths numerically for a realistic convolved line profile it is possible to find an approximation formula to calculate the resulting line half width (HWHM) in a simple way from the profile input velocities namely the Doppler velocity $v_{\rm Dop}$ of the Voigt profile and the rotation velocity $v_{\rm rot}$ of the limb darkened rotation profile.

The intrinsic Voigt profile is calculated as defined in section 3.1.2 with the dimensionless velocity offset $u = \Delta v / v_{\rm Dop}$ and the damping parameter $a = \Gamma/(4\pi v_{\rm Dop})$, which is fixed to $a = 0.15$ here. That leaves the Doppler velocity $v_{\rm Dop}$ as the only free parameter.

For the rotation profile the formula

$$G_{\rm rot} = \frac{2(1-\epsilon)}{v_{\rm rot}\pi(1-\epsilon/3)} \left[1 - \left(\frac{\Delta v}{v_{\rm rot}}\right)^2\right]^{1/2} \; + \; \frac{\epsilon}{2v_{\rm rot}(1-\epsilon/3)} \left[1 - \left(\frac{\Delta v}{v_{\rm rot}}\right)^2\right]$$

is used with the fixed limb darkening parameter $\epsilon = 0.625$ for a wavelength range around 5500 Å. That leaves the rotational velocity $v_{\rm rot}$ the only free parameter here.

The stellar line is then calculated by a numerical convolution of both profiles $V(v_{\rm Dop}) \otimes G(v_{\rm rot})$. Finally, the line half width (HWHM) w is determined as described in section 3.1.3.

Beginning from a simple approximation of both the intrinsic and the rotation line profile by a Gaussian, the half width w can be calculated by the square-root of the sum of the squared individual widths $w_{gauss} = \sqrt{v_{\rm Dop}^2 \; + \; v_{\rm rot}^2}$. Instead, using the exponents of both velocities as free parameters α and β, a simple approximation formula can be formulated by

$$w = \sqrt{v_{\rm Dop}^{\alpha} \; + \; v_{\rm rot}^{\beta}}$$

With the help of the numerical line modeling including a mean limb darkening for a wavelength of about 5500 Å, a series of line half widths (HWHM) have been calculated from various combinations of Doppler ($v_{\rm Dop} = 0.5 \; - \; 12$ km/s) and rotation velocities ($v_{\rm rot} = 0.5 \; - \; 12$ km/s). An example of calculated line half width sequences by their rotation velocity and four different Doppler velocities can be found in figure 3.4 plotted as solid lines.

To find the parameters α and β for the approximation of the line half widths $w = \sqrt{v_{\rm Dop}^{\alpha} + v_{\rm rot}^{\beta}}$, the MPFIT package (see also section 5.2) has been used to find the best fit values with the series of numerically calculated widths. The best matching values are

$$\alpha = 1.9730 \pm 0.0003, \;\; \beta = 1.9247 \pm 0.0003$$

The fitted half widths (HWHM) are plotted as dashed lines in figure 3.4 showing an acceptable agreement between the approximation and the numerical line half widths for a simple evaluation of line widths.

For smaller intrinsic widths, the approximation is underestimating the line widths for higher rotation velocities, while for higher intrinsic widths, the approximation formula overestimates the line widths. Still, the general trend of the numerical line widths is represented by the used approximation formula.

Since both parameters are close to the exponents of the convolved Gaussian's resulting width, i.e., close to two, using the Gaussian approximation $w_{gauss} = \sqrt{v_{\rm Dop}^2 + v_{\rm rot}^2}$ is possible but the fitted exponents are to be preferred.

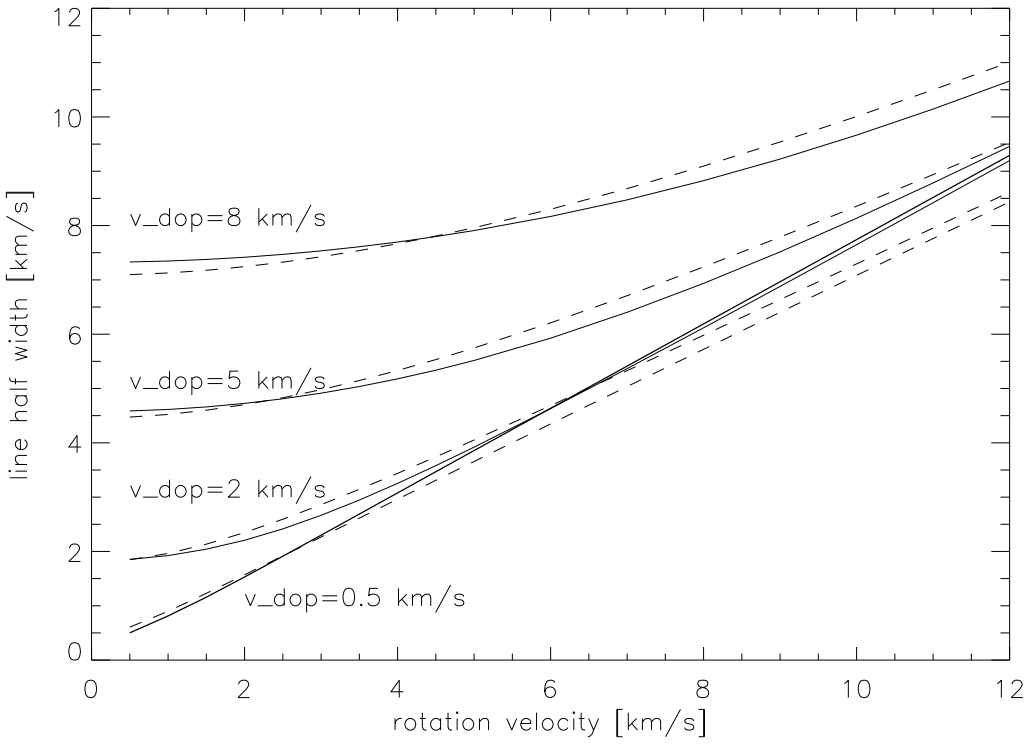

Figure 3.4: Distribution of line half widths (HWHM) for four different Doppler velocities with a sequence of rotation velocities. The numerically calculated line half widths are shown as solid lines with those from the approximation formula overplotted as dashed lines. The used formula for approximating the line half width w is given by $w = \sqrt{v_{\rm Dop}^{\alpha} + v_{\rm rot}^{\beta}}$ with the exponents best fitted by $\alpha \approx 1.973$ and $\beta \approx 1.925$.

A more flexible double polynomial approach given by

$$w = \sqrt{a_0 + a_1 \cdot v_{\rm Dop} + a_2 \cdot v_{\rm Dop}^2 + a_3 \cdot v_{\rm Dop}^3 \;\; + \;\; a_4 \cdot v_{\rm rot} + a_5 \cdot v_{\rm rot}^2 + a_6 \cdot v_{\rm rot}^3}$$

leads to only marginal better results than the used fit of the exponents but needs a much higher number of parameters and is therefore unfavorable.

3.2 Simulated broadening deviations

3.2.1 Intrinsic profile widths

Here, the dependency of the geometrically caused width difference with the intrinsic line width will be inspected. Except for the intrinsic line width, all other parameters are fixed, i.e., a geometrical effect of $v_{\rm geo} = 10$ m/s (of the stellar radius) and a rotation velocity of $v_{\rm rot} = 2$ km/s is always applied here.

The intrinsic line profile depends on the used species (atomic mass) and transition properties (excitation energy and oscillator strength) as well as the microturbulence. This variety of intrinsic line profiles is substituted here by a series of Doppler widths $v_{\rm Dop}$.

Also different damping parameters ($a = 0.15, 0.30$ and 0.50) are used for the calculations to study their influence. Higher damping makes the intrinsic line profile broader and enhances its damping wings.

The results of the absolute broadening deviations Δwidth with the intrinsic Doppler width $v_{\rm Dop}$ for the three different damping parameters a can be found in figure 3.5.

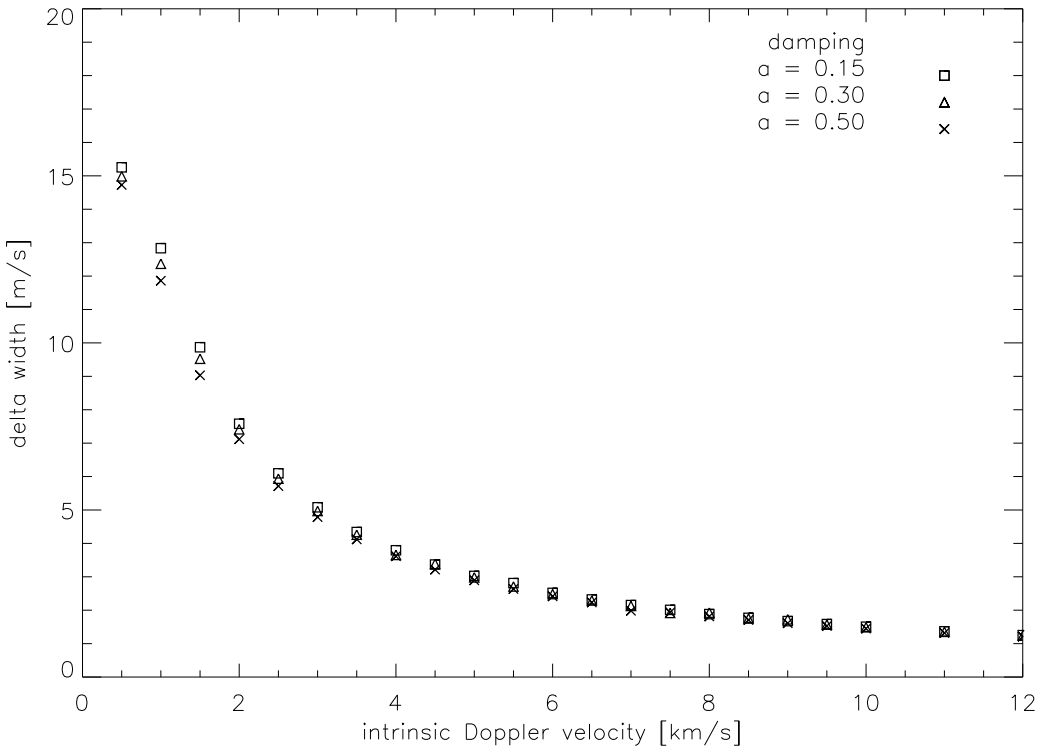

Figure 3.5: Calculated absolute Δwidths from different intrinsic width strengths (and a fixed rotation velocity of $v_{\rm rot} = 2$ km/s and geometrical width $v_{\rm geo} = 10$ m/s). Larger intrinsic widths are causing a smaller geometrical effect because the fraction of the rotation profile is decreasing. The influence of the damping parameter a (see different plot symbols) is small and therefore negligible.

The geometrical effect does not affect the intrinsic line width, it only enters the rotation profile. Therefore the intrinsic line width hinders the geometrically caused broadening

deviations Δwidth. The estimated Δwidth first falls with the intrinsic Doppler width until it slowly saturates to higher intrinsic Doppler widths.

The damping strength does only influence the width deviation to a larger degree as long as the intrinsic Doppler width dominates the profile. Since the intrinsic Doppler width can not be reduced below the microturbulence, the different damping has only minor influence on the width deviations and can be neglected except for extreme cases not handled here.

Coming to the width deviations relative to the maximum width ($v_{\rm rot} + v_{\rm geo}$), the situation is even more clear. The relative width deviation falls rapidly with the intrinsic Doppler width for small ones and then saturates to higher intrinsic widths.

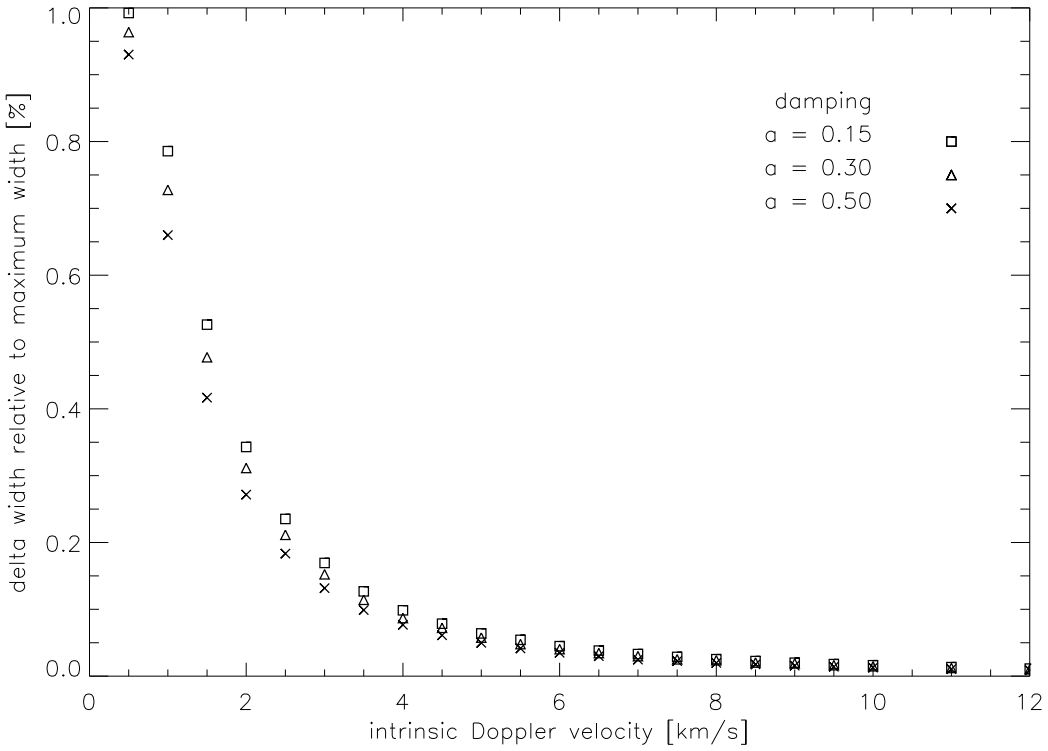

Figure 3.6: Calculated relative (%) Δwidths from different intrinsic width strengths (and a fixed rotation velocity of $v_{\rm rot} = 2$ km/s and geometrical width $v_{\rm geo} = 10$ m/s). It follows that smaller intrinsic widths are preferred for the measurement of the geometrical effect.

The influence of the damping parameter remains small, which justifies to fix it for small lines. The simulated results can be found in figure 3.6. Clearly, small intrinsic lines are preferred to measure the geometrically caused width deviations.

3.2.2 Rotation profile widths

The geometrical effect goes directly into the rotation profile since it is simply added to the rotation velocity for the two extreme cases of maximal and minimal broadening ($v_{\rm rot} \pm v_{\rm geo}$).

To estimate the effect of different rotation velocities, all other parameters have been fixed, i.e., the intrinsic profile width is set to $v_{\rm Dop} = 2$ km/s (damping $a = 0.15$) and the geometrical effect is set to $v_{\rm geo} = 10$ m/s while the rotation velocity is varied.

As can be seen at the results in figure 3.7, the geometrically caused width deviation Δwidth rises with the rotation velocity until the rotation profile dominates the convolved line profile and almost no further improvement can be gained, saturation is almost reached.

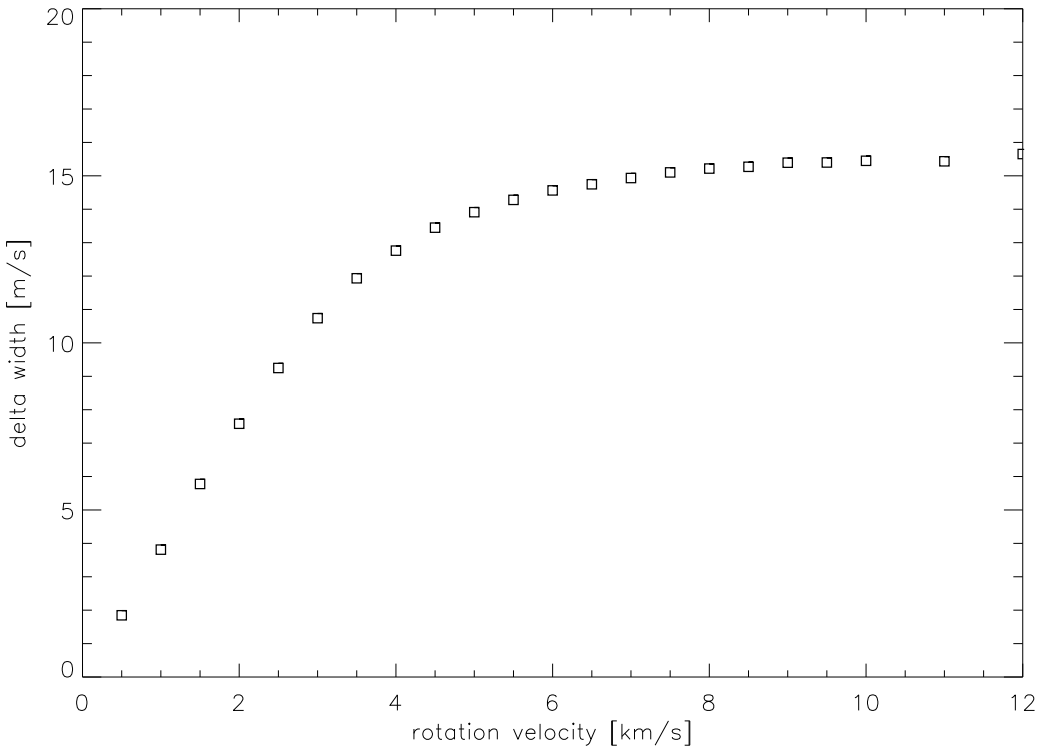

Figure 3.7: Calculated absolute Δwidths from different rotation velocities (and a fixed intrinsic width of $v_{\mathrm{Dop}} = 2$ km/s and geometrical width $v_{\mathrm{geo}} = 10$ m/s). The measured geometrical effect rises with the rotation velocity until saturation is reached.

To reach a high geometrical effect, the rotation velocity should not be too small, in fact it should be larger than the intrinsic Doppler velocity.

When looking at the width deviations relative to the line width as shown in figure 3.8, the situation is more complicated. As also concluded from the absolute width deviation, the rotation velocity should not drop below the intrinsic Doppler width v_{Dop}.

But since the overall width of the line grows with the rotation velocity, too large rotation velocities are unfavorable for the measurement accuracy. An optimal rotation velocity regime between one and 2.5 times the intrinsic Doppler width velocity is preferred for an accurate measurement of the geometrical effect.

Not shown is the very extreme case of a star, which has no apparent projected rotation velocity $v \sin i$, i.e., when viewed "pole-on" with the velocity component along the line of sight of the observer being $v_z = 0$. Then, the geometrical effect for a spherical symmetric star does not depend on the orientation of the slit anymore.

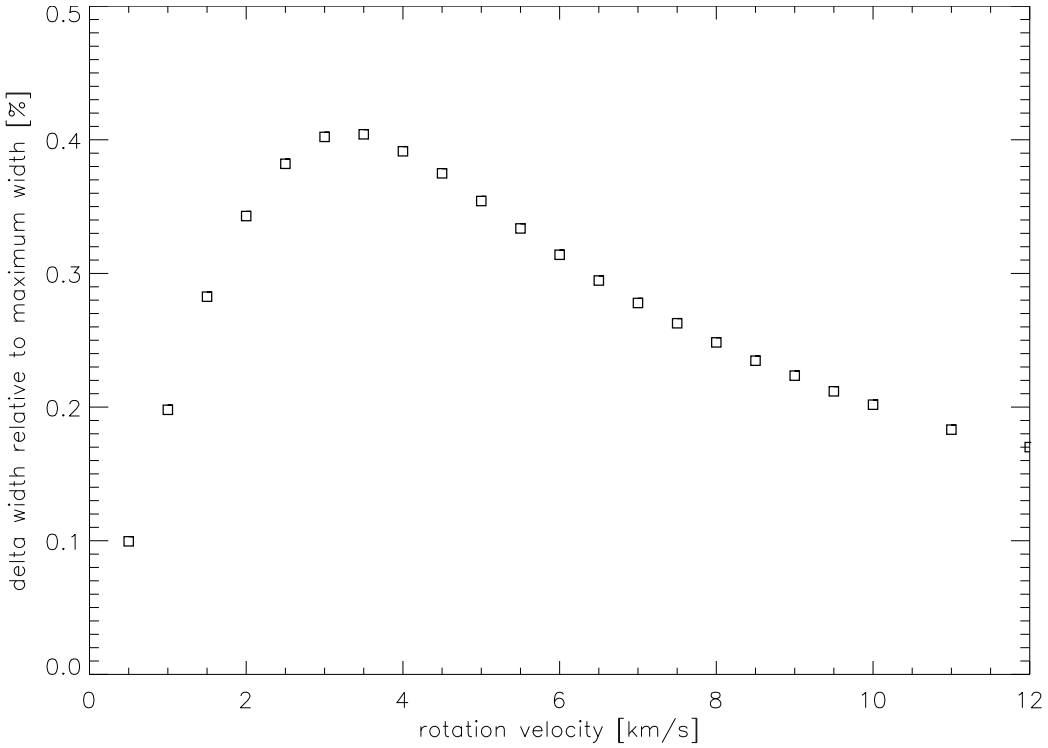

Figure 3.8: Calculated relative (%) Δwidths from different rotation velocities (and a fixed intrinsic width of $v_{\mathrm{Dop}} = 2$ km/s and geometrical width $v_{\mathrm{geo}} = 10$ m/s). A rotation velocity regime between one and 2.5 times of the intrinsic Doppler velocity is preferred to measure the geometrical effect.

3.2.3 Influence of the geometrical extension

As shown in the preceding chapter large angular diameter of stars are required to measure the differential broadening caused by different spin-slit alignments. Another important point is the instrumental configuration, the telescope magnification and the grating length have also to be taken into account for the resulting geometrical effect.

Except for the sun itself, all further stars are at least a few light years away from earth resulting in very small angular diameter. Therefore, only nearby stars can be candidates for observations.

Since the angles are small, the angular elongation of stellar radii can be estimated geometrically with the distance r and the radius R by

$$\Phi_R \approx \frac{R}{r}$$

transferring this to the arcsecond scale gives

$$\Phi_R/arcsec = \frac{360 \cdot 60 \cdot 60}{2\pi} \frac{R}{r} \approx 206265 \cdot \frac{R}{r}$$

Finally using the radius in units of solar radii and the distance in parsec we have

$$\Phi_R/arcsec = 4,65 \cdot 10^{-3} \; \frac{R/R_\odot}{r/pc}$$

With this formula we can estimate the angular size of radii of nearby stars by concluding their radii from their stellar type. For example a solar like star in 10 parsec distance has an angular diameter of $\Phi = 2 \cdot \Phi_R \approx 1 \cdot 10^{-3}$ arcseconds. Judging from this, angular diameter of nearby stars range in the milliarcsecond regime.

There are lots of stars that have smaller distances than 10 parsec. Besides, there are many stars that are larger than a solar like star and also lots of them being smaller than the sun. So we can expect a large variety of angular diameters and, hence, strengths of the geometrical effect in the order of several m/s using the UVES spectrograph.

Here, the influence of the geometrical effect on the line width deviation is inspected by fixing all other parameters like the intrinsic Doppler line width to $v_{\mathrm{Dop}} = 2$ km/s (damping parameter $a = 0.15$) and using only two rotation velocities of $v_{\mathrm{rot}} = 2$, 10 km/s while varying the geometrical width.

As illustrated in figure 3.9, the estimated width deviation rises linearly with the geometric effect as expected from its direct impact on the rotation profile described above. Also a larger rotation velocity results in a stronger absolute width deviation.

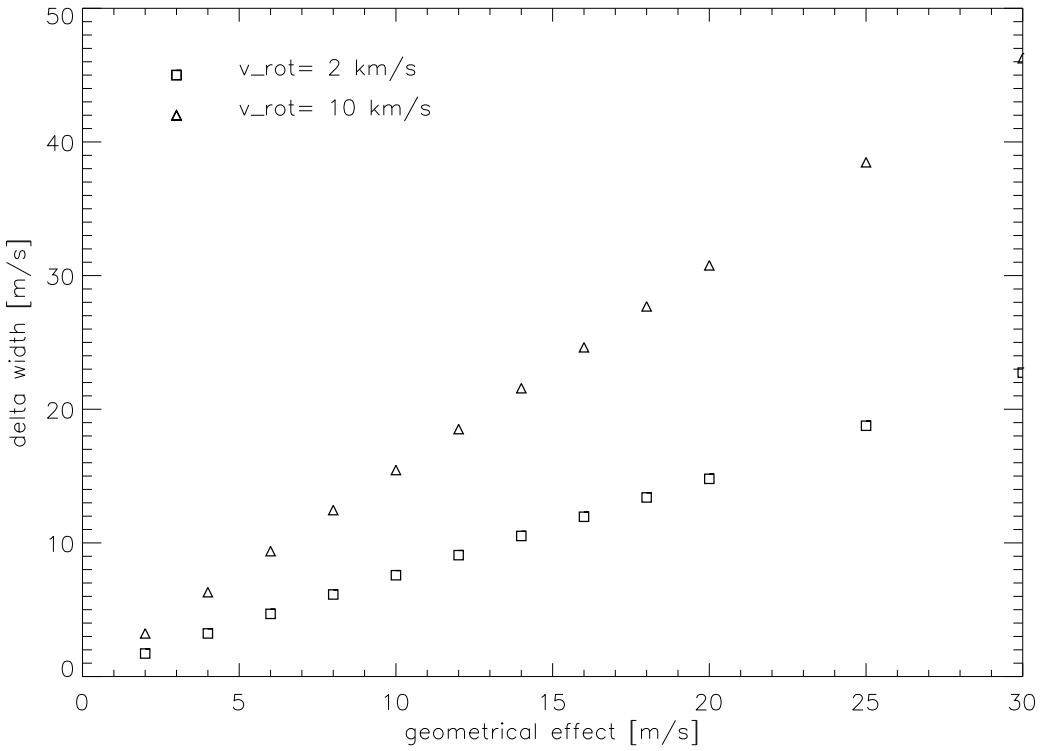

Figure 3.9: Calculated absolute Δwidths from different geometrical widths (angular diameters) (and a fixed intrinsic width of $v_{\mathrm{Dop}} = 2$ km/s). Two rotation velocity curves are shown, for $v_{\mathrm{rot}} = 2$ and 10 km/s. The measured geometrical effect rises linearly with the geometrical width.

Looking at the width deviation relative to the line width the situation has changed. As shown in figure 3.10, it is more favorable for the width measurement accuracy to select a target star with a rotation velocity near the optimal regime ($v_{\mathrm{rot}} \approx v_{\mathrm{Dop}} \ldots 2.5 v_{\mathrm{Dop}}$) than a much larger rotation velocity near saturation where the line width rises stronger than

the width deviation.

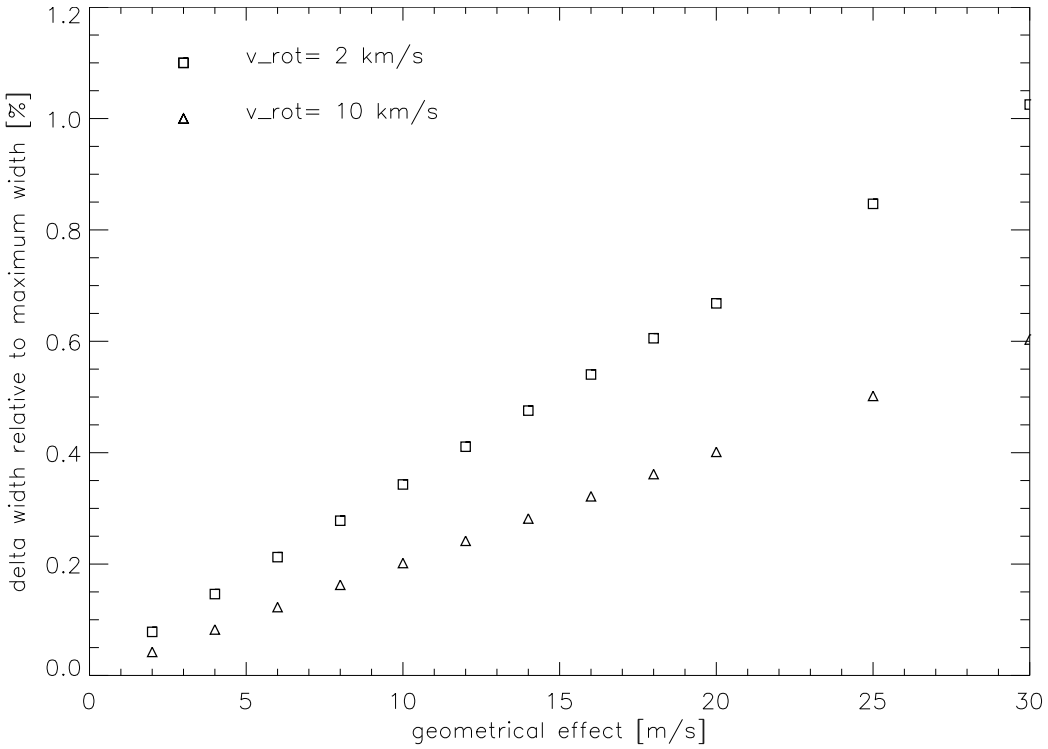

Figure 3.10: Calculated relative (%) Δwidths from different geometrical widths (angular radii) (and a fixed intrinsic width of $v_{\rm Dop} = 2$ km/s). Two rotation velocity curves are shown, for $v_{\rm rot} = 2$ and 10 km/s. The larger the angular diameter of the star the larger the geometrical effect but a smaller rotation velocity near the intrinsic Doppler width is more important than a larger angular diameter.

Therefore, it is more important to have a situation rather adjusted for the intrinsic Doppler and rotation velocity than a large but fast rotator. Nevertheless, target stars must reach a certain angular diameter to enable the width measurement, which is limited by the available spectral resolution, telescope magnification and reachable S/N.

In general, the larger the star (apparent diameter) the larger the measurable geometrical effect. Also the instrumental magnification is important here. Information on the actually observed target stars and their stellar parameters can be found in chapter 4.

3.3 Wavelength dependency

As already mentioned in the beginning of this chapter the limb darkening slowly varies with wavelength. Following Hestroffer & Magnan (1998) using a simplified model for showing the explicit wavelength dependency, the normalized brightness distribution over the stellar disc can be expressed by $I(\mu) = \mu^{\alpha}$.

The only parameter α can then be fitted with the $P5(\mu)$ polynomial fits derived for the sun and is given by $\alpha = -0.023 + 0.292/\lambda$ with λ in units of μm and valid for $\lambda^{-1} \leq 2.4\ \mu\mathrm{m}^{-1}$. Larger wavelengths result in less strong limb darkening.

The geometrical angular extension of a star does not depend on the wavelength. But the measurement of angular sizes of stars usually does. Two typical methods to measure the angular size of a nearby star are interferometry and lunar occultation.

The modeling for the diffraction scheme used for interferometry is often an uniformly bright disc. The real wavelength independent geometric disc size is calculated with a wavelength dependent correction factor adopted from a limb darkening model.

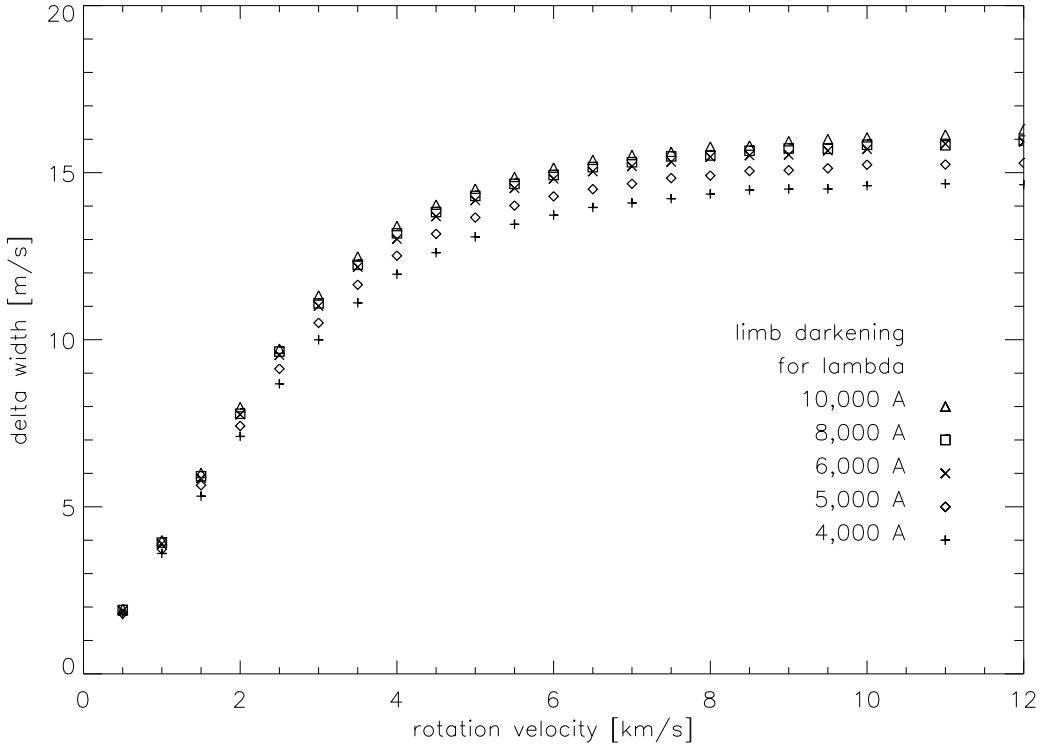

Figure 3.11: Calculated absolute Δwidths from different rotation velocities (and a fixed intrinsic width of $v_{\mathrm{Dop}} = 2$ km/s and geometrical width of $v_{\mathrm{geo}} = 10$ m/s). Several rotation velocity curves with different wavelength dependent limb darkening are shown. Larger wavelengths (i.e., less strong limb darkening) result in a larger geometrical effect.

For the lunar occultations, the wavelength dependency comes from atmospheric blurring and the final disc size is also corrected for it. So the stellar size is corrected for wavelength in both cases and has only one geometric size.

But the limb darkening itself is wavelength dependent, which enters the geometrical effect when integrating over the stellar disc. An example of the impact of this wavelength dependency can be found in figure 3.11 showing the rotation curves for different wavelengths. In general, larger wavelengths result in a stronger geometric effect.

The geometrically caused width deviations have been calculated using the matching limb darkening for five wavelengths from 4,000..10,000 Å. Here, a typical intrinsic Doppler width of $v_{\mathrm{Dop}} = 2$ km/s (damping $a = 0.15$) and geometrical width of $v_{\mathrm{geo}} = 10$ m/s has been fixed while varying the rotation velocity.

Interesting for this work is the typical UVES middle CCD wavelength range of 5,000-6,000 Å (RED600 nm setup) completely covered by the iodine cell. The difference in width

deviation from a line calculated at 6,000 minus those at 5,000 Å is shown in figure 3.12.

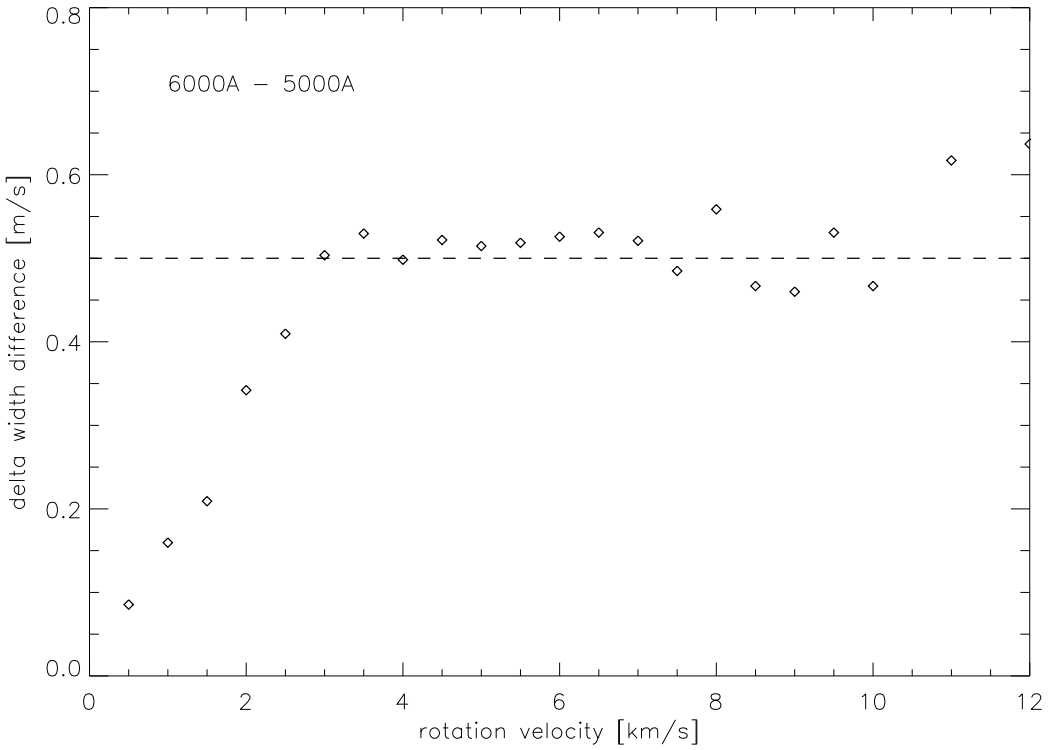

Figure 3.12: Calculated Δwidths residuals from different limb darkening (λ = 6000 and 5000 Å) and rotation velocities (and a fixed intrinsic width of v_{Dop} = 2 km/s and geometrical width of v_{geo} = 10 m/s). At the rotational saturation level the Δwidth residuals are in the order of 0.5 m/s. The scatter at the saturation level is caused by the numerical accuracy.

The difference in Δwidth is in the order of 0.5 m/s between the two edges of this wavelength range. Using a mean limb darkening for the whole range, Δwidth differences half of that (≈0.3 m/s) can be expected. Assuming a measurement accuracy of 3 m/s this contributes 10% to the geometrical effect at maximum.

Looking at the relative width deviations like illustrated in figure 3.13 the limb darkened rotation curves for different wavelengths have only minor influence on the optimal rotation velocity regime.

Therefore all results from the previous sections are still valid. Furthermore the effect of the wavelength dependent limb darkening can be corrected by a correction factor if necessary.

Regarding stellar candidates, it would be optimal to search for large (nearby) stars with small intrinsic widths and moderate rotation velocities. The rotation velocity should best be between one and 2.5 times the intrinsic Doppler velocity to enhance the combined broadening effect.

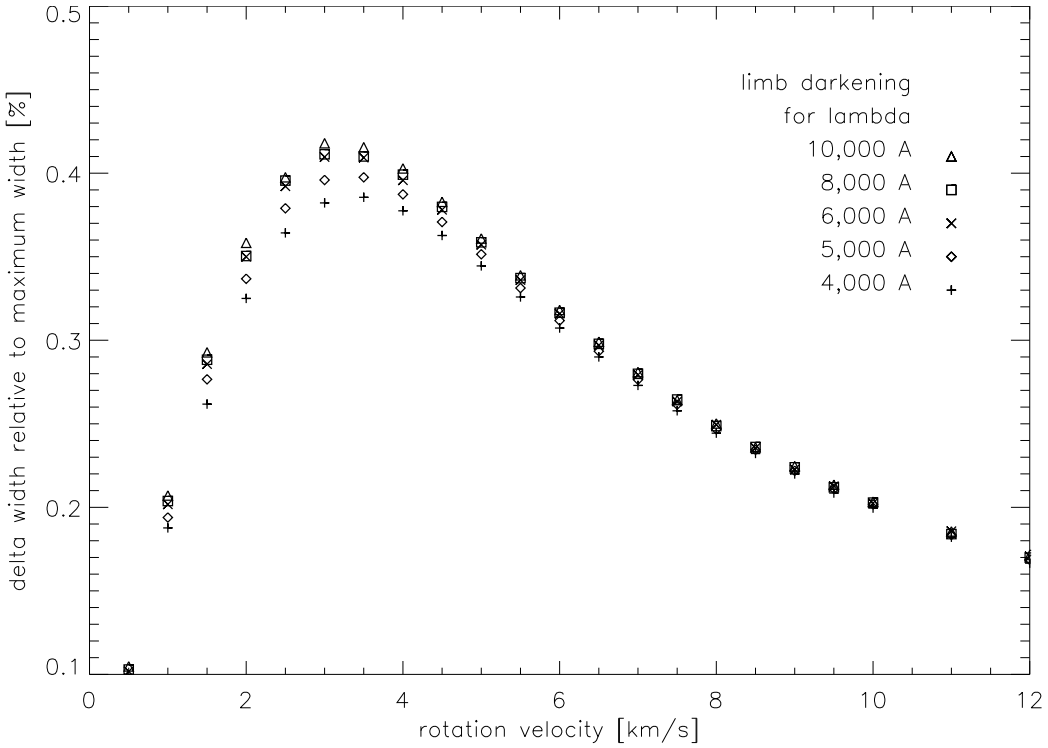

Figure 3.13: Calculated relative Δwidths (%) from different rotation velocities (and a fixed intrinsic width of $v_{\mathrm{Dop}} = 2$ km/s and geometrical width of $v_{\mathrm{geo}} = 10$ m/s). Several rotation velocity curves with different wavelength dependent limb darkening are shown. The limb darkening does not affect the optimal rotation velocity regime.

Chapter 4

Observations and Data Reduction

Three target stars, ϵ *Indi*, α *Tau* and *GJ 86* (and one reference star α Pav) have been selected to measure their orientation of the rotation axis. Since a modified method as used for the search for radial velocity shifts should be used here, there are equivalent requirements to the measurements. Therefore, a large telescope to achieve high Signal-to-Noise (S/N) ratios and telescope magnification combined with a high-resolution spectrograph including a gas reference cell was needed.

4.1 Instruments - UVES/VLT

The used telescope was the *Very Large Telescope* (VLT) of ESO at Cerro Paranal in Chile. One of the instruments at the VLT is the *Ultraviolet and Visual Echelle Spectrograph* or UVES. It is located at one of the two Nasmyth foci (Nasmyth B) of Unit Telescope 2, Kueyen.

UVES is a high-resolution cross-dispersed echelle spectrograph. It operates at high efficiency from the ultraviolet atmospheric cut-off at 300 nm to 1100 nm in the near infrared as limited by the CCD detectors. The spectrograph's beam can be split up by a dichroic beam splitter into two arms (Blue and Red), which can be either used parallel (in dichroic mode) or separately.

The resolving power $R = \lambda/\Delta\lambda$ when using an 1 arcsecond slit is about 40,000. For the Blue arm the maximal (two-pixel) resolving power is 80,000 while the Red arm can reach an resolving power of 110,000. The Blue arm camera has a 2k by 3k ($15\mu m$) pixel CCD chip, while the Red arm has a two CCD mosaic of a total 4k by 4k pixel with a small gap in between. The wavelength coverage for the blue CCD is from 300 to 500 nm, for the red two CCD mosaic the middle one ranges from 420 to 860 nm and the red one from 680 to 1050 nm.

For very high accuracy radial velocity measurements, an iodine reference cell can be inserted in the beam of light of the pre-slit optics. A schematic overview of the UVES design can be found in figure 4.1 that has been taken from the UVES User Manual to be found on the UVES/VLT documentary web page[1] of ESO.

[1] http://www.eso.org/sci/facilities/paranal/instruments/uves/doc/

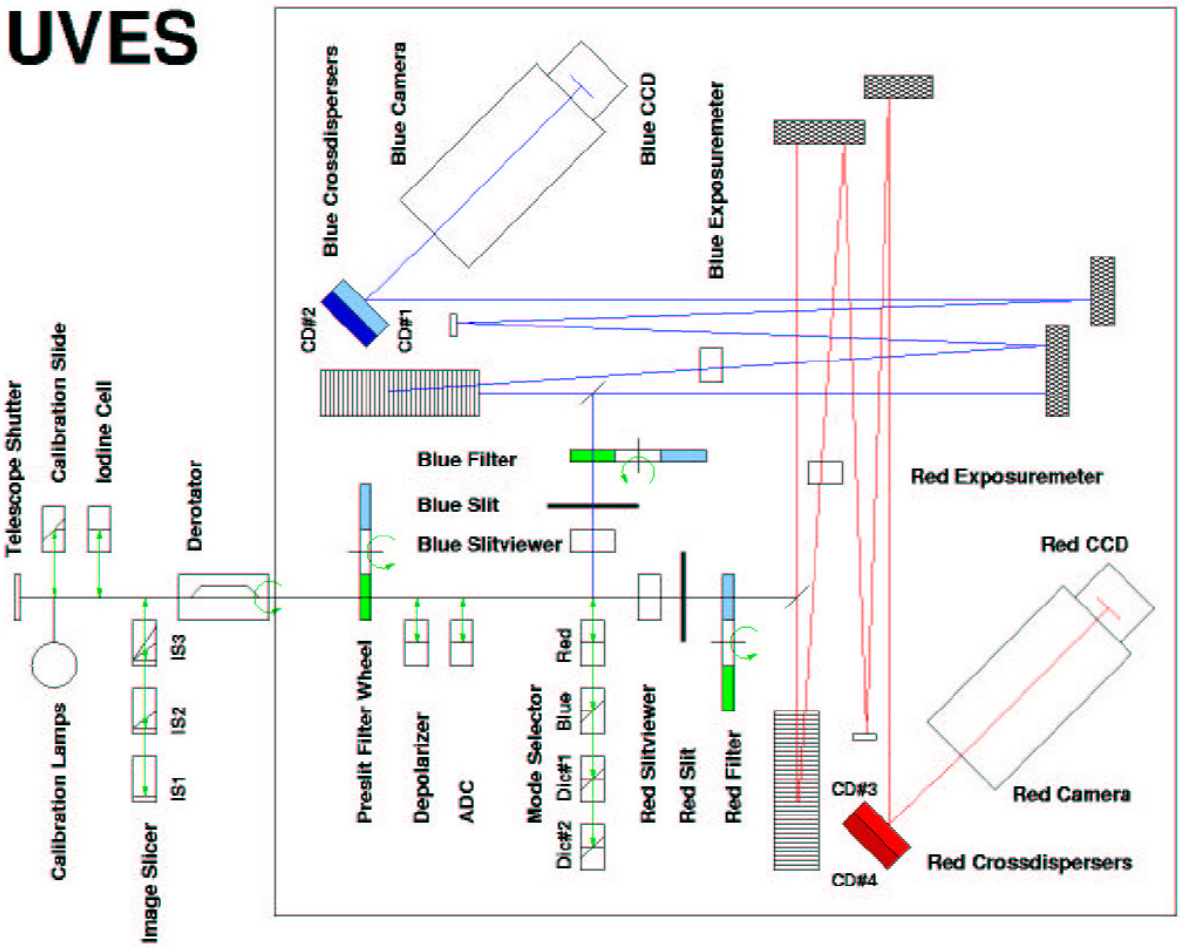

Figure 4.1: Schematic overview of UVES (from the UVES User Manual)

UVES was designed following a double beam white pupil echelle spectrograph layout, which is also used for most of the current high-resolution spectrographs for 8-10 m class telescopes like HRS (Keck) or HDS (Subaru). The wavelength coverage for the Blue arm is 100 nm and for the Red arm either 200 nm or 400 nm, which can be operated simultaneously by using a dichroic beam splitter.

UVES uses steep monolithic mosaic R4 echelle gratings together with dioptric cameras of high-efficiency coatings. The CCDs have optimal quantum efficiency from UV to blue wavelengths for the Blue arm and the 2 CCD mosaic of the Red arm is optimized for the Visual and Near IR, respectively. For mechanical and thermal stability, UVES is mounted at the Nasmyth B focus table inside a thermal enclosure.

The pre-slit optics contain the derotator prism and an iodine cell for excellent wavelength calibration can be inserted in the beam of light as well. For common wavelength calibration, a standard Hollow Cathode ThAr lamp and for flatfielding a Deuterium lamp can be inserted by a 45° calibration mirror here as well.

The high-temperature iodine cell is a glass cylinder of 74 mm diameter with 5 mm Pyrex windows and an optical path of 4 cm. Heating tape strips are evenly distributed on the cell. The iodine cell is maintained at 70 ± 0.3°C with full evaporation reached at 65°C.

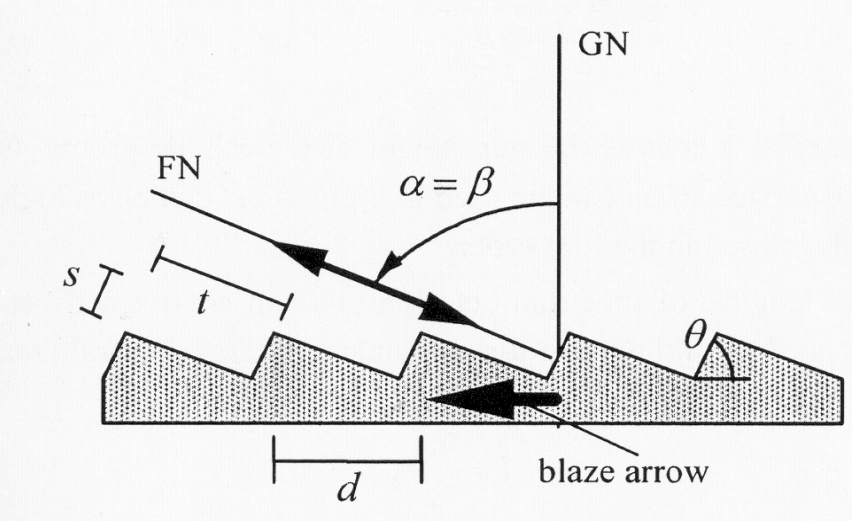

Figure 4.2: Schematic of a blazed echelle grating in Littrow mode with $\alpha \approx \beta \approx \theta_{\text{blaze}}$. GN is the grating normal, FN the facet normal, t the step width, s the step height, d the groove spacing and θ the groove angle (taken from Palmer (2005)).

The R4 echelle is a blazed grating operating at Quasi Littrow Mode (i.e., $\alpha \approx \beta \approx \theta_{\text{blaze}}$) as is illustrated in figure 4.2. For UVES, a small collimator off-plane angle of $0,8°$ separates the incident from the diffracted beam. Therefore, steep gratings with nominal blaze angles of $\theta_{\text{blaze}}^{\text{Blue}} = 76.0°$ for the Blue arm and $\theta_{\text{blaze}}^{\text{Red}} = 75.1°$ for the Red arm are installed in the spectrograph.

The total length of the grating is 84 cm based on a monolithic mosaic of two rulings on a single substrate for the Red arm, which has a stable Point-Spread-Function (PSF) and can be simply mounted. The beam size is about 20 cm. More detailed information on the design and construction of UVES can be found in Dekker et al. (2000). The echelle grating properties of UVES are summarized in table 4.1.

arm	wavelength coverage [nm]	resolving power (maximal)	spacing [grooves/mm]	blaze angle θ_{blaze} [°]	grating length [cm]
Blue	300-500	80,000	31.6	76.0	84
Red	420-1100	110,000	41.6	75.1	84

Table 4.1: Table of properties of the echelle gratings used in the UVES spectrograph.

4.2 Observed targets

The data used in this work has been observed with the UVES/VLT spectrographic telescope of ESO Paranal Observatory (ESO Program ID 073.D-0424(A)). Spectra for all four stars ϵ Indi, α Tau, GJ 86 and the reference star α Pav have been observed within the night in 2004 from November 23 to 24 in local time (Chile) or from November 24 in Universal Time, respectively.

The observatory seeing of that night usually ranged between 0.5 and 0.8 arcseconds with

small episodes of extraordinary good seeing around 0.3 arcseconds. At the end of the night, also higher seeing values of up to about 1 arcsecond have been measured. The seeing almost always remained constant during a single exposure.

target identifier	proper name	coordinates right ascension	coordinates declination
α Pav HD 193924	Peacock	20h 25' 38.858"	-56° 44' 06.32"
ϵ Indi HD 209100		22h 03' 21.657"	-56° 47' 09.51"
α Tau HD 29139	Aldebaran	04h 35' 55.239"	+16° 30' 33.49"
GJ 86 GL 86 HD 13445		02h 10' 25.934"	-50° 49' 25.41"

Table 4.2: Table of the FK5 (equinox 2000) coordinates and names of the target stars for the observations on the night of 2004-11-24.

The coordinates and alternative names of the stellar targets can be found in table 4.2. Only the Red arm of UVES has been used with the chosen setup RED600 stating the central wavelength of 600 nm and a slit width of 0.3 arcseconds aiming at a resolving power of $R \approx 100,000$. The observational setup details are listed in table 4.3.

telescope	instrument	arm	wavelength setup [nm]	resolving power R	iodine cell T [°C]	Program ID (ESO/VLT)
VLT UT2	UVES	Red	600 (500-700)	100,000	≈ 70	073.D-0424(A)

Table 4.3: Table of the chosen observational setup for the UVES spectrograph.

Beside the standard calibration data like bias frames, flatfields, order definition frames and ThAr frames for wavelength calibration, the observations included the typical set of data for a radial velocity analysis based on the iodine cell method. Therefore, a set of flatfields with inserted iodine cell has been observed to gain the instrumentally broadened iodine spectrum.

As iodine reference a Fourier-Transform-Spectrometer (FTS) based super-high-resolution iodine spectrum scan is accessible through the UVES tools web page[2] . With this iodine reference it is possible to determine the instrumental profile, which can then be used to create the stellar template, which is described more detailed in chapter 5.

The observations of the hot B2 IV giant α Pav with and without iodine cell have only been taken for the standard derotator position angle (0°) since this hot giant star was intended to be used alternatively for gaining the iodine spectrum by dividing the iodine

[2]UVES tools web page http://www.eso.org/sci/facilities/paranal/instruments/uves/tools/

based stellar spectrum by its pure form that is showing only very few stellar lines because of the high temperature.

For the three remaining target stars spectra with and without inserted iodine cell have been observed as well. Since observations of different spin-slit alignments are needed for the differential broadening analysis, several exposures have been taken with different rotated derotator position angles.

target name	spectra of position angles PA[°] *without* I_2 cell	spectra of position angles PA[°] *with* I_2 cell
α Pav*	0	0
ϵ Indi	0, 60, 120, 180, 300, 360	0, 60, 120, 180, 300, 360
α Tau	0	0, 60, 120, 180, 240, 300, 360
GJ 86	0	0, 120, 240, 360

Table 4.4: Table of available spectra with and without iodine (I_2) cell usage from the observations (ESO period 73) of the target stars α Pav, ϵ Indi, α Tau and GJ 86 sorted by the available derotator position angle data. * = alternative I_2 reference star.

Additionally, to potentially enhance the S/N ratio several exposures have been taken at the same derotator position angle. The derotator position angle has been changed in steps of 60° as a compromise of the sampling of the the angular range coverage (0-360°) and the available time for the observations.

Therefore, not all combinations with or without iodine (I_2) cell and different derotator position angles have been realized. Particularly, except for ϵ Indi, all other targets have only been observed without iodine cell at the standard position angle. Since these "pure" stellar spectra are the basis for the stellar template needed in the analysis code this is quite important as one can see later in the next chapters 5 and 6. An overview of the available data of different position angles for the four target stars can be found in table 4.4.

target name	spectral class	brightness [mag]	distance [parsec]	temperature [K]	rotation velocity $v \sin i$ [km/s]
α Pav Peacock	B2 IV giant	$B \approx 1.8$ $V \approx 1.9$	56.2	$\approx 18,700$	≈ 35
ϵ Indi	K5 V dwarf	$B \approx 5.75$ $V \approx 4.69$	3.6	$\approx 4,600$	≈ 2
α Tau Aldebaran	K5 III giant	$V \approx 0.85$ $R \approx 0.1$	50.1	$< 4,000$	≈ 8
GJ 86	K1 V dwarf	$B \approx 6.94$ $V \approx 6.17$	10.9	$\approx 5,200$	2.37 ± 0.5

Table 4.5: Table of the attributes of the stellar targets (from SIMBAD database, additional data for GJ 86 from the Extrasolar Planets Encyclopedia http://exoplanet.eu).

The target stars have been selected to be slow rotators and to have a large angular diameter and therefore being nearby stars. While ϵ Indi and GJ 86 are dwarf stars, α Tau is a giant star. α Pav as the alternative iodine reference star is a hot B giant showing only few stellar lines in its spectrum. Attributes of the target stars can be found in table 4.5.

An estimation of the angular diameter of the three target stars can be calculated trigonometrical according to

$$\Phi_R/arcsec = 4,65 \cdot 10^{-3} \frac{R/R_\odot}{r/pc}$$

(see also section 3.2.3) times 2 for the full diameter (=2x radius), with R the stellar radius, $R_\odot$ the solar radius, r the distance and pc=parsec. This can only be a rough estimate except for one of the apparent larger stars α Tau (Aldebaran), where the actual angular diameter has been measured with various techniques like lunar occultations or long-baseline interferometry.

The mean limb darkened apparent diameter of Aldebaran is $\Phi_{\text{Aldebaran}} = 20.58 \pm 0.03$ milliarcsec, see also Richichi & Roccatagliata (2005) for details. The estimated angular diameters of the relevant target stars can be found in table 4.6.

target names	radius R [$R_\odot$]	distance r [parsec]	angular diameter Φ [arcsec]
ϵ Indi	0.76	3.6	0.002
α Tau	44.2	50.1	0.021*
GJ 86	0.86	10.9	0.001

Table 4.6: Table of the radii and angular diameter of the stellar targets calculated by $\Phi_R/arcsec = 4,65 * 10^{-3}(R/R_\odot)/(r/pc)$ times 2 for the full diameter. * The mean actually measured angular diameter of Aldebaran is 20.58±0.03 mas (from Richichi & Roccatagliata 2005).

The CHARM2 catalog of Richichi et al. (2005), a catalog containing more than 8,000 entries of measured stellar angular diameter can be found on the CDS web page[3].

The target objects have not only been chosen due to their large angular diameter (mostly because they are in the solar neighborhood) and relatively slow rotation velocity but they are also showing some peculiarities. While, as already mentioned, Aldebaran is one of the apparently larger stars on the sky with a measured angular diameter of approximately 21 milliarcseconds, ϵ Indi and GJ 86 have companions. The spin-orbit alignment of these systems can lead to insights of the system building theory as mentioned in the introduction if the spin orientation of these stars can be determined.

ϵ Indi is a multiple star system with the main component ϵ Indi A (as used here) and a double star companion ϵ Indi B. The ϵ Indi system with a distance of about 3.6 parsec belongs to the 100 nearest stellar systems known as listed by the RECONS[4] list. The companion double star ϵ Indi B has a separation of about 402 arcseconds to the main

[3]CHARM2 http://cdsarc.u-strasbg.fr/viz-bin/Cat2?cat=J%2FA%2BA%2F431%2F773%2F
[4]RECONS (Research Consortium on Nearby Stars) http://www.recons.org/

component. The B component itself consists of two brown dwarfs Ba (spectral class T1) and Bb (T6), which are separated by less than 2 arcseconds.

The GJ 86 system also consists of multiple objects. Beside the main component A (as used here) there is also a white dwarf companion GJ 86B. Furthermore, an approximately 4 Jupiter mass exoplanet Gl 86b has been detected so far. More details on the GJ 86 (also known as GL 86) system can be found in the Extrasolar Planets Encyclopedia[5].

The three target stars, ϵ Indi, GJ 86 and α Tau have been selected to fulfill the criteria derived in chapter 3.

4.3 Data reduction

The data has been reduced with the REDUCE package of Piskunov and Valenti (Piskunov & Valenti 2002) developed for high-resolution echelle spectrographs. REDUCE is a program package using the *Interactive Data Language* (IDL) analysis and visualization system of ITT Visual Information Solutions.

The REDUCE package uses automatical routines whenever possible to produce reproducible results. REDUCE was designed to "optimally" extract the spectrum by constructing a relative illumination profile perpendicular to the echelle dispersion without any specific assumptions. For slowly varying spatial profiles artifacts can be handled in a convenient way.

The REDUCE script supports several high-resolution spectrographs like UVES and can also be expanded for other echelle spectrographs with *fits* file output. The output spectra are saved in a special format called *ech* files, which is based on the fits format but no common fits reader is able to handle them, so the integrated ech reader must be used. The spectral data including the headers and diffraction order information as well as the wavelengths are gathered in an IDL structure for easier use.

For the first steps of the reduction the bunch of bias and flatfield frames are co-added into two groups. A pixel-to-pixel median filter comparison is used to monitor the read noise and to identify outliers like cosmic ray impacts statistically. Incorporating bad pixels, the two revised group images are then combined to a mean bias (or flatfield) frame.

After that, the mapping of the (diffraction) order location and curvature on the images is done empirically in an automatical way. Scanning the order definition image (rotated in a way that the orders are arranged roughly horizontal) line-by-line the contrast based algorithm performs a clustering analysis and merges clusters to final orders.

Manual interaction is needed sometimes in the end for special cases like crossing fringes. The order definition procedure is robust enough to alternatively handle the science image instead of an order definition frame or flatfield.

With the known order locations the mean flatfield's spatial and spectral order profile is decomposed by an oversampled model of the spatial profile and the order shape function or blaze. The flatfield based blaze is saved to roughly normalize the science spectrum later. Assuming the model to be constant over a certain region, pixel defects can be handled.

[5]GJ 86 at Extrasolar Planets Encyclopedia http://exoplanet.eu/star.php?st=Gl%2086

A scattered light estimation including the background based on the inter-order troughs is included in the routines, which is then subtracted from the image. Bad rows are handled with a mask file matching the spectrographs CCD defects.

The noise level is measured empirically from the standard deviation of the observed order minus the reconstructed model. Finally the flatfield is divided by the reconstructed model and normalized to obtain the pixel-to-pixel variations.

The extraction of the science spectra and wavelength calibration frames is done accordingly after subtraction of the mean bias and division by the normalized flatfield. Then, the scattered light is estimated and subtracted from the remaining image using the already mapped diffraction order locations. In an oversampled pixel space the spectral and spatial order profile is decomposed resulting in a reconstructed model, which is also used to find and correct bad pixels.

Using noise model based weights, each column of an order is fitted with the appropriate illumination profile. Finally, the extracted relative intensity of the spectral orders is divided by the order shape function (or blaze from the normalization process of the flatfield) to flatten the continuum. A detailed description of the reduction process can be found in Piskunov & Valenti (2002). The iodine flatfields and the iodine based stellar spectra are handled the same way as the other science spectra.

The extracted wavelength calibration spectra (ThAr in case of UVES) can then be compared to an included ThAr spectrum in an interactive application by identifying (wavelength) and fitting of lines (with line profiles such as a Gaussian) manually by the user. This is done order per order.

When a certain number (typically more than 6) of spectral ThAr lines is identified within an order a polynomial wavelength fit can be applied, with additional line fitting done automatically afterwards. Finishing more than three orders distributed over the whole image, a 2D (meaning pixel space and order number) wavelength solution is calculated by the REDUCE package, which enables automatical line fitting over all orders with the user left for the fine tuning of individual orders.

Also, already known 2D wavelength solutions of previous observations can be used to construct new wavelength solutions by a simple line/row alignment and the automatical line fitting process followed by the polynomial calculated wavelength solution. In the end, the final wavelength solution can be included in the extracted spectra.

Chapter 5

The modeling code

5.1 Radial velocity codes

Most of the known extrasolar planets have been found with the radial velocity method. The host star and its companion rotate around their center of mass. Therefore, when looking at the host star (the planets are too dark and the contrast to their host star is too strong for the planets in close orbits to bee seen directly) its velocity vector changes periodically. The radial component along the line-of-sight of the observer of this oscillating velocity causes a periodically Doppler shift of the spectrum of the star, which can be measured.

With classical spectroscopy of the star, the accuracy of the wavelength shift determination (with typically errors of the radial velocity of $\approx$ 1 km/s) is not good enough to detect Jupiter like or lower mass extrasolar planets. Therefore, high-resolution spectrographs have been combined with special methods for a much more accurate wavelength calibration.

Common techniques are using a gas reference absorption cell or to observe spectra of wavelength calibration lambs (like Thorium-Argon (ThAr) lambs) simultaneously with the star. See also Marcy & Butler (1992) for the advantages of using an iodine cell.

With the inserted reference gas absorption cell (in the visual regime iodine (I_2) is used for UVES for example) in the optical path, the forest of the reference gas molecular lines are superimposed to the observed spectrum of the target star. The reference gas molecular lines deliver a high accuracy wavelength calibration, which provides a much better relative wavelength shift accuracy.

Gas absorption cells can also be used to determine the instrumental profile (IP, i.e., the line-spread-function as the one-dimensional analog to the two-dimensional point-spread-function (PSF)). Doing so the observed molecular gas lines are modeled by a super-high-resolution reference spectrum of that gas and an appropriate instrumental profile model.

Using a super-high-resolution quasi intrinsic gas cell spectrum observed by a Fourier-Transform-Spectrometer (FTS), this instrumental profile determination technique has been described in Valenti et al. (1995) on example of an I_2 cell. An observed stellar spectrum with inserted iodine cell and the corresponding FTS iodine spectral part can be found in figure 5.1.

The known intrinsic iodine FTS spectrum is convolved with a parameterized IP to compare

it with the observed spectrum. The parameterized instrumental profile is optimized to match the model spectrum with the observed spectrum within the noise limits. From the shape of the molecular iodine lines in the observed stellar spectrum the modeled IP can handle (environmental) changes in the spectrometer optics or illumination.

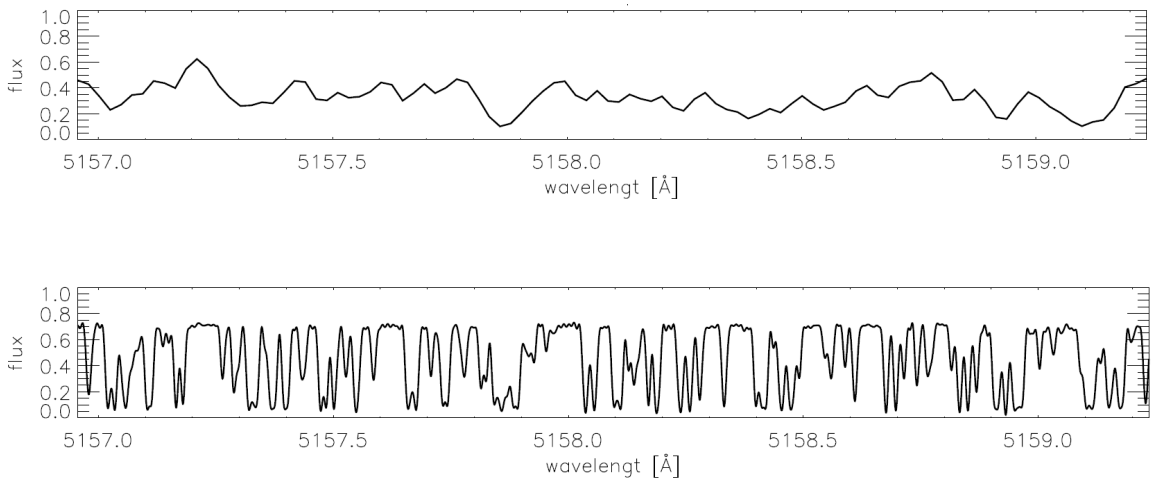

Figure 5.1: TOP: Observed spectrum part (a chunk of 2 Å) of a star with inserted iodine cell. BOTTOM: Iodine absorption cell reference spectrum from a Fourier-Transform-Spectrograph.

Combining both advantages of the gas absorption cell like the superior wavelength calibration and the instrumental profile modeling, much lower radial velocity errors can be achieved in combination with a high-resolution echelle spectrograph. Such a radial velocity (RV) code has been described and applied by Butler et al. (1996) achieving a radial velocity scatter of 3 m/s at a resolving power of $R \approx 62,000$.

To also account for a varying instrumental profile over the whole CCD chip, the spectral (diffraction) orders are divided into small parts ("chunks"), which are independently used to determine the localized IP. The size of these spectrum parts is chosen to show enough structure for the modeling (i.e., being large enough) on the one hand and to account for changes in the IP (i.e., being small enough) on the other hand. A useful size, according to Valenti et al. (1995); Butler et al. (1996), is a chunk width of approximately 2 Å.

For this work a similar radial velocity code has been friendly provided by J. Bean. It uses the same methods as described by Valenti et al. (1995) and Butler et al. (1996) within a collection of IDL based routines. A short description of the RV code can be found in Bean et al. (2007). Since this work aims for measuring broadening deviations between spectra of different spin-slit alignments, the radial velocity code has been expanded with an extra broadening mechanism.

5.2 Instrumental profile modeling

The radial velocity code used for this work is divided into two main parts. In the first part the stellar template is created using the instrumental profiles from an observed flatfield

with inserted iodine cell. Further details of the template creation can be found in the next section.

In the second part observed stellar spectra with inserted iodine cell are compared to a model spectrum based on the shifted stellar template, the FTS iodine spectrum as the intrinsic gas reference spectrum and an IP model. Details on the radial velocity part can be found in section 5.4.

For both parts, the instrumental profile modeling is important. Following the instrumental profile determination by Valenti et al. (1995), the code used here is also based on a parameterized model of the IP. The code uses the MPFIT non-linear lest squares fitting routines of Markwardt (2009) for IDL to find that instrumental profile, which best reproduces the observed spectrum when convolved with the template or reference spectrum.

The MPFIT routines are based on the Levenberg-Marquardt algorithm as presented in Moré (1978) and Moré & Wright (1993). The original MINPACK-1 package of Jorge Moré is available from netlib http://www.netlib.org/minpack. MPFIT is a conversion of the non-linear least squares fitting program MINPACK-1 to IDL. MPFIT inherits the robustness of the original FORTRAN version of MINPACK-1, but is optimized for performance and convenience in IDL.

Several constraints can be applied to model parameters, including fixed constraints, simple bounding constraints, and "tying" the value to another parameter. Several data-weighting methods are allowed, and the parameter covariance matrix is computed. Extensive diagnostic capabilities are available during the fit, via a call-back subroutine, and after the fit is complete. The package has been translated to C and Python as well. The full IDL and C packages can be found at http://purl.com/net/mpfit.

This algorithm is more desirable than IDL's own CURVEFIT routine because it is generally more stable and less likely to crash than the brute-force approach taken by CURVEFIT, which is based upon Numerical Recipes (Press et al. 1992). Also model parameters can be "frozen" (that is, held constant during the fitting process) or used with simple boundary constraints. The radial velocity code used here makes use of these advantages by a hierarchical fitting process starting with a very simple IP model to constrain the wavelength calibration before using the full IP model (including the radial velocity shift in the second part).

The instrumental profile model is optimized to use as few parameters as needed. Judging from a typical echelle spectrograph, the IP core is modeled by a central Gaussian with the height calculated from the width with $height = 1/(width\sqrt{2\pi})$, so using only the width as parameter. In the first fitting step, this simple model IP consisting only of the central Gaussian is used to gain the wavelength calibration (polynomial fit) parameters.

The model convolution and IP construction routines are using an oversampled pixel space (with the user to choose the oversampling factor, which is usually in the order of 4 to 6) for a higher mathematical accuracy. After the model building calculations, the model parameters are optimized by the comparison of the model and the observed spectrum using the MPFIT non-linear least squares fitting routines within the original pixel scale of the observations.

Furthermore, the spectrum of interest is divided into small parts "chunks" of approximately 2 Å width. For UVES, aiming at a resolving power of $R \approx 100,000$, this corresponds to

roughly 100 pixel. These chunks are analyzed independently from each other order by order.

After the initial wavelength fit the instrumental profile model is expanded with a series of satellite Gaussians of fixed position and width (or relative to the central Gaussian's width as chosen by the user) with the satellite Gaussian's height the only parameter left to be fitted. The satellites are used to model asymmetries and other deviations to the wings of the core IP consisting of the central Gaussian. The components of the IP model are illustrated in figure 5.2.

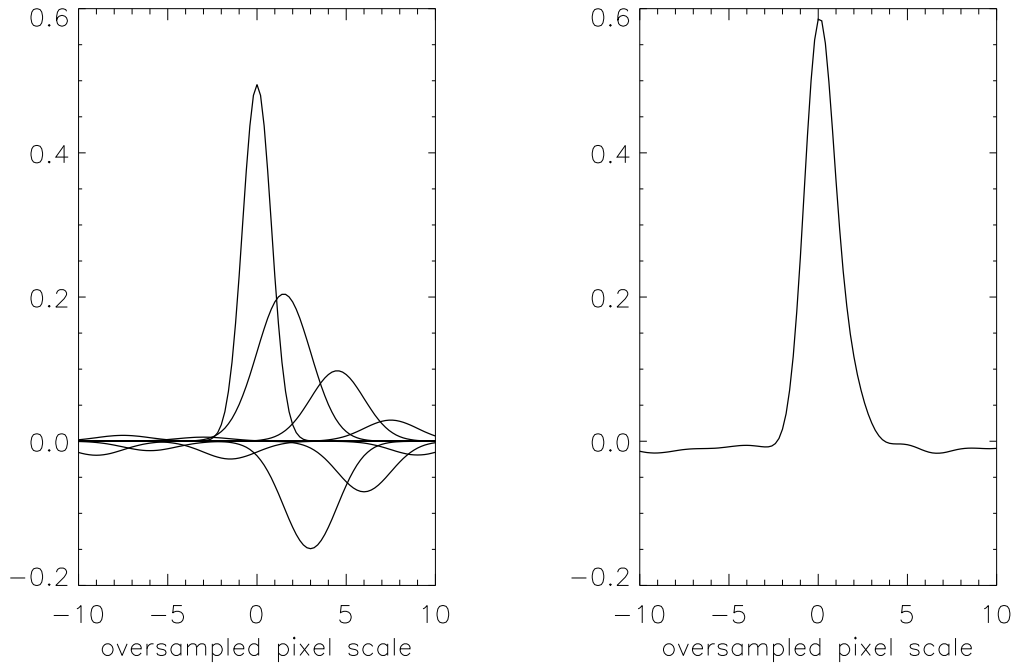

Figure 5.2: LEFT: A model IP consisting of the central Gaussian with all satellite Gaussians drawn separately. RIGHT: The summed IP model for a local spectrum part ("chunk").

With the full IP model including the satellite Gaussians the modeled spectrum is recalculated using the resulting parameters from the initial step as input. Since the chunks are handled independently but belonging to the same spectral order, the wavelength scale is unified over the whole order afterwards. This unified wavelength scale is then fixed for the next step, the fitting of the radial velocity shift.

5.3 Stellar template creation

For the observed gas absorption cell spectrum the often used possibility to use an Fourier-Transform-Spectrograph (FTS) for gaining an intrinsic like super-high-resolution spectrum performs well. The situation is different for stellar spectra. FTS can not be used on stellar sources to create a stellar template spectrum because they are too faint except for some very bright nearby giant stars. Therefore, the stellar template must be created from an observed echelle spectrum of the star (without inserted iodine cell), which is already instrumentally broadened.

The stellar template creation from an already instrumentally broadened spectrum is not easy as it requires a deconvolution of the instrumental profile. The code uses a modified Jansson technique for the deconvolution as mentioned in Bean et al. (2007) and in the deconvolution chapter of Gilliland et al. (1992) as described on example of the Goddard High-Resolution Spectrograph.

Numerical deconvolution is a hard business mostly affected by instabilities during the calculations. The ideal case would be to know the exact IP of the actually observed stellar spectrum but this is not possible since it depends on varying environmental and illumination conditions such as seeing.

Alternatively, the IP from a contemporary observed iodine (flatfield) spectrum, determined using the FTS iodine spectrum as the intrinsic I_2 template, is assumed to also match for the stellar spectrum.

Theoretically calculated stellar super-high-resolution spectra are unqualified here because the stellar parameters and especially the elemental abundances and their transition properties are only poorly known if at all.

So the first part of the analysis procedure of the radial velocity code determines the instrumental profile of an observed iodine (flatfield) spectrum. The FTS iodine spectrum is used as the intrinsic iodine template, which is convoluted with an IP model as described in the preceding section.

After the IP model parameter optimization process is finished, the determined instrumental profiles (for each chunk) is deconvolved from an observed stellar spectrum. The resulting stellar template spectrum including the barycentric correction is the base for the following relative radial velocity analysis.

5.4 Radial velocity analysis

The final step in the original radial velocity code is the radial velocity determination. This is performed relative to the created stellar template spectrum. As described in the preceding sections, a model of the observed stellar spectrum with inserted iodine cell is processed. This model is based on the stellar template spectrum multiplied with the intrinsic iodine (FTS) spectrum and convolved with a instrumental profile model.

To determine the radial velocity shift, a Doppler wavelength shift factor is initially applied to the stellar template spectrum.

$$\lambda_{\text{shifted}} = \lambda \left(1 + \frac{v}{c}\right)$$

The Doppler wavelength shift factor depends only on the radial velocity v and on the speed of light c. The radial velocity v enters as an additional parameter into the fitting process. The shift direction depends on the algebraic sign of the radial velocity. A schematic overview of the whole model process can be found in figure 5.3.

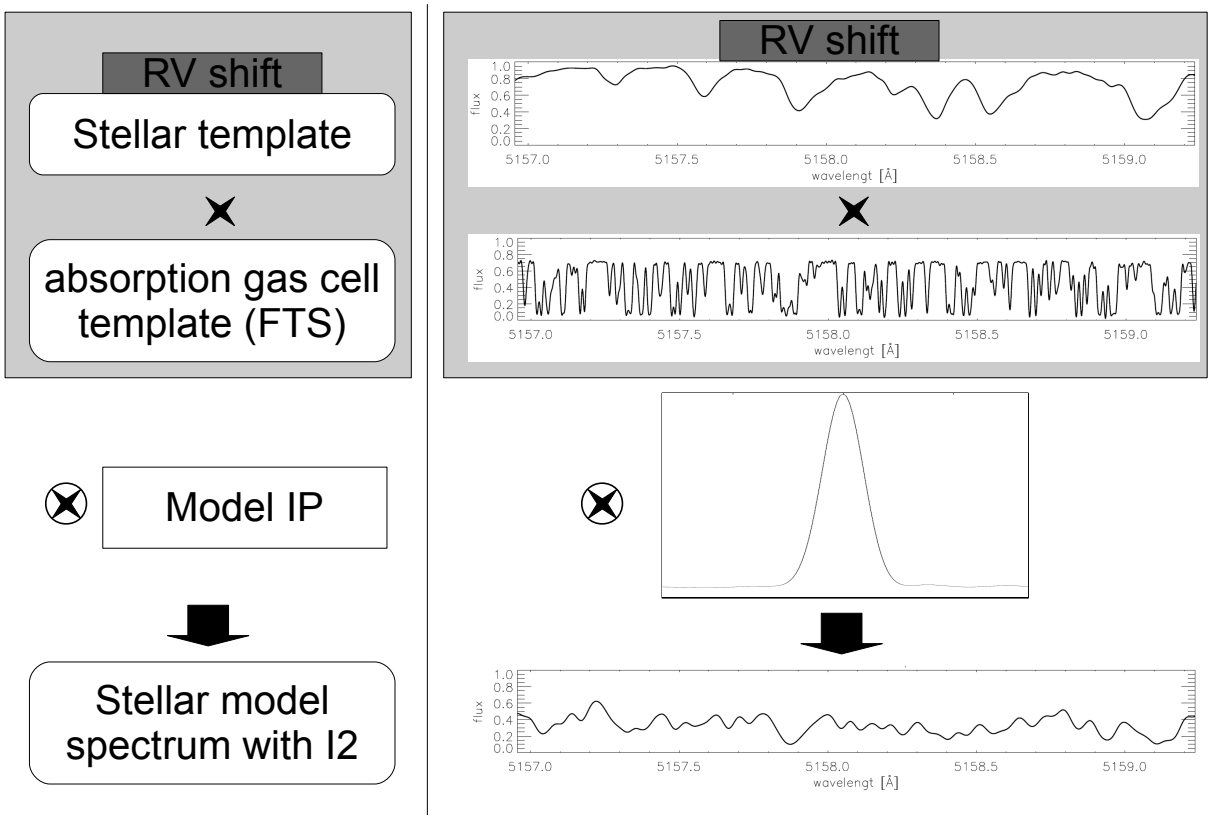

Figure 5.3: Schematic overview of the modeling process on the left with example images on the right. From top to bottom the model starts with the RV shifted stellar template multiplied by the FTS iodine, which is then convolved with the instrumental profile (IP). The resulting IP broadened model spectrum with I_2 represents the observed stellar spectrum with inserted iodine cell.

The radial velocity shift is calculated for all chunks independently and stored. Either an histogram analysis or a weighted average is used to calculate the mean value of the whole observed spectrum. Using a weighted average, all spectral parts (chunks) are taken into account. Especially the edges with poor S/N values count less than the middle parts with high S/N of a spectral order, which leads to an adequate mean value of the relative radial velocity shift.

Analyzing a time series of observations with such a code then reveals the Doppler shift oscillations of a star with a companion except for the "on top view" case with the orbital motion being perpendicular to the line of sight. For that special case, no oscillating radial velocity shift can be observed since this velocity component remains unaffected by the planetary orbit.

5.5 Differential broadening modeling

The spectral broadening mechanism described in chapter 2 originates in the rotation of the star and its angular diameter in combination with a spectrograph. Therefore, only the

stellar spectrum is affected but not those of the gas absorption cell inserted in the optical path of the spectrographic telescope.

The spectral broadening is a result of the combined wavelength shift $\Delta\lambda_{\mathrm{tot}} = \Delta\lambda_{\mathrm{rot}} + \Delta\lambda_{\Phi}$ integrated over the stellar disc. This broadening effect only changes the stellar template in the code similarly to the radial velocity shift applied to it. But in contrast to a simple radial velocity shift the handling of the broadening is much more complicated.

The stellar template is created from an observed stellar spectrum, which is deconvolved with an appropriate instrumental profile as described in the section 5.3. But still, this stellar template also is a result of all other effects like stellar rotation, the geometrical effect of the elongated stellar disc and the seeing for example. In contrast to a fully intrinsic line spectrum this stellar template spectrum is defined by its origin (the stellar -) and observational conditions.

So it is only possible to account for broadening deviations relative to the already broadened stellar template spectrum. As mentioned in chapter 2, the broadening deviations arise from observations of the same star with different spin-slit alignments.

While the radial velocity shift can easily be applied in both direction (by the algebraic sign of the velocity shift) as a Doppler shift factor to the wavelength scale, the situation is different for the modeling of the broadening. Spectral broadening, as also applied for the instrumental and observational conditions described by the instrumental profile, is mathematically implemented as a convolution between a broadening profile (BP) of a certain width ω and a template spectrum.

$$template_{\mathrm{stellar}}^{\mathrm{broadened}} = template_{\mathrm{stellar}} \otimes BP(\omega)$$

Such a broadening profile (mathematically a distribution function) is limited to either make the template spectrum broader or to reproduce the template spectrum, which is then still broadened as mentioned above. It is not possible to make the model spectrum less broadened than the template with this method.

The given situation of an already broadened stellar template spectrum therefore results in two important limitations of the method. First, only (positive) broadening deviations can be measured, which are very small as well as the corresponding broadening profile. Second, the used stellar template should be the weakest broadened one (i.e., that of the "right" spin-slit alignment, which is a priori unknown).

The weakest broadened stellar template is initially unknown, so the ability to choose from pure stellar spectra without inserted gas absorption cell of different spin-slit alignments is crucial. Then it is possible to create and use stellar template spectra from all different spin-slit alignments. A finer covering of different spin-slit alignments enhances the possibility to come close to the absolute broadening minimum.

Processing all template spectra one after another, the extra (positive) broadening of the observed stellar spectra with inserted gas absorption cell of other spin-slit alignments can be modeled best with the weakest broadened stellar template spectrum. When not using the weakest broadened template, some of the measured broadening deviations will be capped to the lower limit, which is zero extra broadening although they are less broadened in reality.

Since the differential broadening profile (BP) is very small regarding the small broadening deviations caused by the combined wavelength shift deviations of different spin-slit alignments, a pixel scale with much higher oversampling factor is needed for the numerical convolution process in the code.

A typical circular broadening profile

$$BP \propto \sqrt{1 - \left(\frac{\Delta\lambda}{\Delta\lambda_{\max}}\right)^2}$$

with a certain width (corresponding to the maximum combined wavelength shift) as the only free parameter has been used here in the code to model the broadening deviations. An example of the broadening profile model can be found in figure 5.4.

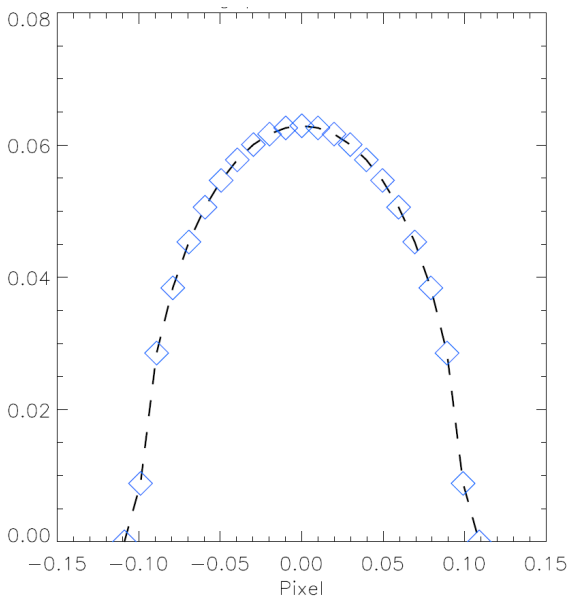

Figure 5.4: Example of a circular broadening profile of 0.1 pixel width with the actually sampled points marked by diamonds on a pixel scale using an oversampling factor of 100.

This broadening profile is sampled in the used (oversampled) pixel space of the code. Therefore, the oversampling factor must be high enough to distinguish the broadening profile of a certain width from the Delta function representing no extra broadening.

An example of a broadening profile with a width of 0.1 pixel using an oversampling factor of 100 can be found in figure 5.4. Oversampling factors as high as 100 and more (for the radial velocity measurement a sufficient oversampling factor ranges from 4 to 6) translate in a much higher computing time.

The differential broadening measurement is implemented in the model with the additional broadening profile to be convolved with the stellar template spectrum before being multiplied with the iodine template spectrum and being convolved with the instrumental profile. This is the final modeling step after the determination of the wavelength scale and the radial velocity shift steps.

The radial velocity shift is held constant during the calculations of the differential broadening in the final step. A schematic overview of the full model process can be found in figure 5.5.

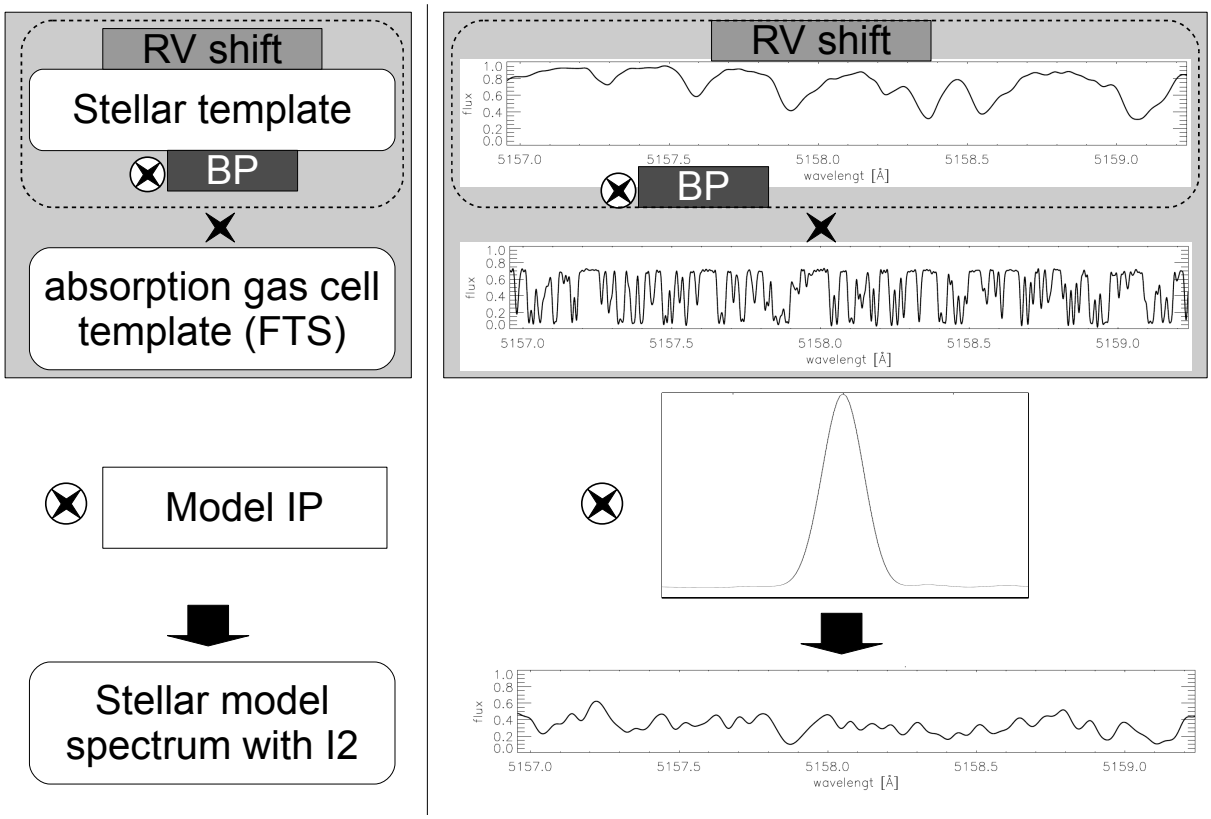

Figure 5.5: Schematic overview of the full model processing on the left with example images on the right. From top to bottom the modeling starts with the RV shifted stellar template convolved with the differential broadening profile (BP) depending on the spin-slit alignment. Then this is multiplied by the FTS iodine, which is then convolved with the instrumental profile (IP). The resulting IP broadened model spectrum with I_2 represents the observed stellar spectrum with iodine of different spin-orbit alignments.

Afterwards, the measured broadening deviations (the widths of the applied broadening profiles) of each spectrum part (chunk) can be averaged to find a mean value for the whole spectrum.

The sinusoidal like progression of the measured broadening deviations with the spin-slit alignments then reveals the position angle of the star. Maximal broadening is reached when the projected rotation axis of the star is coaligned with the spin axis being perpendicular to the dispersion direction of the spectrograph.

Chapter 6

Simulations

6.1 Artificial broadening

A good way to test a program is to apply it to data which properties are already known from the user so the expected result is clear. This data can either be real observed data with approved properties or more likely simulated data.

When simulating data the simulation should be close to the reality so using a spectrum from a real observation as base for simulations gives a good estimate of what the used program is capable of. Or, to begin with, if the program basically works as it is designed for.

Since the expected differential broadening effects for the target stars used in this work are very small, such simulations give us the freedom to use much higher values to test the program and then continue with more realistic values.

Here, the artificially broadened spectra used for the simulations are based on a reverse engineering process of the analysis code. The broadening code as described in chapter 5 rebuilds an observed spectrum by the stellar template spectrum (with the instrumental profile being removed), the intrinsic iodine spectrum (here a FTS spectrum) and a model of the instrumental profile. The differential broadening only affects the stellar template so this is the key for this simulations.

All simulations in this chapter are based on an artificially broadened stellar template of the same spectral order (of ϵ Indi around 5600 Å). The calculations are using an oversampling factor of 200 corresponding to a subpixel sampling of 0.005 real pixel. This is also the minimum value for the numerical broadening profile to be different from the delta function (i.e., to consist of more than one value greater than zero).

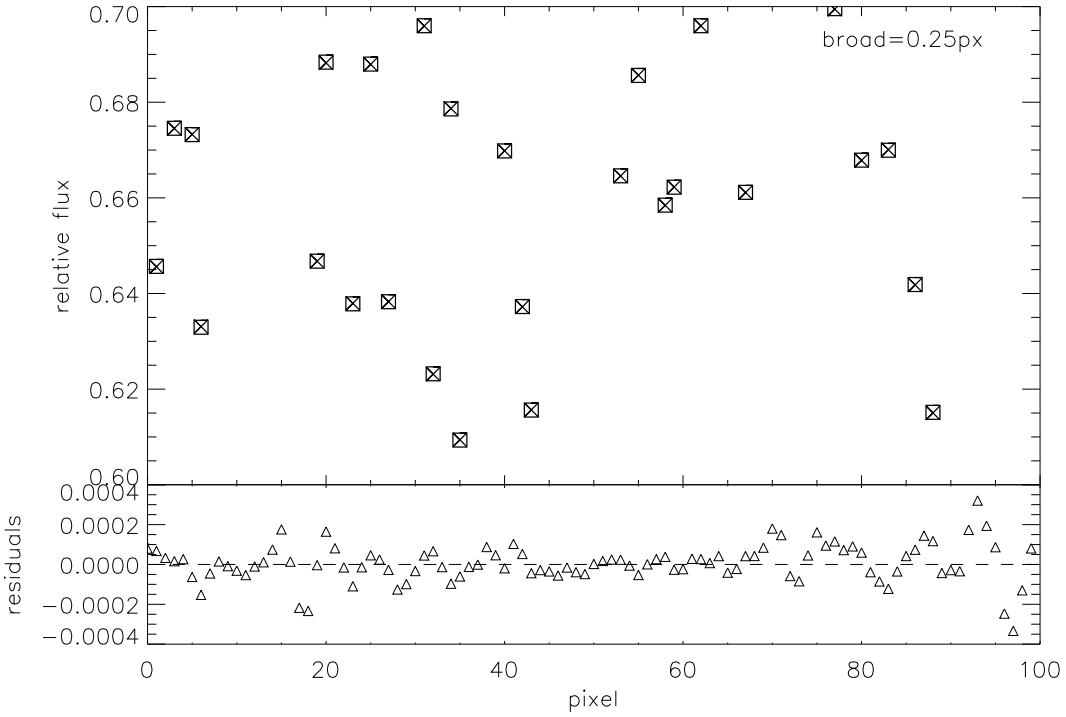

Figure 6.1: This figure shows the simulation of an artificially broadened spectrum (broadening=0.25px; X symbol) compared to its template (squares). Only a small spectrum part (approximately 2 Å) corresponding to a chunk with 100 pixels is shown and the y-axis range is reduced to a small part as well. Almost no difference can be noticed with the naked eye. Therefore the residuals between both spectra are plotted beneath.

The broadening profile used to artificially broaden the template is the same as used for the analysis, a simple one parameter rotation profile. Four different broadening values (broadening= 0.25, 0.10, 0.05 and 0.01 pixel) have been used for the simulations. After the convolution with the differential broadening profile the template spectrum is multiplied with the iodine spectrum and then convolved with an IP consisting of a single Gaussian of approximately the same width as the real one for the UVES data used here.

Finally, the simulated and now artificially broadened spectrum is reduced to its original pixel scale. A spectrum chunk of 100 pixels (about 2 Å wide) is shown in figure 6.1. The simulated spectrum (broadened by 0.25px, using X symbols) is overplotted with the original template spectrum (squares). For a better comparison the y range is zoomed in to a smaller region but still the naked eye can hardly see any difference.

Therefore, the residuals from the difference of both spectra are shown beneath. Judging from the standard deviation of the residuals, a S/N value of more than 9,000 (one sigma) is needed to detect the relatively large broadening of 0.25 px or approximately 270 m/s (for a pixel width of 0.02 Å for UVES at $R \approx 100,000$). For a broadening of 0.10 px (or $\approx$ 110 m/s) the needed one-sigma S/N would be even larger than 50,000.

6.2 Broadening code tests

To test the ability of the broadening code to measure broadening deviations between differently broadened spectra by the geometrical effect for artificially broadened spectra have been prepared in the way as described in the previous section.

Especially no artificial noise has been applied to the test spectra to enable an uninfluenced test of the broadening code's ability to measure the broadening deviation against the pure template spectrum. The spectral order (at about 5600 Å) will be analyzed by the broadening code for each chunk (of 100 pixel each) independently for a total of 36 chunks.

Lacking enough padding space for strong radial velocity shifts and to avoid border effects of the numerical convolution, the first and the last two chunks are skipped by the code. The broadening code first determines the "classical" RV parameters including the radial velocity shift, wavelength scale and instrumental profile (IP). Then for the last step the wavelength and radial velocity shift are fixed to the results from the previous steps. The IP and the now enabled broadening profile is modeled by the broadening code until the best conformity of the model spectrum to the observed (here the artificially prepared) spectrum part is reached.

While the calculations needed to create the model spectrum are preformed in an oversampled pixel space (to provide a well sampled broadening profile and IP) with an oversampling factor of 200, the fitting process is only based on the real pixel space determined by the "observed" spectrum. Caused by the huge oversampling factor regarding the very small broadening deviations, the processing time is drastically increased compared to the original RV code using an oversampling factor of only four to six. But the MPFIT package used to find the best fit makes use of multiple CPU cores automatically if available.

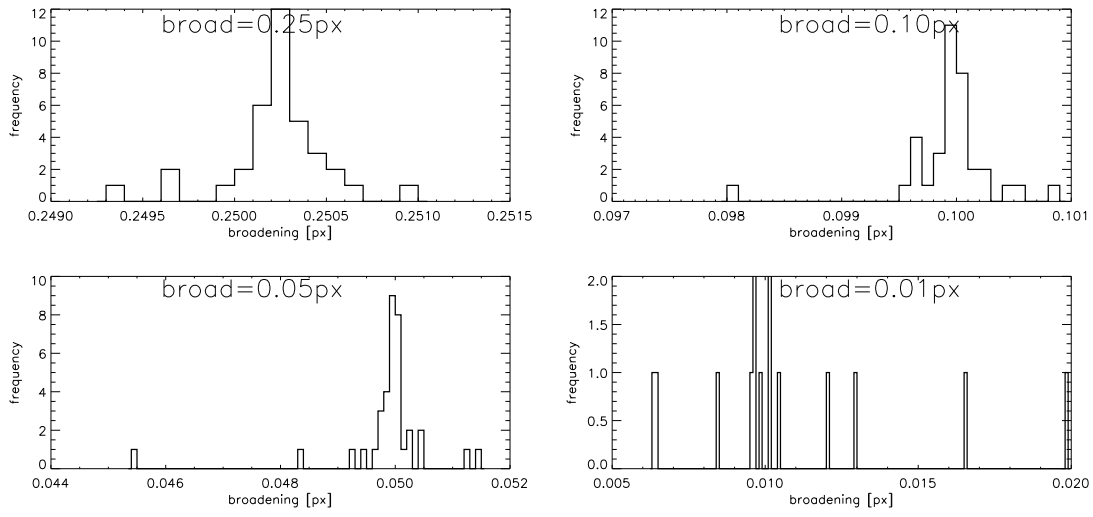

Figure 6.2: These four histograms show the broadening results of an artificially broadened (broadening= 0.25, 0.10, 0.05 and 0.01 pixel) spectral order (around 5600 Å.) when used as input to the broadening code as described in chapter 5 without noise. The number of valid "cleaned" chunks decreases with declined broadening while the input broadening can still be reproduced.

The resulting broadening parameter for each chunk can finally be analyzed. Except for the order edges as described above further selection criteria have been applied to the results. Determined broadening values of less than 0.005 px that are congruent with zero or the lower limit and those values near the upper limit of 0.5 px have been removed as well as the values being equal to the broadening parameter starting value (of 0.3 px) leaving "cleaned" differential broadening values.

The histogram of the remaining determined "cleaned" broadening values (in pixels) of each remaining chunk can be found in figure 6.2. The results have been calculated for four different artificially broadened spectra (broadening= 0.25, 0.10, 0.05 and 0.01 px) including no artificial noise. The median broadening deviation values and the standard deviation from the histograms can be found in table 6.1.

Artificial broadening [pixel]	Artificial broadening [m/s]	Determined median broadening [pixel]	Standard deviation [px]
0.25	≈ 270	0.2502	0.0002
0.10	≈ 110	0.0999	0.0004
0.05	≈ 54	0.0499	0.0009
0.01	≈ 11	0.0101	0.0036

Table 6.1: Table with the median and standard deviation of the "cleaned" broadening deviation values determined by the broadening code for four different artificially broadened spectra (one spectral order at 5600 Å) without noise.

As one can clearly see the broadening code reproduces the artificial broadening well. Even for the smallest broadening of 0.01 px, which is only twice as large as the broadening profile accuracy of 0.005 px (oversampling factor of 200), the broadening code gives good results. Looking at the standard deviation of the results it is rising with the broadening decline.

Also, the number of remaining chunks after "cleaning" falls with the broadening decline leaving less valid chunks to calculate the median, which reduces the accuracy that can be achieved by the lower number of total valid results (or chunks). Still for the special unrealistic situation without noise the accuracy is better than the oversampling accuracy of 0.05 pixel.

6.3 Simulations with noise

After having proven the capability of the broadening code of determining broadening deviations in general, a more realistic approach is needed including artificial noise. Therefore, the same approach as used in the previous section has been used but the artificially broadened spectrum order has been expanded with randomized Gaussian noise of a certain Signal-to-Noise (S/N) level.

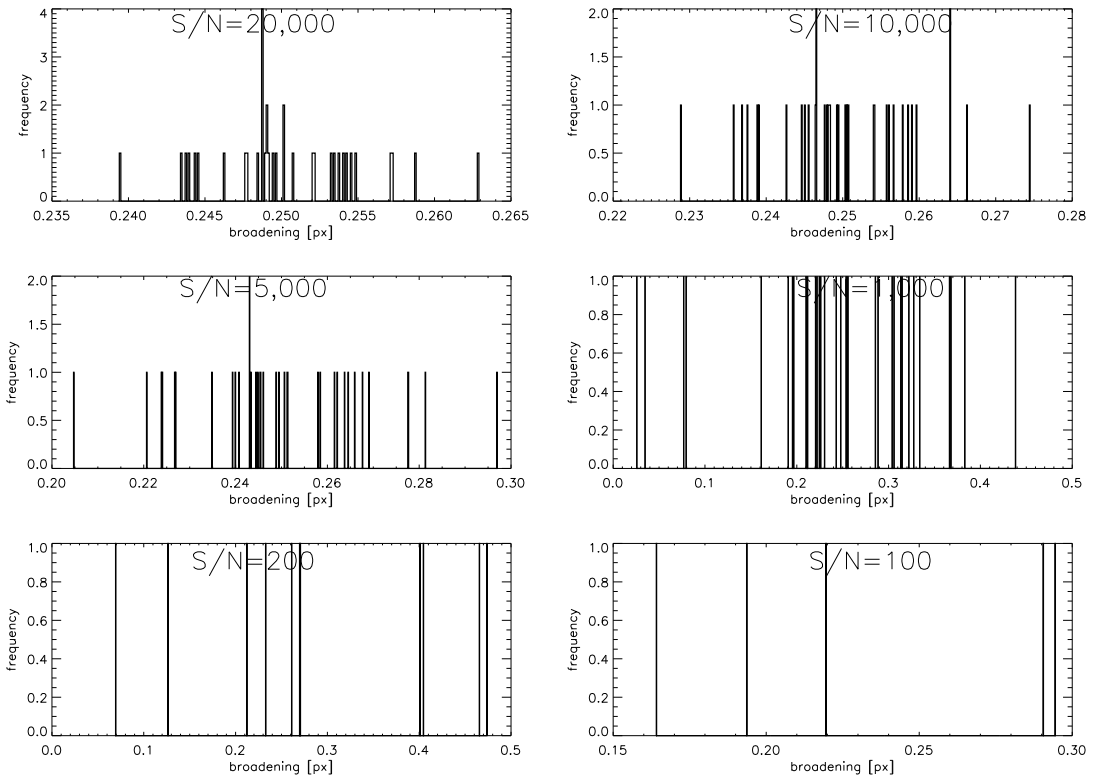

Figure 6.3: Six cleared histograms from different noise levels showing the broadening results of an artificially broadened (broadening=0.25 pixel) spectral order (around 5600 Å) when used as input to the broadening code.

The six chosen noise levels start with a S/N value of 100 and 200, which the real observed spectra range in between, followed by much higher values like 1,000, 5,0000, 10,000 and 20,000 to basically test the ability of the broadening code to reveal the broadening deviations.

Artificial broadening [pixel]	Noise level S/N	Determined median broadening [pixel]	Standard deviation [px]
0.25	20,000	0.249	0.005
	10,000	0.249	0.009
	5,000	0.25	0.02
	1,000	0.25	0.10
	200	0.27	0.13
	100	0.22	0.06

Table 6.2: Table with the median and standard deviation of the "cleaned" broadening deviation values determined by the broadening code for a broadening of 0.25 px and six different noise levels.

As before, histograms of "cleaned" broadening results as described in the previous section are presented but now including different noise levels.

The selected noise levels have been applied to the four different artificially broadened spectra starting with a broadening of 0.25 px. The histogram for all six noise levels can be

found in figure 6.3. The resulting median value and the standard deviation can be found in table 6.2. For the noise levels from 20,000 to 5,000 the number of valid chunks remain high and the broadening results are well reproduced.

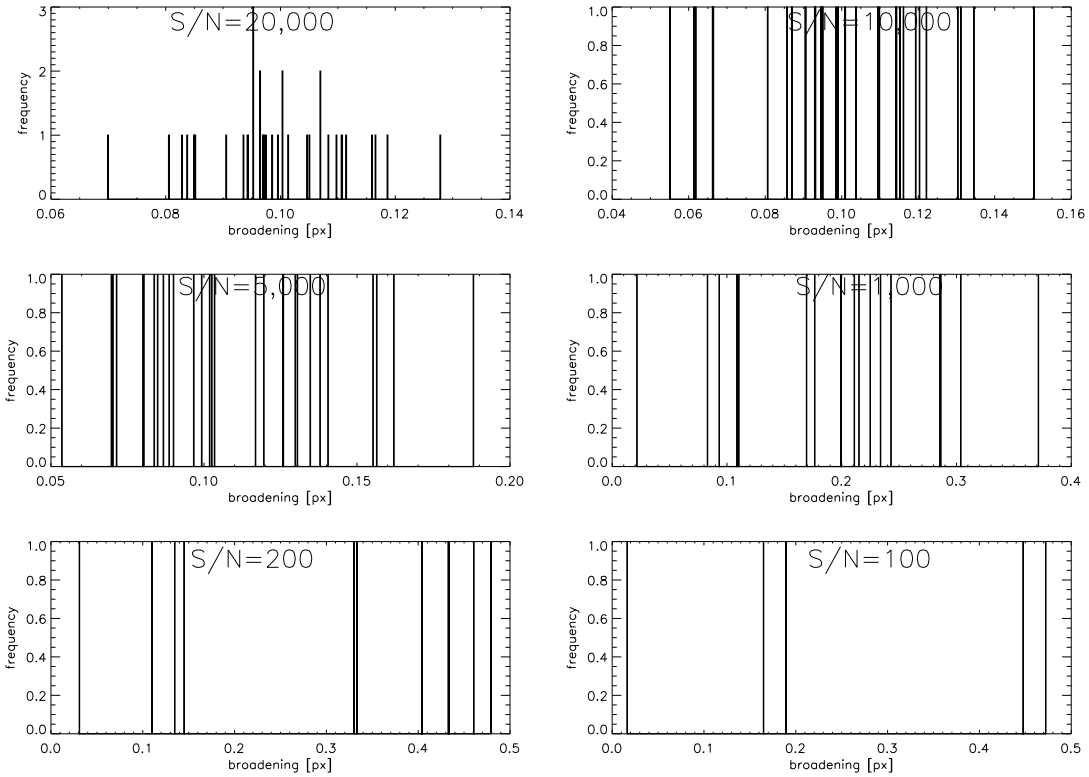

Figure 6.4: Six cleared histograms from different noise levels showing the broadening results of an artificially broadened spectral order (around 5600 Å) for a broadening of 0.10 pixel.

Dropping to a noise level of 1,000 or even smaller, the number of valid chunks drastically decreases causing the standard deviation of the worst S/N of 100 to be even lower than that of a S/N of 1,000 but this is a selection effect due to the cleaning. In general, the broadening median values are well reproduced within their errors (being the standard deviation divided by the square root of the number of valid chunks) except for the worst case with a S/N of 100.

Artificial broadening [pixel]	Noise level S/N	Determined median broadening [pixel]	Standard deviation [px]
0.10	20,000	0.099	0.012
	10,000	0.099	0.022
	5,000	0.103	0.032
	1,000	0.200	0.088
	200	0.40	0.16
	100	0.19	0.20

Table 6.3: Table with the median and standard deviation of the "cleaned" broadening deviation values determined by the broadening code for a broadening of 0.10 px and six different noise levels.

The next smaller broadening is those of 0.10 px with the resulting histograms of the different noise levels shown in figure 6.4. The determined broadening median value and the standard deviation can be found in table 6.3.

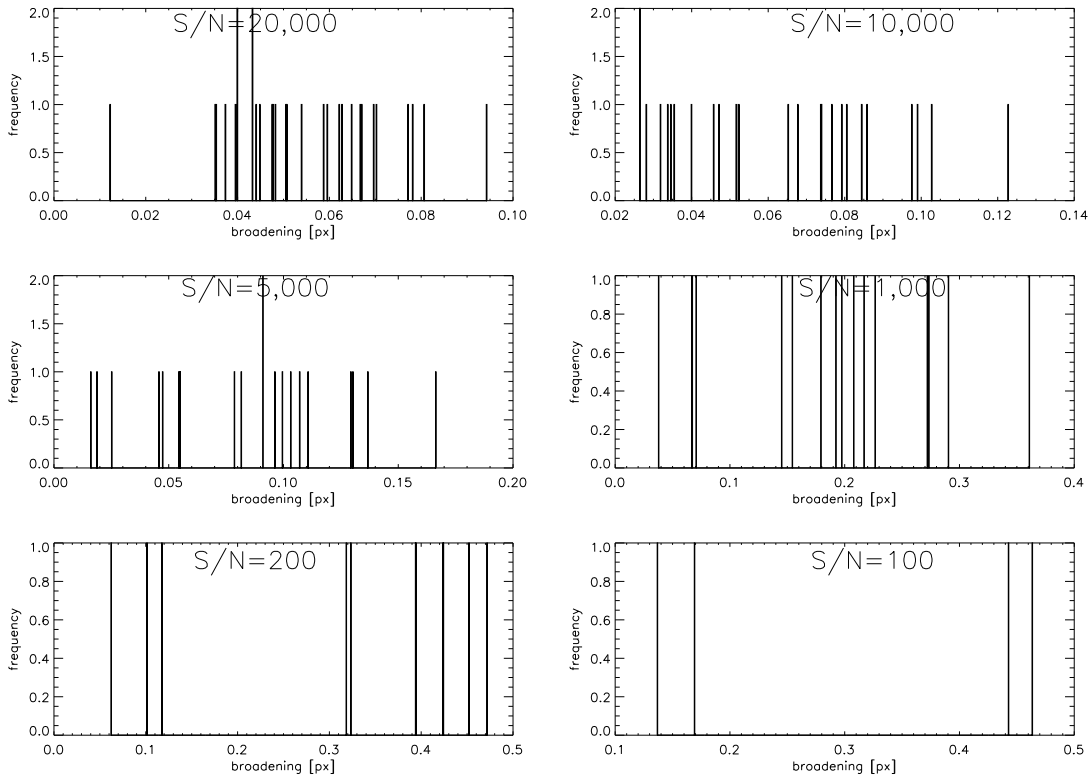

Figure 6.5: Six cleared histograms from different noise levels showing the broadening results of an artificially broadened spectral order (around 5600 Å) for a broadening of 0.05 pixel.

The situation is a little different here compared to the 0.25 px broadening case. The number of valid chunks drops noticeably beginning from a S/N value of 5,000 with the worst S/N of 100 having only a fistful of valid chunks left. The standard deviation increases with declining S/N as expected. Only the median values from the results down to a S/N of 5,000 can reproduce the input value of 0.10 px. After that only the noise is fitted and the broadening code is not able to determine the artificial broadening any more.

Artificial broadening [pixel]	Noise level S/N	Determined median broadening [pixel]	Standard deviation [px]
0.05	20,000	0.051	0.017
	10,000	0.065	0.027
	5,000	0.091	0.041
	1,000	0.192	0.089
	200	0.39	0.15
	100	0.44	0.17

Table 6.4: Table with the median and standard deviation of the "cleaned" broadening deviation values determined by the broadening code for a broadening of 0.05 px and six different noise levels.

Coming to the next case with a broadening of 0.05 px with the histogram of the "cleaned" broadening results to be found in figure 6.4. As before, the median values and the standard deviation of the results can be found in table 6.4.

Looking at the histograms, the decrease in valid chunk numbers starts even earlier with a S/N value of 10,000 and drastically drops with worse S/N. The broadening code can only reproduce the artificial broadening of 0.05 px for the highest S/N of 20,000 within its error with the S/N=10,000 broadening result being close but out of their error-range. From a noise level of 5,000 and worse the noise fitting wins against the artificial broadening.

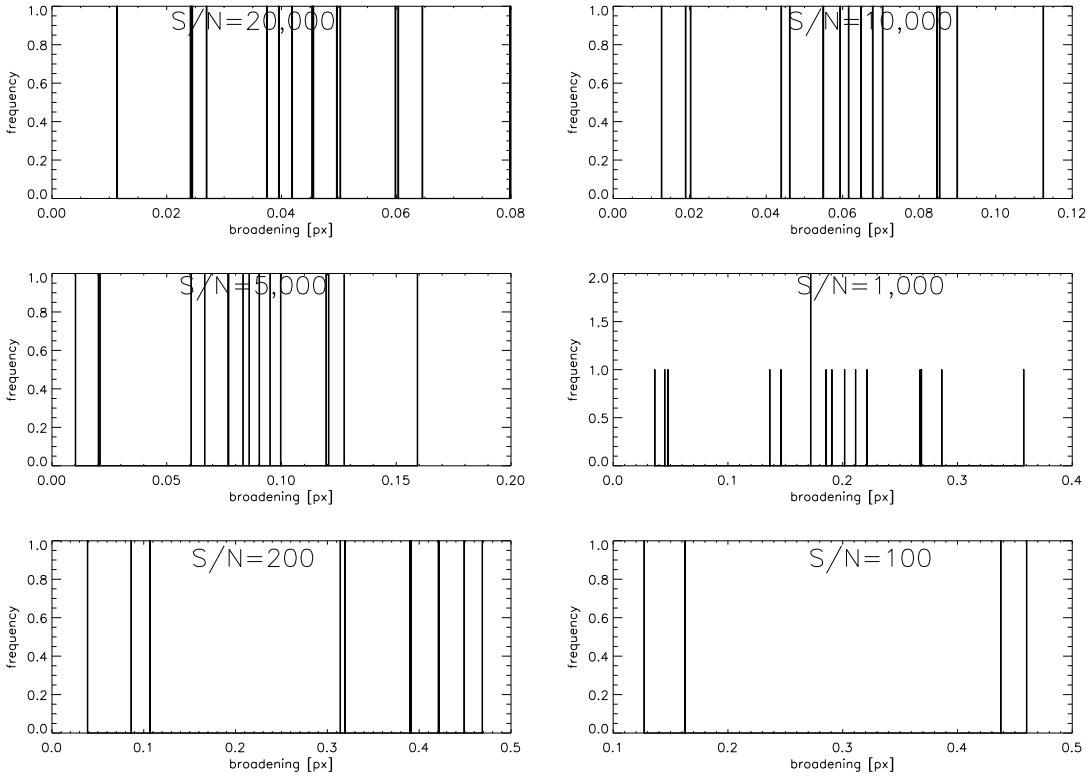

Figure 6.6: Six cleared histograms from different noise levels showing the broadening results of an artificially broadened spectral order (around 5600 Å) for a broadening of 0.01 pixel.

The lowest artificial broadening presented here of 0.01 px with the broadening result histograms shown in figure 6.6 is even more affected by noise. The number of valid chunks is drastically reduced even for a S/N of 20,000 and with none of the noise levels used here the broadening code is able to reproduce the very small artificial broadening.

The broadening results median values and the standard deviation are given in table 6.5. Clearly none of the results matches the input value. The noise levels applied to the artificially broadened spectrum suppress the searched broadening deviation completely.

The results from the more realistic spectra with artificial noise are strongly influenced by the chosen noise level. Though it is not impossible to measure sub-pixel differential broadening with the code the noise level overwhelms the broadening effect for most of the shown situations.

While for a broadening of 0.25 px the results are within range from a noise level starting with 200, for 0.10 px broadening this is only true for noise levels of 5,000 or more for these

simulations. An artificial broadening of 0.05 px or approximately 54 m/s (at 5600 Å) could only be reproduced with an extraordinarily high S/N of 20,000.

Artificial broadening [pixel]	Noise level S/N	Determined median broadening [pixel]	Standard deviation [px]
0.01	20,000	0.045	0.018
	10,000	0.062	0.027
	5,000	0.086	0.041
	1,000	0.191	0.080
	200	0.39	0.16
	100	0.44	0.18

Table 6.5: Table with the median and standard deviation of the "cleaned" broadening deviation values determined by the broadening code for a broadening of 0.01 px and six different noise levels.

While the apparently largest stars on the sky (of approximately 20 mas in diameter) can reach geometrical effects in the order of 0.06 px the needed noise levels to detect this broadening are far out of range. For nearby solar like stars, the expected geometrical effect is in the order of 0.01 px or less, which the simulations could not detect even with a S/N of 20,000.

The simulations have been done using only one spectral order (of 20 in case of the UVES middle CCD used here) meaning better statistics by a factor of about $\sqrt{20}$ when using all orders. But the stellar spectrum and the noise levels (of both the star and the iodine cell) are of different type as in the simulations. The stellar spectrum's noise distribution is affected by the blaze. So in reality the statistics might be a little less enhanced when using all orders.

Still the number of valid chunks (not stacking at the minimum/maximum or preset value of the broadening parameter) depends strongly on the noise level. The achieved noise level for the observations is less than 200 at maximum. Since the method depends on the modeling of the instrumental profile change between the template spectrum and the object spectrum it is not possible to add up several observations to enhance the signal-to-noise ratio.

Chapter 7

Results

7.1 Instrumental profile

The method used in this work as described in chapter 5 is based on the reconstruction of the observed spectrum by a multiplication of the (shifted and/or broadened) stellar template with the iodine template, which is then convolved with an appropriate model instrumental profile. While the iodine template simply is a super high-resolution FTS spectrum of the used iodine cell, the stellar template is not as easily accessible.

With most of the stars being too faint to be used with an FTS, also calculated spectra by a modern model spectrum code are not suitable because of the only vaguely known stellar properties (for example all elemental abundances) and limited modeling abilities of the model spectrum code. So the deal is to construct the stellar template from a pure stellar observation without the gas absorption cell.

The stellar template is created by the deconvolution of the instrumental profile from the pure stellar spectrum. The main problem and also the main disadvantage is the missing knowledge of the IP (including environmental effects like the light source, seeing and other conditional changes). Since for modeling the IP a stellar spectrum is already mandatory, it is not possible to directly gain the IP from the observed stellar spectrum.

To circumvent this problem a trick is used namely to use the IP of an iodine flatfield constructed with the available iodine template. This iodine flatfield should be observed shortly before or after the stellar spectrum to not allow for too strong environmental changes. Still, using the iodine IP for the stellar spectrum is only a crutch.

The iodine lines are used for determining the IP and to provide an accurate wavelength scale leaving all scientific information (here the wavelength shift and differential line broadening) to be gained from the stellar spectrum part that is modeled with the stellar template. So the modeling of the instrumental profile is very important as it is used in the beginning to create the stellar template and in the end to model the observed stellar spectrum with iodine.

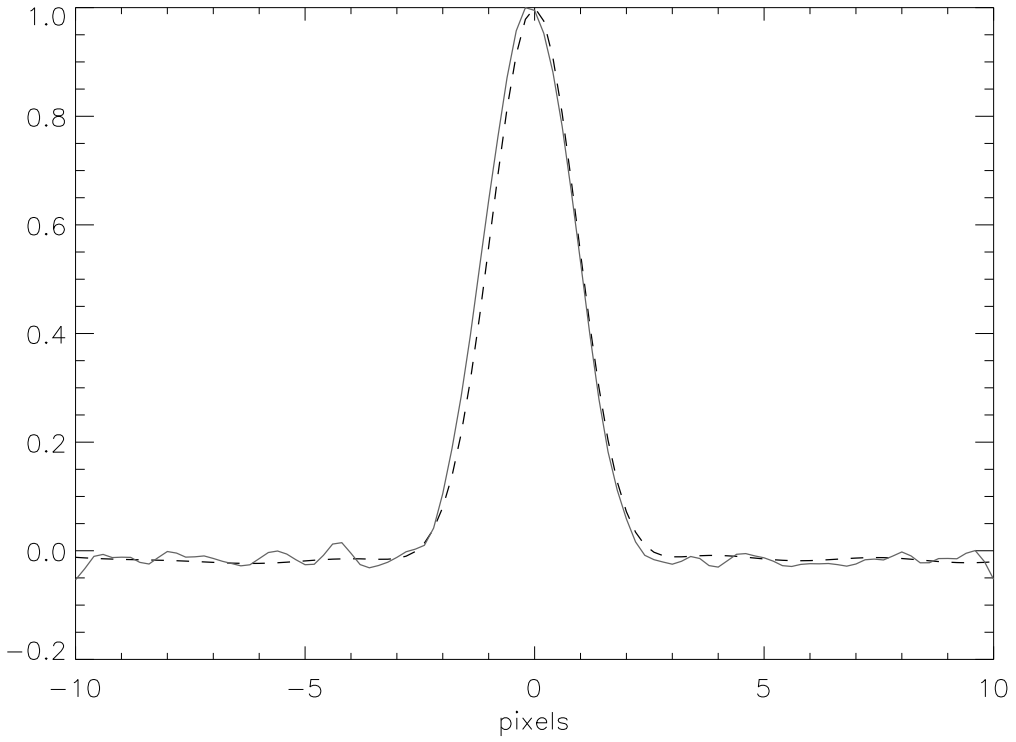

Figure 7.1: Example of a resulting instrumental profile for a 100 px spectrum part (chunk 26 of order 15) on a height normalized scale. The used model IP (dashed line) consists of a central Gaussian with 5 satellite Gaussians equally spaced on each side. For comparison the corresponding IP produced using the SVD model with 50 Eigenvalues is overplotted (solid line). Except for the slightly misaligned centering of the SVD model both IPs are in good agreement, justifying the use of the simpler multiple Gaussians model. For the small scale oscillations on the baseline, see text.

As suggested by Valenti et al. (1995) the original IP model of the used RV code consisted of a set of multiple Gaussians, namely a central Gaussian with several satellites on each side to model the wings of the central Gaussian. Although having successfully been applied for other telescope/spectrograph systems like the HET, this model failed for our UVES data producing unexpectedly shaped and poor fitting IPs far off a slightly modified central Gaussian shape. The failed model's satellite Gaussians had been restricted to be positioned within the central Gaussian.

In order to have a good fit, the model IP has been changed with the satellite Gaussians being distributed equally spaced along the whole pixel space. The final IP model has now one central Gaussian and six satellite Gaussians to each side positioned each 1.5 pixel along the baseline. The fixed satellite width is also 1.5 pixel to establish a good overlap of neighboring satellites (see also section 5.2).

With the new IP model a much better fit has been reached and the shape of the IP has now the shape of a slightly modified central Gaussian like reported by other sources (e.g., Bean et al. 2009). But outside of the IP core there are now unexpected small scale oscillations along the baseline that must be modeled. An example of such an IP can be found in figure 7.1 looking at the dashed line. To rule out special observing effects, an iodine flatfield from another observation from the UVES archive has been handled in the same way also

revealing small scale oscillations.

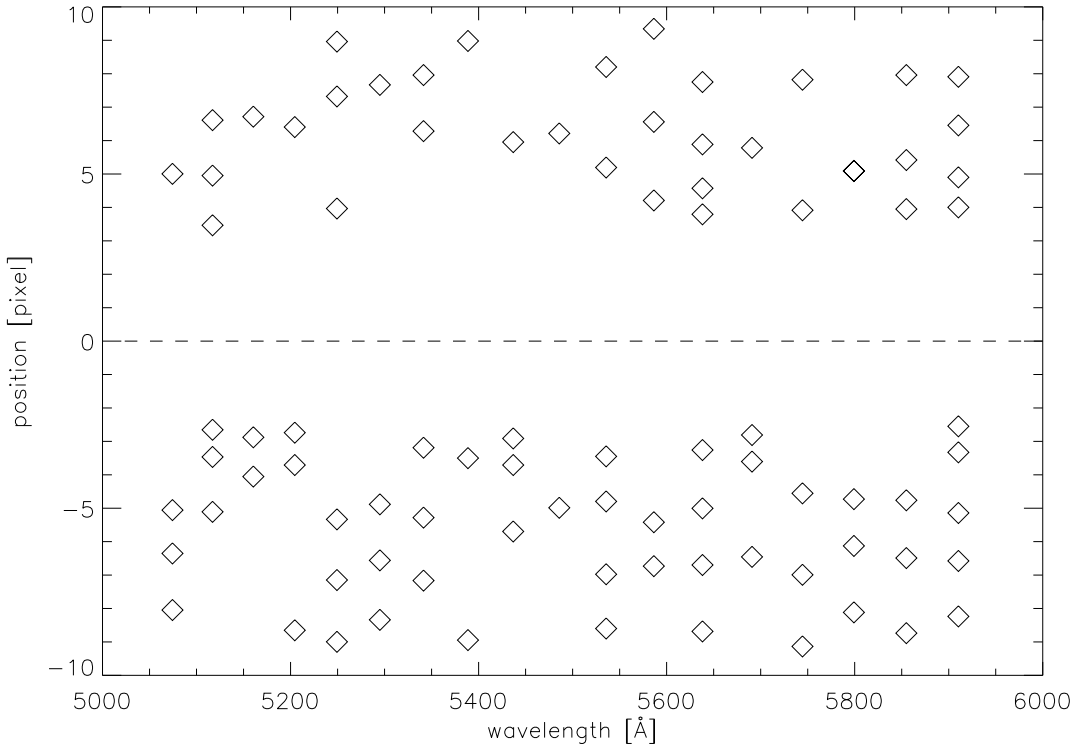

Figure 7.2: Example of the determined small scale oscillation extreme value (minima/maxima) positions for the instrumental profile of each chunk in order 11 using the multiple Gaussians model. The larger space in the middle corresponds to the IP core. The chunk IPs are sorted by their central wavelength showing no wavelength dependency of the extreme value positions.

In the simple case of a boxed shaped wavelength window of the spectrograph, the shape of an instrumental profile is a sinc curve originating from the Fourier transform. But then, the oscillation envelope curve of the minor maxima should decrease while going away from the IP core and their positions should vary with wavelength. In this case the observed small scale oscillations do not show such a height decrease and the positions of the extreme values (minima/maxima) as measured for the multiple Gaussian model IPs of spectral order 11 of the iodine flatfield (see figure 7.2) are randomly distributed.

Small scale oscillations have also been found by Seifahrt et al. (2010) (using a SVD model with 21 eigenvalues) and Bean et al. (2009) (using a multiple Gaussian IP model) for CRIRES (see IP plots therein). The origin of the small scale oscillations is not discussed in these papers.

To constrain the results from the used multiple Gaussian IP model, one spectral order of the same iodine flatfield has been segmented in the same way (into 39 chunks with 100 px each) and put into a Singular-Value Decomposition (SVD) code (as also used by Seifahrt et al. 2010) to check those IPs against our's. An example of such a SVD model IP can be found in figure 7.1 (solid line). The SVD IP follows the multiple Gaussian IP quite well but showing more details at the baseline due to the larger parameter space.

For the SVD IP the number of eigenvalues (usually 10 to 15) had to be increased by a factor of 4-5 to 40-60 eigenvalues to stabilize the fit. The small scale oscillation structures for the whole order as shown in figure 7.3 (with 50 eigenvalues) on the right remain constant for 40-60 eigenvalues with noise pickups starting at 60 eigenvalues. So this small scale oscillation structures are real. On the left image in figure 7.3 the Gaussian model IP structure for the whole order is plotted for comparison.

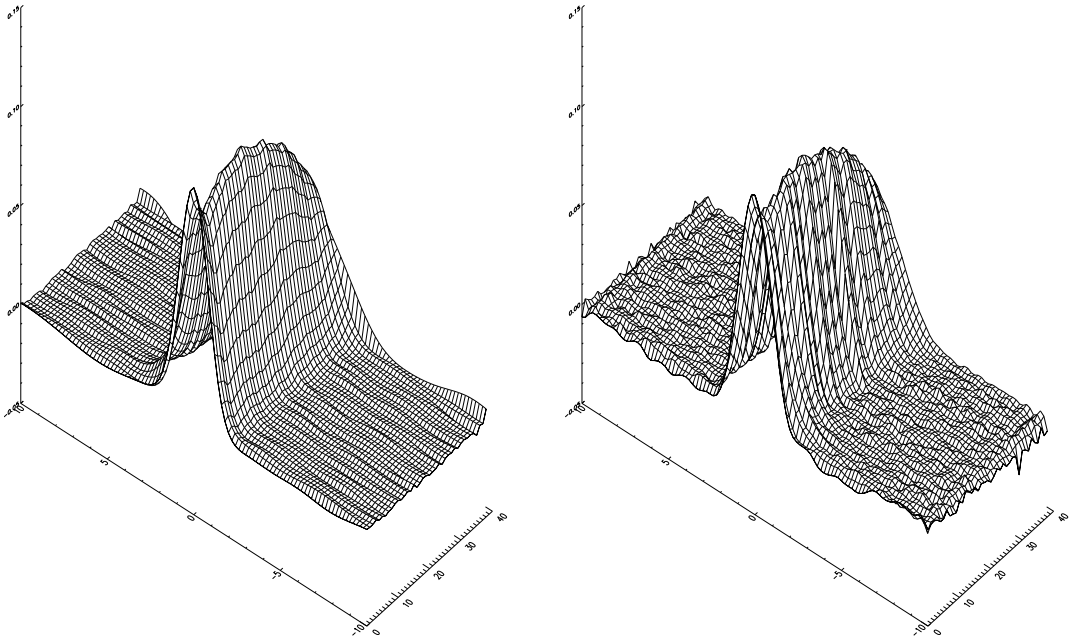

Figure 7.3: Surface plot example of a full order (order 15 with 39 chunks of 100 px each) distribution of the resulting IPs for each chunk. On the left image the used model IP distribution is shown with the corresponding SVD IP distribution on the right image. The chunk number axis starts from the bottom center continuing to the upper right, the axis to the upper left is the same pixel axis of a single IP as shown in figure 7.1. Both models are in good agreement especially when looking at the peak height distribution. The small scale oscillations at the baseline level (bottom right part of the images) can be noticed here even better with the SVD model showing more details because of the larger parameter space, see text for details.

Both structures are in good agreement especially when looking at the peak height distribution. This also means that the use of the Gaussian model is justified. It is clearly preferred to the SVD model with 50 eigenvalues since only 100 data points are available and there are further parameters (wavelength, velocity shift, broadening) to fit, so the number of free parameters can not be increased arbitrarily.

Since the RV code uses oversampling, this might cause numerical problems causing the small scale oscillations. Therefore, the interpolation method used in the RV code has been varied (linear, quadratic, cubic spline (used here) and sinc interpolation) and tested with the same spectrum. The small scale oscillations do remain in each case so this possibility can be eliminated.

Another possibility might be a more realistic approach to the origin of the instrumental

profile with the collimated roughly round beam of light falling on the tilted grating of the spectrograph. Then, the grating is not uniformly illuminated so the instrumental profile has not the shape of a sinc (or first spherical Bessel) function but that of a combination of (higher order) spherical Bessel functions. Together with non perfect optical elements this might explain the shape of the determined instrumental profiles. The modeling of the change in the instrumental profile is necessary due to variations in the seeing, mechanical- and temperature condition. The timespan between consecutive exposures of several minutes is too large to assume the instrumental profile to remain constant.

7.2 Radial velocity accuracy

The original code was designed to measure the radial velocity shift of the observed spectra relative to the template spectrum with a high accuracy. While this information is not the goal in this work it is still part of the code and easily accessible.

The radial velocity shift is calculated in a "normal" oversampled pixel space using an oversampling factor of four (additional subpixel per real pixel) before the radial velocity shift is fixed and the last step uses a much higher oversampling factor of 200 and more to determine the differential broadening.

Heliocentric Julian Date HJD	Observing time date, UTC[h:m:s]	position angle [degree]	radial velocity [m/s]
2453272.500541	2004-09-23 at 23:56:43.181	000	433.006
2453272.512702	2004-09-24 at 00:14:14.004	060	431.935
2453272.522534	2004-09-24 at 00:28:27.490	120	427.188
2453272.530628	2004-09-24 at 00:40:05.391	180	429.786
2453272.544214	2004-09-24 at 00:59:39.234	240	431.479
2453272.558227	2004-09-24 at 01:19:49.080	300	428.339
2453272.566879	2004-09-24 at 01:32:16.096	360	431.363

Table 7.1: Table with the mean radial velocity results (weighted mean relative to the template) for the spectra of ϵIndi with a mean of 430 m/s and a standard deviation of 2 m/s. The spectra have been observed over a time of about 1.5 hours of the same night. The maximal RV difference between these observations is about 6 m/s.

All observations used here have been obtained in one night within approximately one and a half hours between the observations of the first and the last position angle for one target star. Therefore, the scatter of the resulting radial velocity shift is a good indicator for the radial velocity shift accuracy. Coming back to the basic idea of this work that the width of a stellar line can be measured with a comparable accuracy as its position, the reached RV accuracy should also be a lower limit for the width measurement.

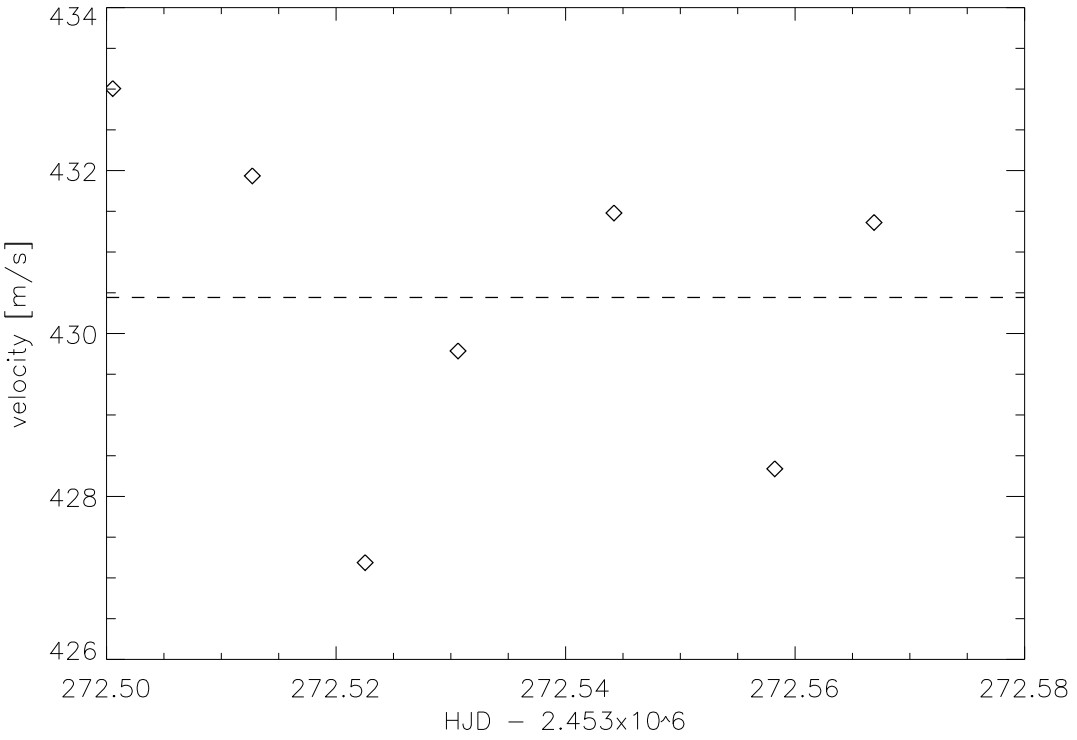

Figure 7.4: Radial velocity distribution (relative to the template) of observations of ϵ Indi of different position angles by their observing time (heliocentric julian date - HJD). The time between the first and the last observation is about 1.5 hours. The mean radial velocity is 430 m/s (indicated by the dashed line) with a standard deviation of 2 m/s. The difference between the minimum and maximum result is about 6 m/s.

The more than seven hundred determined radial velocity shift values per observation (one per chunk) have been formed into a single value by a weighted mean using the internally calculated errors. The relative velocity shift of each observation due to different observation times or earth's positions, respectively, have been removed from the results in advance to measure only velocity shifts caused by the target system's configuration.

For ϵ Indi the results for the seven different position angle spectra relative to the stellar template (of position angle zero) can be found in table 7.1. A graphical version of the RV results is given in figure 7.4 with the mean value indicated by the dashed line. The mean radial velocity shift for ϵ Indi is about 430 m/s with a standard deviation of 2 m/s. The scatter between the lowest and the highest values is about 6 m/s.

The general offset in radial velocity between the template and actually observed spectra, especially noticeable at the same position angle (0 and 360 degree), comes from the deconvolution used to create the stellar template. Therefore only relative values can be gained here.

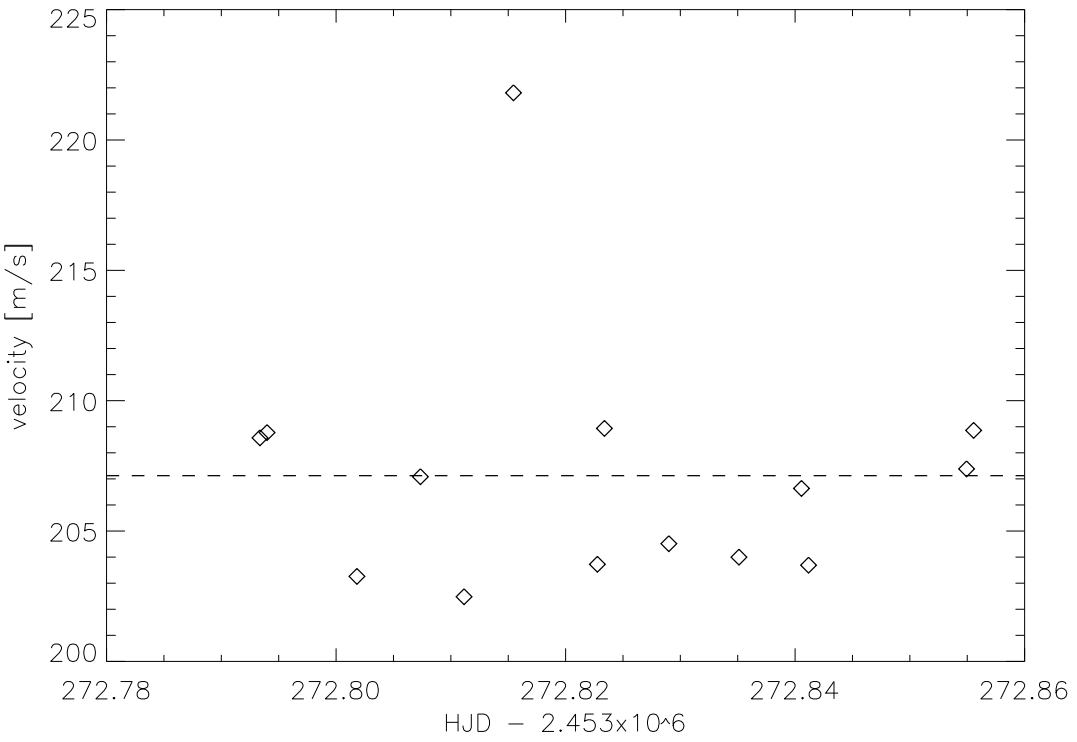

Figure 7.5: Radial velocity distribution (relative to the template) of observations of α Tau of different position angles by their observing time (heliocentric julian date - HJD). The time between the first and the last observation is about 1.5 hours. The mean radial velocity is 207 m/s (indicated by the dashed line) with a standard deviation of 5 m/s with one outlier. The difference between the minimum and maximum result is about 6 m/s ignoring the single outlier that would rise it to 19 m/s.

For α Tau the situation looks not much different. The radial velocity shift results can be found in table 7.2 and its visualization in figure 7.5. Here, each position angle is covered by two spectra to test for instabilities due to instrumental changes. The mean radial velocity shift is about 207 m/s with a higher standard deviation of 5 m/s due to the single outlier.

Ignoring the outlier, the scatter difference for α Tau between the lowest and highest values is with about 6 m/s the same as for ϵ Indi. Including the outlier it rises to 19 m/s. The scatter between spectra of the same position angle is a little less than 6 m/s but as high as 5 m/s indicating an only minor influence of the change in position angle to the accuracy.

Both stars show a maximal scatter difference in the radial velocity shift of about 6 m/s (ignoring the single outlier for α Tau). This seems to be a good estimate for the accuracy of the radial velocity measurement with the UVES data and the used code. It also indicates that the third star GJ 86 with the smallest geometrical effect in the simple approximation of about 3 m/s (radius) is out of reach of the achievable accuracy by the lower limit as judged from the RV accuracy.

Heliocentric Julian Date HJD	Observing time date, UTC[h:m:s]	position angle [degree]	radial velocity [m/s]
2453272.793368	2004-09-24 at 06:59:22.652	000	208.575
2453272.793986	2004-09-24 at 07:00:15.996	000	208.777
2453272.801818	2004-09-24 at 07:11:32.825	060	203.261
2453272.807348	2004-09-24 at 07:19:30.517	060	207.084
2453272.811154	2004-09-24 at 07:24:59.316	120	202.480
2453272.815460	2004-09-24 at 07:31:11.328	120	221.809
2453272.822770	2004-09-24 at 07:41:42.664	180	203.725
2453272.823384	2004-09-24 at 07:42:35.719	180	208.937
2453272.828997	2004-09-24 at 07:50:40.714	240	204.516
2453272.835105	2004-09-24 at 07:59:28.529	240	203.998
2453272.840554	2004-09-24 at 08:07:19.230	300	206.635
2453272.841171	2004-09-24 at 08:08:12.534	300	203.691
2453272.854941	2004-09-24 at 08:28:02.190	360	207.383
2453272.855557	2004-09-24 at 08:28:55.405	360	208.861

Table 7.2: Table with the mean radial velocity results (weighted mean relative to the template) for the spectra of α Tau with a mean of 207 m/s and a standard deviation of 5 m/s. The spectra have been observed over a time of about 1.5 hours of the same night. The maximal RV difference between these observations is about 6 m/s ignoring the single outlier with a difference of 19 m/s.

7.3 Broadening results

The differential broadening has been measured for a full set of spectra for each position angle using a stellar template created using the IP from an iodine flatfield by deconvolving this IP from a pure stellar spectrum of α Tau and ϵ Indi, respectively. Details on the spectra used for the template creation can be found in table 7.3.

Heliocentric Julian Date HJD	Observing time date, UTC[h:m:s]	position angle [degree]	type
2453273.003524	2004-09-24 at 12:00:38.249	000	I_2 flatfield spectrum
2453272.777871	2004-09-24 at 06:37:03.763	000	pure α Tau spectrum
2453272.584747	2004-09-24 at 01:58:09.342	000	pure ϵ Indi spectrum

Table 7.3: Table with details of the spectra used to create the stellar template for α Tau and ϵ Indi with the help of the instrumental profile determined from the iodine flatfield ($S/N \approx 800$).

The stellar template spectra of both stars have been calculated using an oversampling factor of six to achieve a better sampling of the instrumental profile. The instrumental profile has been determined with the multiple Gaussian model of one central and six

equally spaced satellite Gaussians to each side. Therefore, the FTS based iodine template spectrum has been convolved with the IP model and its parameters (the heights of the Gaussians) have been optimized to establish a good agreement with the observed iodine flatfield spectrum.

Then those IPs (one for each spectral chunk of 100 px) from the iodine spectrum are used to be deconvolved from the pure stellar spectrum to create the stellar template spectrum. This stellar template spectrum is the base for all further modeling (in particular the wavelength shift and the differential broadening) of spectra that has been observed through an iodine cell.

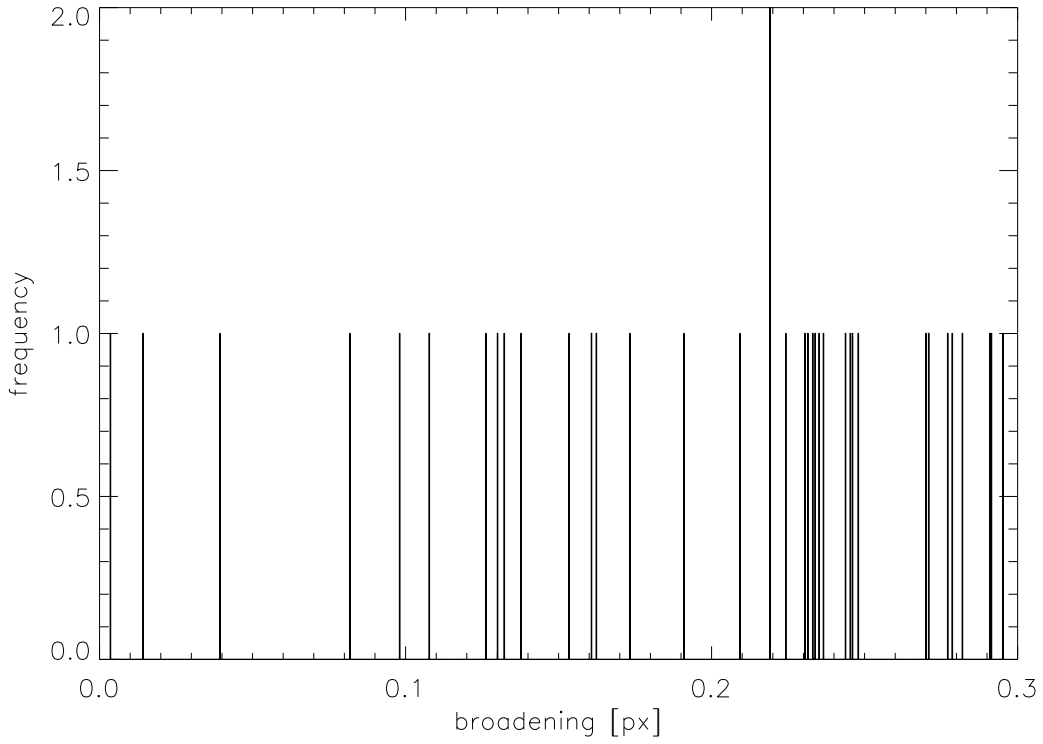

Figure 7.6: Differential broadening histogram example (relative to the template) of an α Tau observation with a position angle of 180°. Only cleaned chunks with values not being equal to the minimum (0.0 px), maximum (0.3 px) or initial (0.1 px) values are counted here leaving only less than 10% valid chunks. The distribution is neither of Gaussian nor of Poisson type but seems to be random like those from the simulation section with too little valid chunks.

The differential broadening is applied by a broadening profile (BP), a simple spherical broadening function, which is convolved with the shifted stellar template. The differential broadening between two spectra of different position angle is very small therefore a much larger oversampling is needed to sample the broadening profile.

Since the calculation time rises with the oversampling (i.e., more subpixels), the calculations are splitted into two parts. The "classical" part where the wavelength calibration and finally the wavelength shift is calculated is using a "normal" oversampling factor of four while for the last part the wavelength shift is held constant and only the differential broadening and the IP is calculated with a much higher oversampling factor.

The calculations presented here for determining the differential broadening are using a large oversampling factor of 200 in case of α Tau (radius effect of about $\approx$ 75 m/s or 0.07 px) and of 500 in case of the much smaller star ϵ Indi (radius effect of about $\approx$ 7 m/s or 0.006 px) to adopt the very small differential broadening profile to be distinguished from the Delta function.

For each spectrum the differential broadening width has been determined with a restricted parameter range between the minimum broadening of zero pixel (BP equals the delta function) and a chosen maximum broadening level of 0.3 px far off the expected values. Only positive broadening can be measured since the broadening profile can only reproduce the template spectrum (that is already broadened since it is created from an observed spectrum) at minimum or make it broader than the stellar template spectrum.

The observed spectrum is divided up into about 750 chunks of 100 px each to account for localized IP changes. Therefore, about 750 broadening results are computed. For the selected targets used here, most of the broadening values are not usable. A selection criterion has been used to distinguish "valid" broadening results from those that are representing the minimum, maximum or initial value as used for the calculations.

Heliocentric Julian Date (HJD)	Observing time date, UTC[h:m:s]	position angle[°]	broadening median[px]	broadening error [px]	valid chunks
2453272.793368	2004-09-24 at 06:59:22.652	000	0.2138	0.0017	46
2453272.793986	2004-09-24 at 07:00:15.996	000	0.2004	0.0015	55
2453272.801818	2004-09-24 at 07:11:32.825	060	0.2264	0.0017	42
2453272.807348	2004-09-24 at 07:19:30.517	060	0.2103	0.0019	40
2453272.811154	2004-09-24 at 07:24:59.316	120	0.2201	0.0022	38
2453272.815460	2004-09-24 at 07:31:11.328	120	0.1892	0.0027	34
2453272.822770	2004-09-24 at 07:41:42.664	180	0.2440	0.0022	36
2453272.823384	2004-09-24 at 07:42:35.719	180	0.2242	0.0021	38
2453272.828997	2004-09-24 at 07:50:40.714	240	0.2195	0.0019	41
2453272.835105	2004-09-24 at 07:59:28.529	240	0.1936	0.0017	47
2453272.840554	2004-09-24 at 08:07:19.230	300	0.1844	0.0022	40
2453272.841171	2004-09-24 at 08:08:12.534	300	0.1985	0.0014	40
2453272.854941	2004-09-24 at 08:28:02.190	360	0.1806	0.0021	34
2453272.855557	2004-09-24 at 08:28:55.405	360	0.2057	0.0023	37

Table 7.4: Table with the differential broadening results (relative to the template) for the spectra of α Tau with the median and the error as well as the number of valid chunks. Two data points for each position angle has been measured. The listed spectra have been observed over a time of about 1.5 hours of the same night. The template spectrum has been of position angle zero. An oversampling factor of 200 has been used to calculate the differential broadening.

The maximum value is unphysical while the minimum value is also not usable because it contains also all negative values that can not be modeled. The exact initial or starting value for the broadening indicates no successful fitting. The remaining less than 10% "cleaned" broadening values are used to calculate a mean broadening value for each spectrum. A

typical histogram of the cleaned broadening values of a spectrum of α Tau is illustrated in figure 7.6.

The cleaned broadening values are distributed over the whole parameter range from zero to 0.3 px broadening. Neither is the distribution of Gaussian nor of Poisson type but seems random. The small number of remaining cleaned values together with them not gathering around a mean value indicates that these values are fitted noise like already observed at the simulations in section 6.3 for too small broadening with too large noise.

Although there is no apparent distribution of the broadening values we assume Gaussian statistics here, using the median broadening value and the standard deviation divided by the square-root of the number of valid chunks as the estimate of the corresponding error. The median broadening value with its error, the number of valid chunks and the time frame of the calculated spectra are tablelized in table 7.4 for α Tau and in table 7.5 for ϵ Indi for a full set of different position angles (from zero to 360° in steps of 60°).

The calculations for α Tau for each spectrum using an large oversampling factor of 200 took about 3-4 hours of computing time on an Intel Xeon quad-core clocked with 2.5 GHz. The used MPFIT fitting algorithm nicely auto-parallizes on the available four CPU cores. Due to the small chunks, the memory usage is negligible.

Heliocentric Julian Date (HJD)	Observing time date, UTC[h:m:s]	position angle[°]	broadening median[px]	broadening error [px]	valid chunks
2453272.500541	2004-09-23 at 23:56:43.181	000	0.2041	0.0013	51
2453272.512702	2004-09-24 at 00:14:14.004	060	0.2335	0.0019	39
2453272.522534	2004-09-24 at 00:28:27.490	120	0.2056	0.0017	52
2453272.530628	2004-09-24 at 00:40:05.391	180	0.2405	0.0020	35
2453272.544214	2004-09-24 at 00:59:39.234	240	0.2007	0.0021	38
2453272.558227	2004-09-24 at 01:19:49.080	300	0.2004	0.0018	40
2453272.566879	2004-09-24 at 01:32:16.096	360	0.2193	0.0019	43

Table 7.5: Table with the differential broadening results (relative to the template) for the spectra of ϵ Indi with the median and the error as well as the number of valid chunks. The listed spectra have been observed over a time of about 1.5 hours of the same night. The template spectrum has been of position angle zero. An oversampling factor of 500 has been used to calculate the differential broadening results.

For the calculations of ϵ Indi a large oversampling factor of 500 has been used to account for its much smaller apparent diameter. The larger oversampling factor drastically increased the computing time to 17-18 hours per spectrum on the same machine.

Visualizing the distribution of the mean differential broadening results with their error bars versus the position angle for both stars can be found in figure 7.7 for α Tau and figure 7.8 for ϵ Indi.

For α Tau two spectra of each position angle have been calculated to search for discrepancies within the same instrumental configuration. The calculated differential broadening values of the same position angle are only partly compliant with themselves within the error bars. For the position angles 120 and 240° the error bars are out of range and for

360° just in range. That means that the typical error bars of about 0.002 px might be underestimated.

Looking at the measured broadening values, the results differ strongly from the expected values. The differential broadening values should be of the same order as the expected geometrical effect of the apparent stellar radius, i.e., an amplitude of about 0.07 px for α Tau and of about 0.006 px for ϵ Indi.

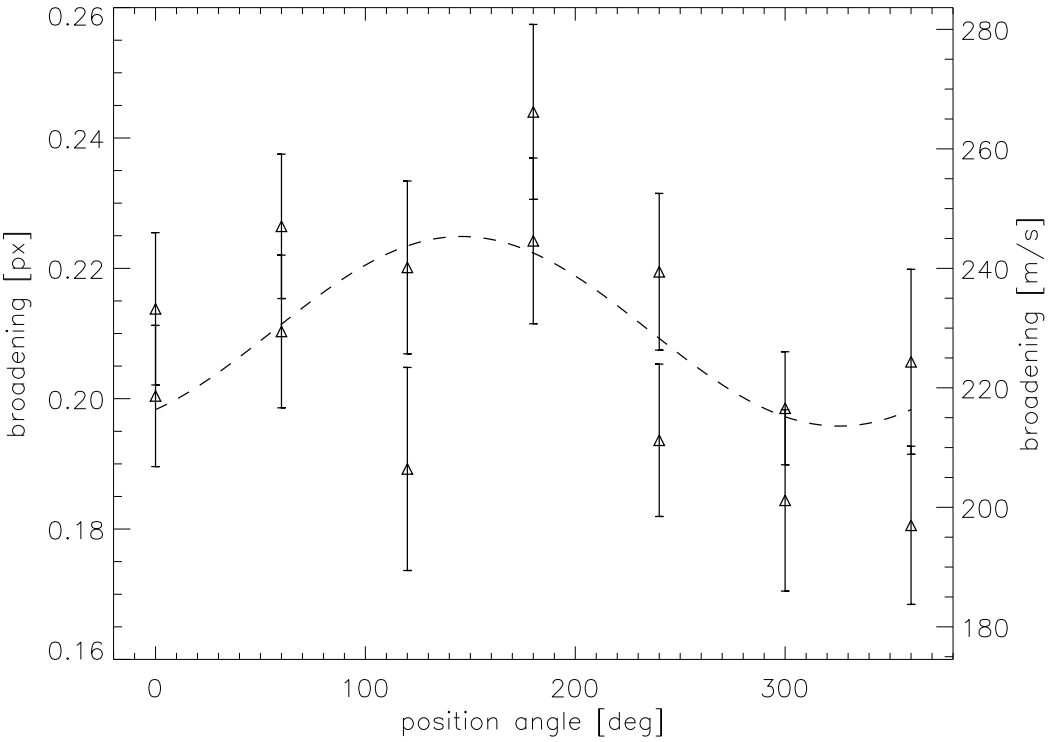

Figure 7.7: Differential broadening distribution (relative to the template) of observations of α Tau of different position angles. Each position angle is covered by two data points for stability comparison. The time between the first and the last observation is about 1.5 hours. A sinusoidal fit is overplotted to the data by the dashed line. The maximum of the fit curve is at position angle 146 ± 35 degree.

Instead, the measured values range roughly between 0.18 and 0.24 px with a mean of about 0.21 px for α Tau and between 0.20 and 0.24 px with a mean of about 0.22 px for ϵ Indi. There seems to be an unexpected offset in the order of the mean broadening value of about 0.21-0.22 px instead of values scattering around zero with an amplitude in the order of the expected geometrical effect. As mentioned before, negative broadening can not be modeled and would not appear on the graph.

Since the broadening values scatter around such a large value of about 0.21 px compared to the expected geometrical effect, this really might be an offset to the data. The question arises if there is a physical reason for such an offset?

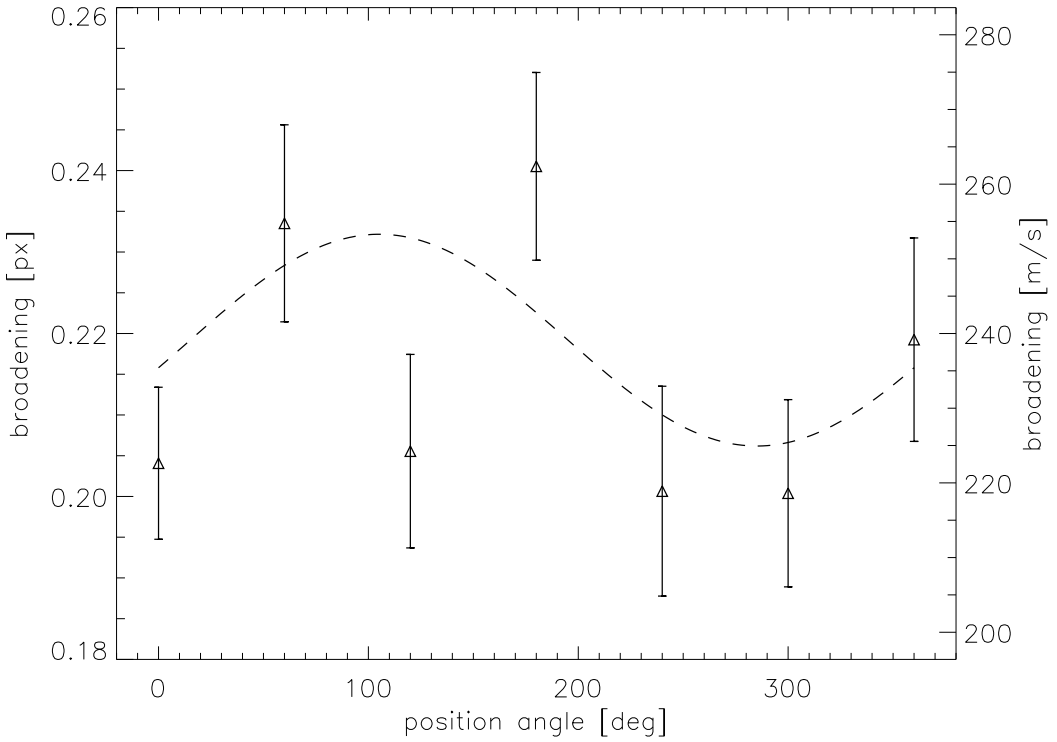

Figure 7.8: Differential broadening distribution (relative to the template) of observations of ϵ Indi of different position angles. The time between the first and the last observation is about 1.5 hours. The sinusoidal fit overplotted by the dashed line has its maximum at position angle 105 ± 41 degree.

A physical offset can only be produced by a smaller than expected stellar template that is the base for all calculations performed to determine the differential broadening. Indeed, the stellar template is a deconvolved stellar spectrum but the instrumental profile used for the deconvolution has a different origin. Namely the IP from the iodine flatfield. That means, a completely different light source has been used, the target star on the one hand and a flatfield lamp on the other hand that leads to a different illumination characteristic.

With the flatfield lamp's homogeneous illumination of the whole slit in contrast to the seeing disc's illumination of the target star, the IP gained from a flatfield observation might be broader than from an observation of a stellar source. Using this "amplified" IP to deconvolve it from a stellar spectrum leads to a less broad template than with the (unavailable) matching stellar IP. So this might be a reason for the offset.

Assuming there is a physical reason for the offset, the data has been fitted with sinus curve on top of an offset. The expected broadening distribution with position angle must be 360° periodical, where the slit again has the same orientation as for zero degree.

The calculations for the special cases of a parallel or antiparallel spin-slit orientation in chapter 2 and 3 result in a maximal or minimal broadening with values in between for other orientations. Therefore, a sinusoidal curve is a good approximation of the expected situation.

Such a sinusoidal curve including a constant offset ($A \cdot \sin(PA + PA0)$ +offset, with A the amplitude and PA (PA0) the position angle (shift)) has been fitted to the data using

the MPFIT non-linear fitting routine. The fit for the two target stars used here has been overplotted as a dashed line to figure 7.7 for α Tau with a maximum at 146 ± 35 degree and to figure 7.8 for ϵ Indi with a maximum at 105 ± 41 degree.

Already when looking with the blank eye the best fit sinus fits only poor with missing the error bars of several data points. Even if one disregards the lowest data point for a position angle of 120° of figure 7.7 for α Tau (due to its large RV scatter as mentioned in section 7.2 for this spectrum), the fit remains poor, even more obvious in figure 7.8 for ϵ Indi.

Taking a closer look to the fit for α Tau, the best fit amplitude is with about 0.03 px only half as large as expected by the star's geometrical effect of about 0.07 px. For ϵ Indi the fitted amplitude of about 0.04 px differs even stronger from the expected value of 0.006 px by the geometrical effect. As for the offset the amplitudes for the sinus fit of both stars are close together.

A typical way to measure the fit quality of a model curve is to look at the χ^2 value. The χ^2 value is the sum of the squared deviation of a data point y_i from its fit point $y_{fit,i}$ divided by the noise σ_i

$$\chi^2 = \sum_i \frac{(y_i - y_{fit,i})^2}{\sigma_i^2}$$

If the fit would follow the data within the noise limits (i.e., being a good fit) then the deviation for each data point would be near to the noise, i.e., the fraction would be near 1, and the sum would be near the number of data points.

Furthermore, when dividing the χ^2 by the fit's degree of freedom (dof, i.e., the effective number of data points given by the number of data points minus the number of free parameters used for the fit) we get the reduced χ^2 value $\chi^2_{red} = \chi^2/dof$, which should be near one for a good fit within the error bars.

For the sinusoidal fits used here the χ^2 values of both stars are with $\chi^2_{\alpha Tau} \approx 0.45$ and $\chi^2_{\epsilon Indi} \approx 0.23$ lower than one and the reduced χ^2 values even closer to zero with $\chi^2_{red,\alpha Tau} \approx 0.04$ and $\chi^2_{red,\epsilon Indi} \approx 0.02$. Reduced χ^2 values of less than one represent either a perfect fit, which is obviously not the case when looking at the graph, or point to a problematic situation of the following types.

First, overestimated errors can cause the reduced χ^2 value to drop below one but as mentioned earlier the error bars used here are underestimated at best when looking at the results for identical position angles in figure 7.7. Second, an inappropriate fit model with too much freedom unphysically fitting each data point ignoring the noise can cause reduced χ^2 numbers lower than one. Third, fitting noise can also let the reduced χ^2 value to be too small.

The last two situations are worth looking into a little deeper. The used model of the sinusoidal curve with an offset can only be justified partially. The physical differential broadening data must be 360°-periodical with a maximum and a minimum case separated by 180° caused by the derotator orientation and the following geometrical effect as shown in chapter 2. So a sinusoidal curve is justified but there is no physical need for an offset. Although the offset might be explained by the stellar template creation as mentioned earlier this does not necessarily make the data real.

For the last situation of the data showing mainly noise there are some strong arguments. From the about 750 measured values (one for each chunk) the majority is unusable because it represents the model's limits and only a small fraction of less than 10% have been used to calculate a combined value for each spectrum. Also the distribution of the measured broadening values (see also the histogram in figure 7.6) show no crowding at a certain mean value but seem random.

The same situation can be observed in the simulations chapter in section 6.3 when the noise level is too strong to measure the artificial broadening. Then the number of valid chunks is drastically decreased and only the noise level is fitted resulting in a scattering around an offset value just like for the real data measured here.

To strengthen the argument that the fit is not excellent (by the low χ^2) but rather poor, a simple test can be done. For the R^2 statistic the summed and squared deviations between the data points y_i and the actual fit $y_{fit,i}$ are compared to those summed and squared deviations of the data points to a horizontal line going through their mean value $\overline{y}$ by

$$R^2 = 1 \; - \; \frac{\sum (y_i - y_{fit,i})^2}{\sum (y_i - \overline{y})^2}$$

The R^2 value usually ranges between 0 and 1 with 0 meaning the data points matching the horizontal line and 1 meaning the fit curve perfectly represents the data. For the sinusoidal fit of the measured data of α Tau $R^2_{\alpha Tau} \approx 0.29$ and of ϵ Indi $R^2_{\epsilon Indi} \approx 0.18$. The R^2 statistics for both stars show, that the data is better fitted with a horizontal line than with the used sinusoidal curve.

Summarizing all mentioned points, it is justified to say that the measured data for both stars is mainly noise and do not represent the differential broadening caused by the spin-slit dependent combined broadening effect of the stellar rotation and apparent radius relative to the template spectrum.

With the available data quality it was not possible to measure the spin-slit orientation of the selected target stars. Due to the modeling specifics it is in principle not possible to enhance the S/N by adding up spectra of the same position angle, which would disable the possibility of the modeling of the change in the instrumental profile that is a base of the used method.

Chapter 8

Discussion and Outlook

8.1 Summary

This work introduced a principle to measure the orientation of spin axis of stars with spectroscopic means. The knowledge of the orientation of the stellar spin can give insights to the theory of planet formation or stellar system formation. The orientation of the spin axis is also interesting for multiple star systems and systems with a circumstellar envelope.

In this work a spectroscopic method of measuring the stellar spin orientation has been derived from basic physical principles of grating spectrographs. The stellar line broadening has been shown to base upon the combined effect of stellar rotation and the apparent stellar elongation. The combined broadening effect depends on the alignment of the stellar spin and the spectrograph's slit orientation or dispersion axis, respectively.

The dependencies of the resulting broadening deviations between spectra of different spin-slit alignments with the intrinsic and the rotational broadening widths have been numerically analyzed. An estimation formula for the line width has been developed $w = \sqrt{v_{\mathrm{Dop}}^{1.9730} + v_{\mathrm{rot}}^{1.9247}}$, which is close to a simple double Gaussian estimation.

The combined broadening effect is wavelength dependent due to the wavelength dependent limb darkening in the order of about half a meter per second for a wavelength region ranging from 5,000 to 6,000 Å. The apparent diameter of even nearby stars are very small (in the order of milliarcseconds) so is the resulting broadening deviation of different spin-slit alignments.

Thinking in an analogy of an analytical line profile, the line width should be measurable with a comparable accuracy as the line position. Therefore, a similar approach as for measuring very small radial velocity shifts of planetary systems has been chosen including spectroscopic measurements through a gas absorption cell. A radial velocity code has been extended with an additional broadening profile applied to the stellar template spectrum to also measure broadening deviations. With the already broadened stellar template a much higher oversampling factor was necessary to model the differential broadening profile causing much longer computing times.

The principle ability of the applied method to measure such small broadening deviations has been shown with artificially broadened spectra. But the simulations including realistic

noise levels failed to reproduce the known differential broadening for very small broadening effects (in the order of meters per second or 1% of a pixel) as expected for nearby stars.

Then the program was applied to real spectra of two stars $\alpha\,Tau$ and $\epsilon\,Indi$, observed with VLT/UVES aiming at $R \propto 100,000$, with an expected broadening amplitude of $w_{\alpha Tau} \approx 70$ m/s and $w_{\epsilon Indi} \approx 7$ m/s. The results that have been found indicate, that only noise has been fitted. The used method was not able to measure the spin-slit alignment and spin orientation of these stars.

8.2 Discussion

As mentioned in the summary and in the results chapter the differential broadening due to the different slit-spin alignments of the UVES spectra could not be measured. Although the expected effect of the maximal broadening deviation (by the apparent stellar radius) of about $w_{\alpha Tau} \approx 70$ m/s and $w_{\epsilon Indi} \approx 7$ m/s is larger than or in the order of the achieved radial velocity accuracy of about 6 m/s, the broadening could not be measured. The question arises, why this was not possible and what are the problems with this special method in general.

There are several numerical processes involved in the used method, which is based upon a broadening extended radial velocity method, like interpolation (oversampling, new wavelength grid) and convolution (deconvolution for the stellar template; convolution of the broadening and instrumental profile) that are not lossless. While a radial velocity induced wavelength shift is applied by a simple Doppler factor, the differential broadening can only be handled with a broadening profile that is convolved with the stellar template spectrum.

The peaks in the spectrum are only slightly affected and their positions (shift) remain mostly uninfluenced by a little extra numerically caused erroneous broadening. But for measuring small broadening effects, they are mainly affected by this numerically broadening. Additionally, a small erroneous radial velocity shift has a larger effect than broadening deviations on the fitting mechanism's χ^2 due to the displaced line peaks.

The instrumental profile (IP) has also to be taken into account. The IP affects both the stellar and the gas cell template spectrum that are multiplied in advance. The broadening affects only the stellar template, but the observed spectrum (or the model) is dominated by the large number of gas cell lines. Influenced mostly by them a slightly mistaken IP renders the differential broadening measurements impossible.

The IP acts in the same way as the differential broadening profile with a convolution of the spectrum both resulting in a higher broadened spectrum. In other words the IP can counteract the differential broadening measurements. Hence, radial velocity shift and differential broadening are two of a different class of parameters, they are differently affected by the spectrum modeling.

There are more limitations with measuring broadening since only positive broadening can be measured with a broadening profile. The broadening profile can only be as small a Delta function (i.e., no extra broadening) or larger. This leads to problems with the already broadened stellar template. It must have weaker broadening than the object's spectrum (which is a priori unknown) or the method fails. In contrast, the radial velocity shift

can be easily applied in both directions, which is in general not possible with differential broadening.

The broadening is hugely dependent on the stellar template and therefore the way it is created. Since the actual IP of an observed stellar spectrum is unknown, the IP of the gas reference cell's flatfield is used instead and deconvolved from the stellar spectrum to create its template. A completely different illumination enters this IP, the flatfield lamp versus the seeing disc of the star, which can also influence the accuracy of small broadening measurements.

So, summed up, it is more demanding to measure a broadening deviation than a radial velocity shift since the broadening is more affected by the way the spectrum modeling is done. There are too many processing steps that have a similar effect and can influence or render the measurement impossible. Furthermore, the spectrum extraction should also be taken into account, in which processing of the spectral image information can get lost.

8.3 Outlook

A possible way to enhance the used method would be to use a template that is not already influenced by the stellar rotation. Then, the stellar template would always be less broadened (by a huge amount) than any of the object spectra and also the broadening function is now known to be the rotational broadening function (including limb darkening).

In an ideal world such a spectrum could be produced by a theoretical spectrum modeling code but in reality the star's properties are too unknown (all elemental abundances, temperature and pressure structure etc.) and such code's ability to model a realistic spectrum is too restricted, so that this is not applicable here. With a precise measurement the star's rotation velocity could be deconvolved from a spectrum, but then there are already two (numerical and in general not unambiguous) deconvolutions involved to create the stellar template, which does not help the case.

So looking at the failure of the broadening extended radial velocity method, other approaches may be more promising. The most direct way would be to measure the tilting of the spectrum in the 2D spectral image itself. But the scale is only a small fractions of a pixel here, so the question is how to translate this into a working method. Using extracted spectra, another method would be to analyze them with Fourier transformation according to the measurements of differential rotation of stars.

Furthermore, the spectra of different position angles can be directly compared (with some kind of cross-correlation for example) without large processing in the beginning. But in this case the spectra should be almost identical except for the searched effect of the spin-slit alignment. To avoid the usual necessity of consecutive observations with changing external conditions (like seeing, pressure shifts etc.) a tool to enable simultaneous observations with different spin-slit alignments would be needed.

The development of a differential derotator device, with the ability to split the telescope's ray of light into paths with different spin-slit alignments (by a derotator) and feeding them together into the spectrograph, is currently under development by Anna-Lea Lesage at Hamburger Sternwarte.

Acknowledgment

The author is beneficiary of a Ph.D. scholarship of The Research Training Group / Graduiertenkolleg GRK 1351/1 "Extrasolar Planets and Their Host Stars" at Hamburg Observatory and the Institute for Astrophysics Göttingen funded by the Deutsche Forschungsgemeinschaft (DFG).

The author acknowledges the use of data from the UVES Paranal Observatory Project (ESO Program ID 073.D-0424(A)).

This research has made use of the SIMBAD database, operated at CDS, Strasbourg, France.

Bibliography

Anderson, D. R., Hellier, C., Gillon, M., Triaud, A. H. M. J., Smalley, B., Hebb, L., Collier Cameron, A., Maxted, P. F. L., Queloz, D., West, R. G., Bentley, S. J., Enoch, B., Horne, K., Lister, T. A., Mayor, M., Parley, N. R., Pepe, F., Pollacco, D., Ségransan, D., Udry, S. & Wilson, D. M. (2009), 'WASP-17b: an ultra-low density planet in a probable retrograde orbit', *ArXiv e-prints*.

Bean, J. L., McArthur, B. E., Benedict, G. F., Harrison, T. E., Bizyaev, D., Nelan, E. & Smith, V. V. (2007), 'The Mass of the Candidate Exoplanet Companion to HD 33636 from Hubble Space Telescope Astrometry and High-Precision Radial Velocities', *AJ* **134**, 749–758.

Bean, J. L., Seifahrt, A., Hartman, H., Nilsson, H., Wiedemann, G., Reiners, A., Dreizler, S. & Henry, T. J. (2009), 'The CRIRES Search for Planets Around the Lowest-Mass Stars. I. High-Precision Near-Infrared Radial Velocities with an Ammonia Gas Cell', *ArXiv e-prints*.

Bouchy, F., Queloz, D., Deleuil, M., Loeillet, B., Hatzes, A. P., Aigrain, S., Alonso, R., Auvergne, M., Baglin, A., Barge, P., Benz, W., Bordé, P., Deeg, H. J., de La Reza, R., Dvorak, R., Erikson, A., Fridlund, M., Gondoin, P., Guillot, T., Hébrard, G., Jorda, L., Lammer, H., Léger, A., Llebaria, A., Magain, P., Mayor, M., Moutou, C., Ollivier, M., Pätzold, M., Pepe, F., Pont, F., Rauer, H., Rouan, D., Schneider, J., Triaud, A. H. M. J., Udry, S. & Wuchterl, G. (2008), 'Transiting exoplanets from the CoRoT space mission. III. The spectroscopic transit of CoRoT-Exo-2b with SOPHIE and HARPS', *AAP* **482**, L25–L28.

Butler, R. P., Marcy, G. W., Williams, E., Hauser, H. & Shirts, P. (1997), 'Three New "51 Pegasi–Type" Planets', *APJL* **474**, L115+.

Butler, R. P., Marcy, G. W., Williams, E., McCarthy, C., Dosanjh, P. & Vogt, S. S. (1996), 'Attaining Doppler Precision of 3 M s-1', *PASP* **108**, 500–+.

Dekker, H., D'Odorico, S., Kaufer, A., Delabre, B. & Kotzlowski, H. (2000), Design, construction, and performance of UVES, the echelle spectrograph for the UT2 Kueyen Telescope at the ESO Paranal Observatory, *in* M. Iye & A. F. Moorwood, eds, 'Proc. SPIE Vol. 4008, p. 534-545, Optical and IR Telescope Instrumentation and Detectors, Masanori Iye; Alan F. Moorwood; Eds.', pp. 534–545.

Fabrycky, D. C. & Winn, J. N. (2009), 'Exoplanetary Spin-Orbit Alignment: Results from the Ensemble of Rossiter-McLaughlin Observations', *ApJ* **696**, 1230–1240.

Gilliland, R. L., Morris, S. L., Weymann, R. J., Ebbets, D. C. & Lindler, D. J. (1992), 'Resolution and noise properties of the Goddard High-Resolution Spectrograph', *PASP* **104**, 367–382.

Gillon, M. (2009), 'Spin-orbit misalignement for the transiting planet HD 80606b', *ArXiv e-prints*.

Gillon, M., Anderson, D. R., Triaud, A. H. M. J., Hellier, C., Maxted, P. F. L., Pollaco, D., Queloz, D., Smalley, B., West, R. G., Wilson, D. M., Bentley, S. J., Collier Cameron, A., Enoch, B., Hebb, L., Horne, K., Irwin, J., Joshi, Y. C., Lister, T. A., Mayor, M., Pepe, F., Parley, N., Segransan, D., Udry, S. & Wheatley, P. J. (2009), 'Discovery and characterization of WASP-6b, an inflated sub-Jupiter mass planet transiting a solar-type star', *AAP* **501**, 785–792.

Gizon, L. & Solanki, S. K. (2003), 'Determining the Inclination of the Rotation Axis of a Sun-like Star', *APJ* **589**, 1009–1019.

Gray, D. F. (1976), *The observation and analysis of stellar photospheres*, Research supported by the National Research Council of Canada. New York, Wiley-Interscience, 1976. 484 p.

Hestroffer, D. & Magnan, C. (1998), 'Wavelength dependency of the Solar limb darkening', *Astronomy and Astrophysics* **333**, 338–342.

Jenkins, J. M., Borucki, W. J., Koch, D. G., Marcy, G. W., Cochran, W. D., Basri, G., Batalha, N. M., Buchhave, L. A., Brown, T. M., Caldwell, D. A., Dunham, E. W., Endl, M., Fischer, D. A., Gautier, III, T. N., Geary, J. C., Gilliland, R. L., Howell, S. B., Isaacson, H., Johnson, J. A., Latham, D. W., Lissauer, J. J., Monet, D. G., Rowe, J. F., Sasselov, D. D., Welsh, W. F., Howard, A. W., MacQueen, P., Chandrasekaran, H., Twicken, J. D., Bryson, S. T., Quintana, E. V., Clarke, B. D., Li, J., Allen, C., Tenenbaum, P., Wu, H., Meibom, S., Klaus, T. C., Middour, C. K., Cote, M. T., McCauliff, S., Girouard, F. R., Gunter, J. P., Wohler, B., Hall, J. R., Ibrahim, K., Kamal Uddin, A., Wu, M. S., Bhavsar, P. A., Van Cleve, J., Pletcher, D. L., Dotson, J. A. & Haas, M. R. (2010), 'Discovery and Rossiter-McLaughlin Effect of Exoplanet Kepler-8b', *ArXiv e-prints*.

Johnson, J. A., Winn, J. N., Albrecht, S., Howard, A. W., Marcy, G. W. & Gazak, J. Z. (2009), 'A Third Exoplanetary System with Misaligned Orbital and Stellar Spin Axes', *PASP* **121**, 1104–1111.

Johnson, J. A., Winn, J. N., Narita, N., Enya, K., Williams, P. K. G., Marcy, G. W., Sato, B., Ohta, Y., Taruya, A., Suto, Y., Turner, E. L., Bakos, G., Butler, R. P., Vogt, S. S., Aoki, W., Tamura, M., Yamada, T., Yoshii, Y. & Hidas, M. (2008), 'Measurement of the Spin-Orbit Angle of Exoplanet HAT-P-1b', *ApJ* **686**, 649–657.

Lagarde, S., Sanchez, L. J. & Petrov, R. G. (1995), Sub-resolution Limit Spatio-Spectral Information Using Differential Speckle Interferometry, *in* G. Comte & M. Marcelin, ed., 'IAU Colloq. 149: Tridimensional Optical Spectroscopic Methods in Astrophysics', Vol. 71 of *Astronomical Society of the Pacific Conference Series*, pp. 360–+.

Le Bouquin, J., Absil, O., Benisty, M., Massi, F., Mérand, A. & Stefl, S. (2009), 'The spin-orbit alignment of the Fomalhaut planetary system probed by optical long baseline interferometry', *AAP* **498**, L41–L44.

Loeillet, B., Shporer, A., Bouchy, F., Pont, F., Mazeh, T., Beuzit, J. L., Boisse, I., Bonfils, X., da Silva, R., Delfosse, X., Desort, M., Ecuvillon, A., Forveille, T., Galland, F., Gallenne, A., Hébrard, G., Lagrange, A., Lovis, C., Mayor, M., Moutou, C., Pepe, F., Perrier, C., Queloz, D., Ségransan, D., Sivan, J. P., Santos, N. C., Tsodikovich, Y., Udry, S. & Vidal-Madjar, A. (2008), 'Refined parameters and spectroscopic transit of the super-massive planet HD 147506b', *AAP* **481**, 529–533.

Marcy, G. W. & Butler, R. P. (1992), 'Precision radial velocities with an iodine absorption cell', *PASP* **104**, 270–277.

Marcy, G. W., Butler, R. P., Williams, E., Bildsten, L., Graham, J. R., Ghez, A. M. & Jernigan, J. G. (1997), 'The Planet around 51 Pegasi', *APJ* **481**, 926–+.

Markwardt, C. B. (2009), Non-linear Least-squares Fitting in IDL with MPFIT, *in* D. A. Bohlender, D. Durand, & P. Dowler, ed., 'Astronomical Society of the Pacific Conference Series', Vol. 411 of *Astronomical Society of the Pacific Conference Series*, pp. 251–+.

Mayor, M. & Queloz, D. (1995), 'A Jupiter-mass companion to a solar-type star', *Nature* **378**, 355–359.

Moré, J. (1978), *The Levenberg-Marquardt Algorithm: Implementation and Theory*, Numerical Analysis, vol. 630, ed. G. A. Watson (Springer-Verlag: Berlin), p. 105.

Moré, J. & Wright, S. (1993), *Optimization Software Guide*, SIAM, Frontiers in Applied Mathematics, Number 14.

Narita, N., Enya, K., Sato, B., Ohta, Y., Winn, J. N., Suto, Y., Taruya, A., Turner, E. L., Aoki, W., Yoshii, M., Yamada, T. & Tamura, Y. (2007), 'Measurement of the Rossiter-Laughlin Effect in the Transiting Exoplanetary System TrES-1', *PASJ* **59**, 763–770.

Narita, N., Hirano, T., Sato, B., Wink, J. N., Suto, Y., Turner, E. L., Aoki, W., Tamura, M. & Yamada, T. (2009*a*), 'Improved Measurement of the Rossiter-McLaughlin Effect in the Exoplanetary System HD 17156', *PASJ* **61**, 991–.

Narita, N., Sato, B., Hirano, T. & Tamura, M. (2009*b*), 'First Evidence of a Retrograde Orbit of a Transiting Exoplanet HAT-P-7b', *PASJ* **61**, L35–L40.

Narita, N., Sato, B., Hirano, T., Winn, J. N., Aoki, W. & Tamura, M. (2010), 'Spin-Orbit Alignment of the TrES-4 Transiting Planetary System and Possible Additional Radial Velocity Variation', *ArXiv e-prints*.

Neckel, H. & Labs, D. (1994), 'Solar limb darkening 1986-1990 (lambda lambda 303 to 1099nm)', *Solar Physics* **153**, 91–114.

Palmer, C. (2005), *Diffraction grating handbook*, Diffraction grating handbook, sixth edition, Rochester, New York, Newport Corporation, 2005.

Piskunov, N. E. & Valenti, J. A. (2002), 'New algorithms for reducing cross-dispersed echelle spectra', *A&A* **385**, 1095–1106.

Pont, F., Endl, M., Bouchy, F., Aigrain, S., Moutou, C., Alonso, R., Baglin, A., Fridlund, M., Hatzes, A. P., Hebrard, G., Cochran, W. D., Barnes, S. I., Sneden, C. & MacQueen, P. J. (2009*a*), 'The spin-orbit angle of CoRoT-1: evidence for a strongly misaligned hot Jupiter', *ArXiv e-prints*.

Pont, F., Hébrard, G., Irwin, J. M., Bouchy, F., Moutou, C., Ehrenreich, D., Guillot, T., Aigrain, S., Bonfils, X., Berta, Z., Boisse, I., Burke, C., Charbonneau, D., Delfosse, X., Desort, M., Eggenberger, A., Forveille, T., Lagrange, A., Lovis, C., Nutzman, P., Pepe, F., Perrier, C., Queloz, D., Santos, N. C., Ségransan, D., Udry, S. & Vidal-Madjar, A. (2009*b*), 'Spin-orbit misalignment in the HD 80606 planetary system', *AAP* **502**, 695–703.

Press, W. H., Teukolsky, S. A., Vetterling, W. T. & Flannery, B. P. (1992), *Numerical recipes in C. The art of scientific computing*.

Richichi, A. & Roccatagliata, V. (2005), 'Aldebaran's angular diameter: How well do we know it?', *AAP* **433**, 305–312.

Richichi, A., Percheron, I. & Khristoforova, M. (2005), 'CHARM2: An updated Catalog of High Angular Resolution Measurements', *AAP* **431**, 773–777.

Schroeder, D. J. (1987), *Astronomical optics*, San Diego, CA, Academic Press, Inc, 1987, 363 p.

Seifahrt, A., Käufl, H. U., Zängl, G., Bean, J. L., Richter, M. L. & Siebenmorgen, R. (2010), 'Synthesising, using and correcting for telluric features in high-resolution astronomical spectra. A near-infrared case study using CRIRES.', *in preparation*.

Simpson, E. K., Pollacco, D., Hébrard, G., Gibson, N. P., Barros, S. C. C., Boisse, I., Bouchy, F., Cameron, A. C., Miller, G. R. M., Watson, C. A. & Keenan, F. P. (2010), 'The spin-orbit alignment of the transiting exoplanet WASP-3b from Rossiter-McLaughlin observations', *MNRAS* pp. 548–+.

Triaud, A. H., Cameron, A. C., Queloz, D., Anderson, D. R., Gillon, M., Hebb, L., Hellier, C., Loeillet, B., Maxted, P. F. L., Mayor, M., Pepe, F., Pollacco, D., Ségransan, D., Smalley, B., Udry, S., West, R. G. & Wheatley, P. J. (2010), 'Spin-orbit angle measurements for six southern transiting planets. New insights into the dynamical origins of hot Jupiters', *in preparation (AAP)*.

Triaud, A. H. M. J., Queloz, D., Bouchy, F., Moutou, C., Cameron, A. C., Claret, A., Barge, P., Benz, W., Deleuil, M., Guillot, T., Hébrard, G., Lecavelier Des Étangs, A., Lovis, C., Mayor, M., Pepe, F. & Udry, S. (2009), 'The Rossiter-McLaughlin effect of CoRoT-3b and HD 189733b', *AAP* **506**, 377–384.

Tripathi, A., Winn, J. N., Johnson, J. A., Howard, A. W., Halverson, S., Marcy, G. W., Holman, M. J., de Kleer, K. R., Carter, J. A., Esquerdo, G. A., Everett, M. E. & Cabrera, N. E. (2010), 'A Prograde, Low-Inclination Orbit for the Very Hot Jupiter WASP-3b', *ArXiv e-prints*.

Valenti, J. A., Butler, R. P. & Marcy, G. W. (1995), 'Determining Spectrometer Instrumental Profiles Using FTS Reference Spectra', *PASP* **107**, 966–+.

Winn, J. N., Howard, A. W., Johnson, J. A., Marcy, G. W., Gazak, J. Z., Starkey, D., Ford, E. B., Colón, K. D., Reyes, F., Nortmann, L., Dreizler, S., Odewahn, S., Welsh, W. F., Kadakia, S., Vanderbei, R. J., Adams, E. R., Lockhart, M., Crossfield, I. J., Valenti, J. A., Dantowitz, R. & Carter, J. A. (2009*a*), 'The Transit Ingress and the Tilted Orbit of the Extraordinarily Eccentric Exoplanet HD 80606b', *ApJ* **703**, 2091–2100.

Winn, J. N., Johnson, J. A., Albrecht, S., Howard, A. W., Marcy, G. W., Crossfield, I. J. & Holman, M. J. (2009*b*), 'HAT-P-7: A Retrograde or Polar Orbit, and a Third Body', *ApJL* **703**, L99–L103.

Winn, J. N., Johnson, J. A., Fabrycky, D., Howard, A. W., Marcy, G. W., Narita, N., Crossfield, I. J., Suto, Y., Turner, E. L., Esquerdo, G. & Holman, M. J. (2009*c*), 'On the Spin-Orbit Misalignment of the XO-3 Exoplanetary System', *ApJ* **700**, 302–308.

Winn, J. N., Johnson, J. A., Howard, A. W., Marcy, G. W., Bakos, G. A., Hartman, J., Torres, G., Albrecht, S. & Narita, N. (2010), 'The HAT-P-13 Exoplanetary System: Evidence for Spin-Orbit Alignment and a Third Companion', *ArXiv e-prints*.

Winn, J. N., Johnson, J. A., Marcy, G. W., Butler, R. P., Vogt, S. S., Henry, G. W., Roussanova, A., Holman, M. J., Enya, K., Narita, N., Suto, Y. & Turner, E. L. (2006), 'Measurement of the Spin-Orbit Alignment in the Exoplanetary System HD 189733', *ApJL* **653**, L69–L72.

Winn, J. N., Johnson, J. A., Narita, N., Suto, Y., Turner, E. L., Fischer, D. A., Butler, R. P., Vogt, S. S., O'Donovan, F. T. & Gaudi, B. S. (2008), 'The Prograde Orbit of Exoplanet TrES-2b', *ApJ* **682**, 1283–1288.

Winn, J. N., Johnson, J. A., Peek, K. M. G., Marcy, G. W., Bakos, G. Á., Enya, K., Narita, N., Suto, Y., Turner, E. L. & Vogt, S. S. (2007), 'Spin-Orbit Alignment for the Eccentric Exoplanet HD 147506b', *ApJL* **665**, L167–L170.

Winn, J. N., Noyes, R. W., Holman, M. J., Charbonneau, D., Ohta, Y., Taruya, A., Suto, Y., Narita, N., Turner, E. L., Johnson, J. A., Marcy, G. W., Butler, R. P. & Vogt, S. S. (2005), 'Measurement of Spin-Orbit Alignment in an Extrasolar Planetary System', *ApJ* **631**, 1215–1226.

Wolf, A. S., Laughlin, G., Henry, G. W., Fischer, D. A., Marcy, G., Butler, P. & Vogt, S. (2007), 'A Determination of the Spin-Orbit Alignment of the Anomalously Dense Planet Orbiting HD 149026', *ApJ* **667**, 549–556.